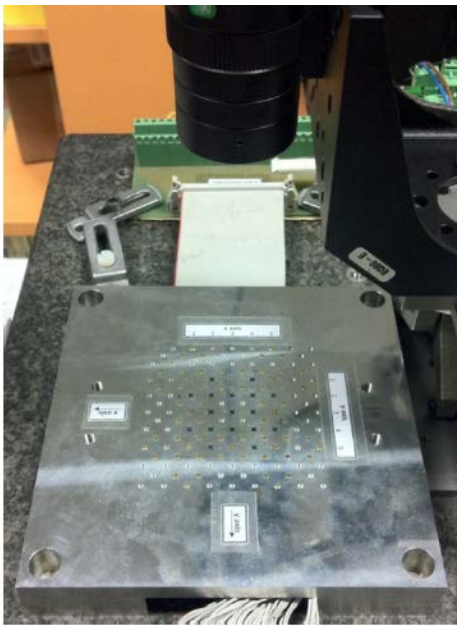
Par **Pengfei HUYAN**

Electromagnetic digital actuators array : characterization of a planar conveyance application and optimized design

Thèse présentée
pour l'obtention du grade
de Docteur de l'UTC



Soutenue le 27 mars 2015
Spécialité : Advanced Mechanics

D2178

Thèse
Présentée pour obtenir le grade de
DOCTEUR
De
UNIVERSITÉ DE TECHNOLOGIE DE COMPIÈGNE
Spécialité Mécanique Avancée
Par
Pengfei HUYAN

Réseau d'actionneurs électromagnétiques numériques : caractérisation d'une application de type convoyage et conception optimisée

Y. Haddab (FEMTO-ST – ENSMM, Besançon)	Rapporteur
F. Formosa (SYMME - Polytech Annecy Chambéry, Annecy)	Rapporteur
B. Lemaire-Semail (L2EP – Polytech'Lille, Lille)	Membre du jury
A. Hubert (LEC – UTC, Compiègne)	Membre du jury
C. Prelle (Laboratoire Roberval – UTC, Compiègne)	Directeur de thèse
L. Petit (Laboratoire Roberval – UTC, Compiègne)	Directeur de thèse

Laboratoire Roberval, UMR 7337, UTC / CNRS

Table of contents

CHAPTER I: STATE OF ART

I.1. DEFINITION 12

I.1.1. DIGITAL ACTUATOR 12

I.1.2. DIGITAL ACTUATOR CLASSIFICATION 13

I.2. TECHNOLOGICAL SOLUTIONS 16

I.2.1. SWITCHING METHODS 16

I.2.1.1. ELECTROMAGNETIC PRINCIPLE 16

I.2.1.2. THERMAL PRINCIPLE 21

I.2.1.3. ELECTROSTATIC PRINCIPLE 24

I.2.1.4. PIEZOELECTRIC PRINCIPLE 26

I.2.2. HOLDING METHODS 27

I.2.2.1. MAGNETIC HOLDING PRINCIPLE 28

I.2.2.2. BUCKLED STRUCTURE HOLDING PRINCIPLE 29

I.2.2.3. HOLDING FUNCTION REALIZED VIA COMPLEX MECHANISM/EXTERNAL ACTUATORS 31

I.2.2.4. HOLDING FUNCTION REALIZED VIA CONTINUOUS SWITCHING FUNCTION 33

I.3. APPLICATIONS 35

I.3.1. SINGLE ACTUATION 35

I.3.1.1. DISCRETE DISPLACEMENT OUTPUT 35

I.3.1.2. MECHANICAL SWITCH 37

I.3.1.2.1. Fludic Switch 37

I.3.1.2.2. Optical Switch 38

I.3.1.2.3. Electrical Switch 39

I.3.2. MULTIPLE ACTUATION BASED APPLICATIONS 40

I.3.2.1. MULTIPLE APPLICATION WITHOUT COLLABORATION 41

I.3.2.1.1. Tactile display 41

I.3.2.1.2. Optical Switch array 42

I.3.2.1.3. Mechanical memories 43

I.3.2.2. MULTIPLE APPLICATION WITH COLLABORATION 44

I.3.2.2.1. Digital robots 44

I.3.2.2.2. Digital to analog converters 45

I.3.2.2.3. Displacement table 46

I.4. CONCLUSION 47

CHAPTER II: PRINCIPLE AND MODELLING OF DIGITAL ELECTROMAGNETIC ACTUATORS ARRAY

II.1. ACTUATORS ARRAY ARCHITECTURE 51

II.1.1. ELEMENTARY ACTUATOR PRINCIPLE 51

II.1.2. ACTUATORS ARRAY PRINCIPLE 54

II.1.3. APPLICATION OF THE ARRAY 56

II.2. MODELLING OF THE ARRAY 58

II.2.1. CHOICE OF MODELING TOOLS 58

II.2.2. SEMI-ANALYTICAL MODELING WITH RADIA 60

II.2.2.1. MAGNETIC HOLDING FORCE 60

II.2.2.2. MAGNETIC INTERACTION FORCE 61

II.2.2.3. MAGNETIC BALANCE FORCE 63

II.2.2.4. TOTAL MAGNETIC FORCE 64

II.2.3. ANALYTICAL MODELING WITH MATLAB 65

II.2.3.1. MODELLING OF THE ELEMENTARY ACTUATOR 66

II.2.3.1.1. Magnetic flux density 66

II.2.3.1.2. Magnetic holding force 67

II.2.3.1.3. Electromagnetic force modelling 70

II.2.3.1.4. Self-returning zone calculation 71

II.2.4. COMPARISON OF THE TWO MODELS 76

II.3. CONCLUSION 77

CHAPTER III: EXPERIMENTAL REALIZATION AND CHARACTERIZATION OF THE ACTUATORS ARRAY

III.1. PRESENTATION OF THE PROTOTYPE 80

III.2. GEOMETRICAL STUDY OF THE PROTOTYPE ARRAY 81

III.2.1. MEASUREMENT TOOLS 82

III.2.2. MEASUREMENT OF THE DIMENSION AND POSITION ERRORS 82

III.2.3. INFLUENCE OF THE ERRORS ON MAGNETIC HOLDING FORCE 85

III.3. EXPERIMENTAL CHARACTERIZATION 87

III.3.1. EQUIPMENT SETUP 88

III.3.2. NON CONTACT MEASUREMENT TECHNIQUE 89

III.3.3. EXPERIMENTAL RESULTS 91

III.3.4. CONCLUSION 103

CHAPTER IV: OPTIMIZATION DESIGN OF THE PROTOTYPE ARRAY

IV.1. OPTIMIZATION TECHNIQUES 105
IV.1.1. CONTEXT OF THE OPTIMIZATION STUDY 105
IV.1.2. MULTI-OBJECTIVES OPTIMIZATION TECHNIQUES 106
IV.1.2.1. WEIGHTING OBJECTIVE METHOD 108
IV.1.2.2. MULTI-LEVEL OPTIMIZATION METHOD 109
IV.1.2.3. TRADE-OFF METHOD 109
IV.1.2.4. GENETIC ALGORITHM 110
IV.1.3. COMPARISON OF THE MO METHODS 112
IV.2. GENETIC OPTIMIZATION REALIZED IN MATLAB 113
IV.2.1. PERFORMANCE INDICATORS 113
IV.2.2. DESIGN PARAMETERS 115
IV.2.3. SINGLE-OBJECTIVE OPTIMIZATION 116
IV.2.3.1. OPTIMIZATION SETUP 116
IV.2.3.2. SINGLE-OBJECTIVE OPTIMIZATION RESULTS 117
IV.2.4. MULTI-OBJECTIVE OPTIMIZATION 119
IV.2.4.1. OPTIMIZATION SETUP 120
IV.2.4.2. MULTI-OBJECTIVE OPTIMIZATION RESULTS 120
IV.2.5. COMPARISON OF THE TWO METHODS 124
IV.3. CONCLUSION 127

CHAPTER V: CONCLUSION AND PERSPECTIVES

V.1. CONCLUSION 129
V.2. PERSPECTIVES 130
V.2.1. PERSPECTIVES OF THE EXISTING ACTUATORS ARRAY 131
V.2.1.1. DYNAMIC MODELLING OF THE PLANAR CONVEYANCE DEVICE 131
V.2.1.2. OPTIMIZATION OF THE FRICTION CONDITIONS BETWEEN THE PLATE AND MPMS 131
V.2.2. NEW DEVELOPMENTS 132
V.2.2.1. DIGITAL ACTUATOR WITH THREE DISPLACEMENT DIRECTIONS 132
V.2.2.2. ACTUATORS ARRAY WITH DIFFERENT STROKES 133
V.2.2.3. MICRO-FABRICATED DIGITAL ACTUATORS ARRAY 134

Abbreviations

PM	Permanent Magnet
MPM	Mobile Permanent Magnet
FPM	Fixed Permanent Magnet
AFPM	Additional Fixed Permanent Magnet
PCB	Printed Circuit Board
UW	Upper Wire
LW	Lower Wire
SRZ	Self-Returning Zone
IZ	Intermediate Zone
MO	Multi-Objectives
SO	Single-Objective
IF	Interference Force
VF	Variation Force
GOT	Global Optimization Toolbox

Introduction

In mechanical or mechatronical systems, actuators are the components used to convert input energy, generally electrical energy, into mechanical tasks such as motion, force or a combination of both. The most frequently encountered actuators in such systems are based on an analogical principle because their mobile part can reach any position within their operating stroke. Analogical actuators present several advantages. Besides their ability to perform continuous actions within their working limits, analogical actuators can achieve high performances with high reliability levels. For these purposes, closed-loop controls are generally implemented with the need of feedback sensors. However depending on the actuator design, the physical phenomenon used to generate the motion or the actuator environment, their control can become very complex to ensure high performances levels or complex tasks. The integration of feedback sensors can also be a problem and is not always possible especially for compact or highly integrated mechanical or mechatronical systems. Moreover to keep the mobile part in a given position within rejecting disturbances, continuous energy supply is needed that can generate heating or deterioration of these systems.

In order to try to overcome these drawbacks, an alternative type of actuators based on a digital principle has been developed in literature. The mobile part of these digital actuators can switch between a finite number of well defined and repeatable discrete positions. All the positions located between two discrete positions are only transient states and cannot be held in normal functioning. The discrete positions are theoretically well defined during the manufacturing step of these actuators. Feedback sensors are then not required and their control is realized in open-loop. Due to their digital principle, these actuators have several advantages as low energy consumption because energy is only needed for the switching of the mobile part between the discrete positions and there is no energy consumption to hold a position. The control of digital actuators is also very simple because only energy pulses are needed. Very simple open-loop controls based on digital outputs of data acquisition boards can then be used. However compared to analogical actuators, digital actuators present two main drawbacks. The manufacturing errors of these actuators have to be precisely controlled because, unlike to analogical actuators, a manufacturing error cannot be compensated using the control law. Another drawback is their inability to realize continuous tasks because of their discrete stroke. An assembly of several digital actuators can nevertheless realize multi-

discrete tasks.

In a former thesis realized at the Roberval laboratory of the Université de Technologie de Compiègne [PETI 2009], a digital electromagnetic actuator has been studied and developed. The originality of this work is based on the selected architecture that enables to realize displacements along two independent and orthogonal axes. In this thesis, a single digital actuator has been firstly designed, modeled and manufactured. The performances of this experimental actuator have been characterized (switching time along the two displacement axes, energy consumption, positioning repeatability error, displaceable mass) and a comparison between simulated and experimental results has shown a good agreement. An array composed of 25 elementary actuators arranged in a 5 × 5 matrix configuration has then been designed by considering the magnetic and electromagnetic interaction between the elementary actuators of the array. A prototype of the array has finally been manufactured and assembled.

The present thesis has been realized in the continuity of the work realized in the thesis described in the previous paragraph. The first main objective of the present thesis is focused on the characterization of the existing actuators array and also a planar conveyance application based on the actuators array. For that purpose, a modeling of the actuators array and experimental tests have been carried out in order to determine the influence of some parameters on the actuators array behavior. The second objective is to design a new version of the actuators array based on the experience of the first prototype. An optimization of the design has then been realized using genetic algorithm techniques while considering several criteria. The work realized in the thesis is described in this manuscript which is divided into five chapters.

Chapter 1 provides a state of art of the digital actuation. The definition and the properties of digital actuators are firstly given. Then the different physical principles and technical solutions used in literature for digital actuators are described. A classification of digital actuators based on the number of stable position is also proposed. Finally, the applications of digital actuators described in literature are detailed.

Chapter 2 presents the principles of the elementary electromagnetic digital actuator and of the actuators array. The properties of the existing actuators array prototype are given and the planar conveyance application and the dedicated control strategy are detailed. At the end of

this chapter, an analytic static model developed to characterize the digital actuators array is presented in detail.

Chapter 3 is focusing on the experimental characterization of the digital actuators array prototype especially the planar conveyance application. The manufacturing errors of the prototype have been firstly measured and their influences on the performances of the digital actuators array have been determined using the developed model. The experimental setup of the prototype and the non-contact measurement technique used for characterization are then presented. Experimental tests of the digital actuators array as a planar conveyance device are presented and displacements along the two axes are shown. In this chapter, the influences of several controlling parameters as the controlling current values, the shape of the current pulses or the displaced mass are shown.

Based on the experience of the first prototype, an optimization of the actuators array design is presented in chapter 4. The objective of this study is to improve the performances of the array while considering three performance indicators which characterize the behavior homogeneity, the independent functioning and the digital behavior respectively. An overview of the existing multi-objective optimization techniques is firstly presented and then the genetic algorithm technique has been selected for this optimization study. The implementation of the genetic algorithm on MATLAB is then presented. Single-objective and multi-objective optimizations have both been realized and finally an optimized design of the actuators array is proposed.

Chapter 5 gives a conclusion of the work realized in the thesis. Short-term and long-term perspectives of this work are finally proposed.

Chapter 1: State of art

The work presented in this thesis focuses on a digital actuators array. In order to define the digital actuation and to identify the existing needs and solutions related to this kind of actuation, the first chapter provides a state of art on this subject. The objective is to detail the different architectures of digital actuators and digital actuators array, the physical principles used for the different functions and also the applications of the digital actuators.

This chapter begins with a general definition of the different types of digital actuators. A classification of digital actuators is then given. The physical principles encountered in literature to realize the elementary functions of digital actuators are presented with examples. The advantages and disadvantages of these physical principles are also presented. At the end, applications based on digital actuators are described. These applications are classified into two types. The first one regroups applications based on a single digital actuator and called “single actuation”. The second one regroups applications based on an assembly of several digital actuators and called “multi actuation”. Examples of these two types are given to explain different applications.

I.1. Definition

I.1.1. Digital actuator

Actuators are the components that convert input energy into specific task such as motion, force or a combination of both. Based on their operation principle, actuators can be classified into analog actuators and digital actuators. Analog actuators are the classic actuators which are generally encountered in literature. They can provide high performances (accuracy positioning and etc) and are widely used in mechanical and mechatronic systems. Their major advantages can be concluded as high positioning accuracy and variable stroke. Moreover, they are theoretically capable of reaching any position within their operating range. However, there are two main disadvantages associated with these actuators. First, these actuators demand continuous energy supply in order to maintain any required position within their operating range. Second, they need feedback sensors to control their operation, for example to achieve precise positioning in different applications.

In the case of compact systems, there are not always enough space to integrate these sensors, analog actuators may be then not suitable. The use of digital actuators can simplify the integration and control. Digital actuators are a type of actuator which has a limited number of well defined repeatable states called “discrete positions” [PETI 2010, WU 2010] and the mobile part of these actuators can switch between the discrete positions. Moreover, these positions are theoretically well defined at the manufacturing process step; therefore, additional sensors are not required to control the position of the actuator. It leads to a simpler open loop control. Due to their easy principle, such systems have several advantages such as: simple, robust, lightweight, low energy consumption (no need of energy consumption for maintaining the discrete positions). Their performances (precision, resolution) are defined at the design step and ensured at manufacturing step in order to achieve predefined discrete positions or stable positions. They can be easily controlled via open loop control without the need of any feedback sensor which facilitates a minimalist design and thus small dimensions. Due to the absence of sensor, their integration into mechatronic systems is facilitated. At the end, their stroke values are usually small and fixed, but can be improved by assembling multiple digital actuators to achieve variable extended strokes [CHEN 2011].

The behavior of a digital actuator can be illustrated by a ball placed in a mechanical structure as shown in Figure I-1.

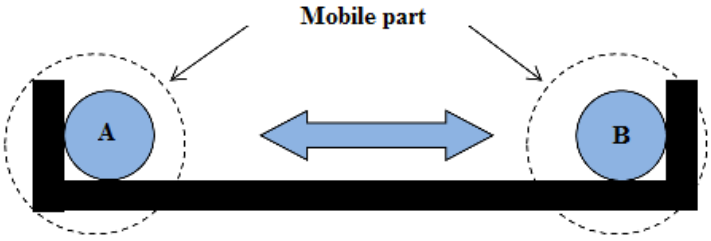


Fig I-1: Illustration of a digital actuator with two discrete positions

The ball represents the mobile part of the actuator and the structure with two vertical supports that represents the fixed part with the two discrete positions (i.e., position A and B). Theoretically, the mobile part cannot be held in any intermediate zone located between the discrete positions. The intermediate zone only corresponds to the transitional state of the mobile part during a switch. The main advantage of the digital actuators is that they only need actuation energy while switching between its discrete positions.

I.1.2. Digital actuator classification

According to the literature [ZAID 2011, PETI 2009, PANE 2009, WANG 2009, CAZO 2009, and PARK 2008], digital actuators may be classified into different types. A classification based on the number of stable positions is proposed in this chapter:

- **Digital actuators with zero stable position (Type I)**
- **Digital actuators with one stable position (Type II)**
- **Digital actuators with two or more stable positions (Type III)**

A stable position is a key position in a digital actuator. It is referred to a special kind of discrete position. The major difference between the stable position and a simple discrete position is that the mobile part of the actuator can be kept without any need of the external input energy at the stable position even in presence of disturbances. Inversely for a simple discrete position, if a disturbance moves the mobile part from the discrete position, it will not return to the discrete position. External input energy is then needed to keep the mobile part in discrete position. The description regarding the above mentioned categories based on stable positions are provided in the following sections.

- **Digital actuators with no stable position (Type I)**

In order to explain the classification of digital actuators, two necessary functions of the digital actuators are presented: the switching function and the holding function. The switching function corresponds to movement of the mobile part of the digital actuator when submitted to a driving force created thanks to a driving current. The mobile part is then switched between the discrete positions. The holding function corresponds to the holding of the mobile part in a discrete position. These two functions will be presented in detail in the following section (see section I.2.).

Type I regroups digital actuators which possess no stable position but two discrete positions as illustrated in Figure I-1. For this type of digital actuator, it is necessary to apply the switching command which enables the driving force (see section I.2.1) during all the switching time to ensure that the mobile part switches from one discrete position (i.e., position A in Figure I-1) to the second discrete position (i.e., position B).

- **Digital actuators with one stable position (Type II)**

The second type (Type II) represents digital actuators with only one stable position and one or several discrete positions as illustrated in Figure I-2-a and b. When there is no driving force or when the driving force is not high enough, the mobile part of the digital actuator will remain/or return to its stable position without external energy supply. In these actuators, a driving force greater than holding force (see section I.2.2) is needed to switch the mobile part between the discrete positions. However, once the switching command is removed, the mobile part will return to its stable position without energy consumption due to the presence of holding force. In Figure I-2, the red solid line represents the switching command which is used to switch the mobile part. With this one, a switching of the actuator from left to right can be realized. Similarly, the black dotted line represents the switching command which enables a switching of the actuator from right to left.

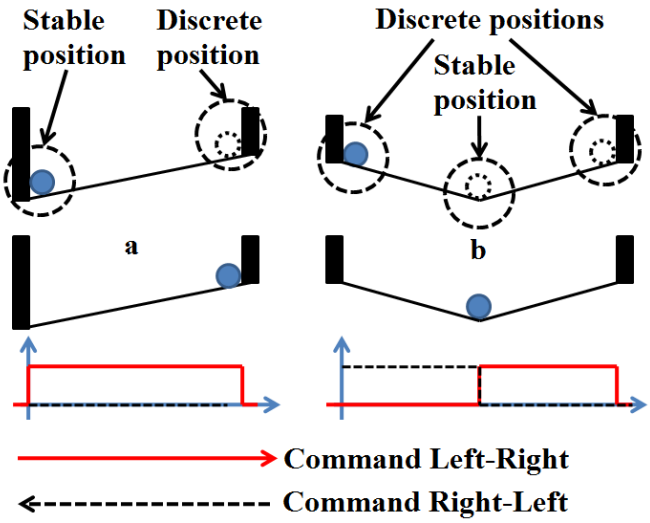


Fig I-2: Digital actuators of type II

- **Digital actuators with two stable position (Type III)**

The third type (Type III) includes digital actuators which have two or more stable positions as shown in the Figure I-3-b, c and d. In this figure, the slope area represents the zone (called self-returning zone and detailed in chapter II) where locates the stable position. Within the range of the self-returning zone, the mobile part of the actuator can return to its stable positions without energy consumption. On the other hand, the area between the self-returning zones is called intermediate zone. In a normal switching, the mobile part cannot stop in this zone. The major difference among the actuators configurations presented in Figure I-3-a, b, c and d is their length of self-returning zone and intermediate zone.

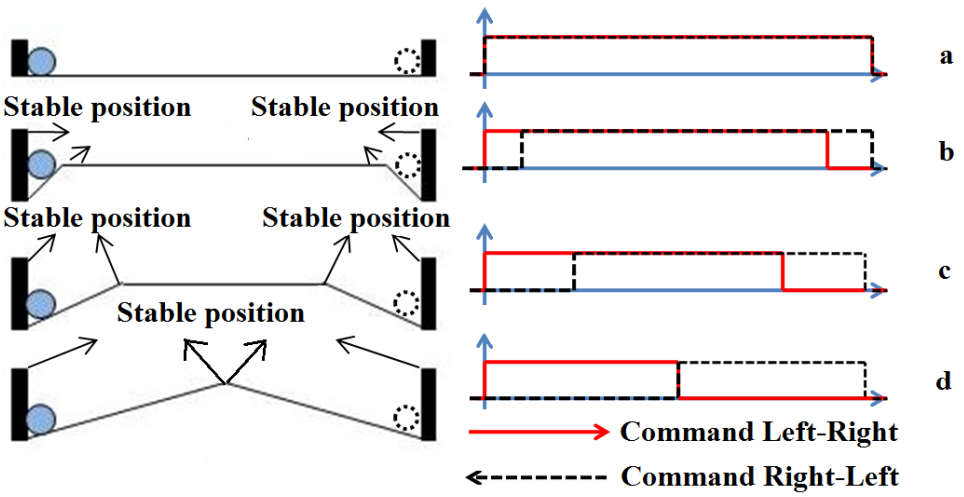


Fig I-3: Illustration of the a Type I digital actuator with switching command, b, c, d Type II digital actuator with switching command

In stable positions, the mobile part of digital actuators is held by the holding force. To switch the mobile part between the two stable positions, the holding force must overcome with the driving force or be removed before applying the driving force. In this scenario, the switching command is only needed until the entrance of the self-returning zone (see Figure I-3). Afterward, the mobile part will reach towards its stable position without energy consumption. In Figure I-3, different forms of switching command are illustrated corresponding to the different actuators (Figure I-a, b, c, d) configurations. In similar fashion, the red solid line represents the switching command which drives the mobile part of the digital actuator from the left side to the right side, and the black dotted line represents the opposite. The difference between the commands of the presented four actuators is then the duration of switching command needed to actuate the mobile part.

In the Type III actuator, a special group composed of bistable actuators as shown in the Figure I-3-d exists. These actuators exhibit two stable positions and no intermediate zone. To actuate the mobile part between the two stable positions, this holding force must be overcome by the driving force or be removed before applying the driving force [ZAID 2011].

I.2. Technological solutions

It has been previously presented that for digital actuators, two functions are needed: the switching and the holding functions. In the following section, the technological solutions used in literature to realize these two functions are presented.

I.2.1. Switching Methods

Switching is the first elementary function of digital actuators that ensure the switch of the mobile part between discrete positions. To realize the switching function, a driving force is generated and exerted on the mobile part. In the literature, several physical principles are used to generate the switching: electromagnetic, thermal, electrostatic, piezoelectric, etc... In the following text, each principle is detailed with examples.

I.2.1.1. Electromagnetic Principle

The electromagnetic principle is characterized by the interaction between magnetic and electrical phenomena. It is based on the appearance of electromagnetic force exerted on an electrically charged particle moving in the presence of a magnetic field. For this type of

actuators, the electromagnetic force is used as the driving force. The actuators based on this principle have been widely used for the actuation of digital actuators as they have several advantages such as: high speed, fast response, simple design and low cost.

An electromagnetic force can be generated via three forms. The first form corresponds to the reluctance force phenomenon. The generation of the reluctance force is similar to the flow of electric energy in an electrical circuit. The electric field causes an electric current to follow the path of the least resistance. Similarly, in a magnetic circuit the magnetic field causes magnetic flux to follow the path of the least magnetic reluctance/resistance. However in a magnetic circuit, the magnetic energy is stored rather than dissipated unlike in electrical circuit. When a coil of the magnetic circuit is energized, a reluctance force appears in order to minimize the overall reluctance of the magnetic circuit [ZADI 2011]. The expression of this force is given by Equation I-1.

$$F_m = \frac{d\left(\frac{R_m}{\Phi}\right)}{de} \qquad \text{(I-1)}$$

R_m : Reluctance (H^{-1}),

Φ : Magnetic flux (Wb),

F_m : Magnetomotive force (V),

e : Magnetic gap (mm).

Zhang et al. [ZHAN 2007] have presented a bistable actuator of type III based on the reluctance force for the switching function. This actuator consists of a cantilever beam with two free ends, a torsional beam with two fixed ends, a coil with magnetic core and permanent magnets (Figure I-4). The switching of the cantilever beam between the two stable states is obtained with a reluctance force by injecting a 70 mA current pulse through the integrated coils. Because of the appearance of the reluctance force, the magnetic plate is vertically attracted towards the coil. In this case, the cantilever beam rotates (in clockwise or counter clockwise as function of the current sign) around the torsional beam and realizes one switch. This bistable actuator with a total size of 2.0 mm × 2.2 mm can provide a 17 μm stoke with a switching time of 20 μs.

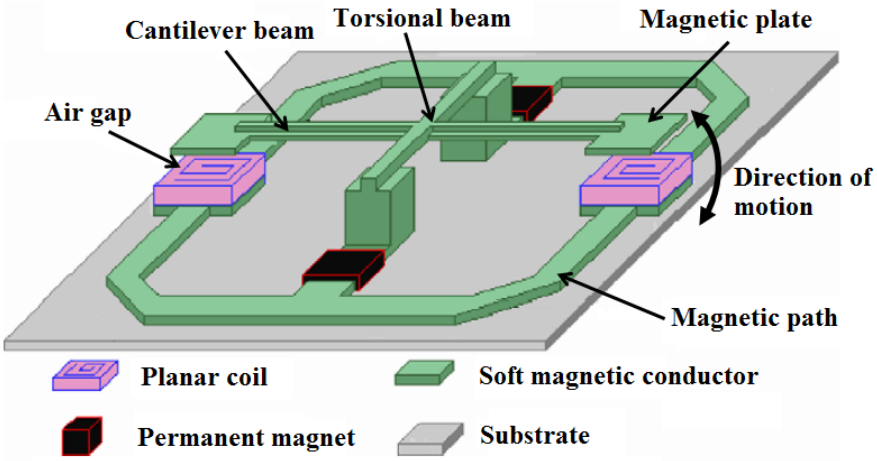


Fig I-4: Electromagnetic bistable actuator, Zhang et al. [ZHAN 2007]

Luharuka et al. [LUHA 2008] have presented an electromagnetic bistable valve of type III which consists of a fully compliant bistable micro-mechanism that provides a rotational motion to the gate with two stable positions (on and off states). A mobile part (i.e., suspended gate mass) composed of soft magnetic material (nickel–iron alloy) can rotate around its axis between two stable positions. In the Figure I-5-a and b, the open and close states of the valve are represented. The switching between the two states is realized with four actuation posts placed around the suspended mass. When the electromagnetic actuation posts are supplied, a reluctance force appears that generates the rotation of the mobile part in order to ensure the alignment of with the post. Two architectures have been designed by Luharuka et al.: the compliant bistable mechanism is placed outside (Figure I-5-a) or inside (Figure I-5-b) the device. These two designs have been manufactured with the help of micro-fabrication techniques. The diameters of the two valves are 3 mm and 1.2 mm and rotation angles are 10° and 20° respectively for inside and outside valves. The torque generated by these two designs is 1 to 2 µN·m.

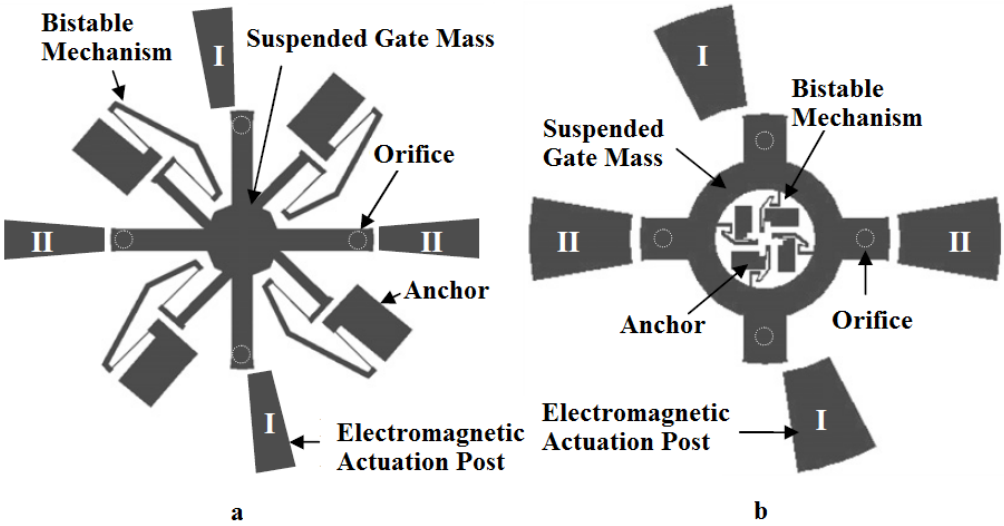


Fig I-5: Electromagnetic rotate valve: a. Inside b. Outside, [LUHA 2008]

The second electromagnetic phenomenon is the Lorentz force. This force appears due to the interaction between an electrical wire carrying an electric current (I) and an external magnetic flux density prevailing around the conductor (B). The expression of the Lorentz force (F) is given by Equation I-2.

$$\vec{F} = I \times \vec{l} \wedge \vec{B} \qquad \text{(I-2)}$$

$\vec{F}$: Lorentz force (N),

I : Current passing through the electrical wire (A),

$\vec{l}$: Length of the wire (m),

$\vec{B}$: Magnetic flux density (T).

Wang et al. [WANG 2009] have developed a bistable actuator of type III based on the Lorentz force for the switching function. This actuator consists of a compliant chevron-type mechanism actuating a shuttle mass, flexible hinges, hinged beams and lateral springs as shown in the Figure I-6. The actuator has been micro-fabricated on a glass substrate. Lorentz force is used to perform bi-directional motion in a plane by placing the whole structure on a square permanent magnet (see Figure I-6). To actuate the hinged structure between two stable positions, an Alternating Current (AC) is passed through the hinged beams via two contact pads. Each beam then experiences a Lorentz force perpendicular to both the directions of the current and magnetic field. The vibration induced by the electromagnetic actuation ensures the switch from one stable position to the other. A 90 µm forward and backward stroke is reported by the authors for this actuator.

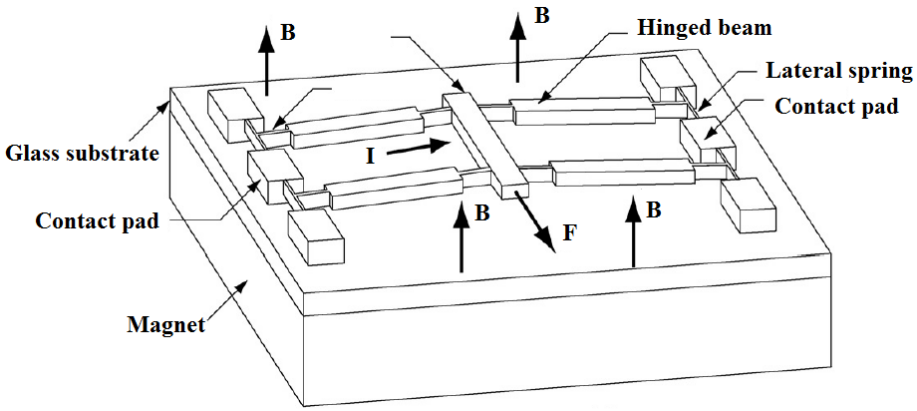


Fig I-6: Electromagnetic bistable actuator, Type III [WANG 2009]

Wu et al. [WU 2010] have also designed a bistable actuator of type III based on the switching using Lorentz force. The key component of this actuator is a circular-supported cantilever beam (see Figure I-7) which is made of soft permalloy magnetic material. It is suspended in air by two supporting torsion flexures at its two sides and can rotate clockwise and counter clockwise around the circular-shaped support. To actuate the actuator, current is sent through the external electric circuits. Lorentz force is then generated between the circular-supported cantilever beam and the electric circuits. It drives the cantilever beam rotating and then in contact with the circuit. The two stable positions of the actuator are reached by switching the current between the two external electric circuits.

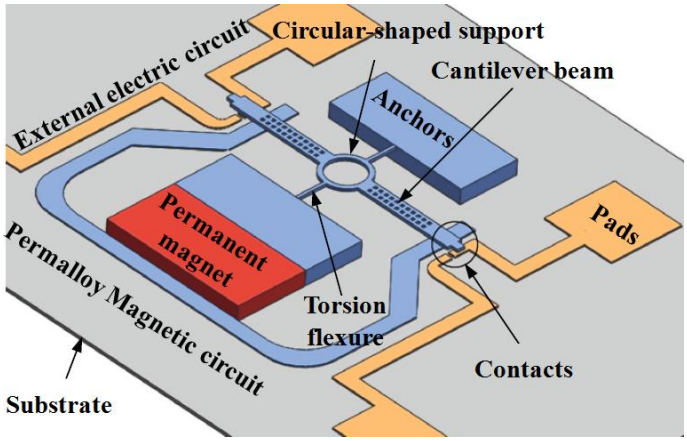


Fig I-7: Electromagnetic bistable actuator, Type III [WU 2010]

The third form to realize electromagnetic force for actuation is based on the generation of induction force described by the Faraday's law. In an electromagnetic system, an induced current appears in a coil due to the magnetic flux density variation around it. This induced current creates a variable magnetic flux within the coil which creates an electromotive force (Equation I-3). In the force expression, the minus sign is due to the fact that the electromotive force is opposed to the change of the magnetic flux density which has created it.

$$F_{EM}(t) = -\frac{d\Phi(t)}{dt} \qquad \text{(I-3)}$$

F_{EM} : Electromotive force (V),

Φ : Magnetic flux (Wb).

Based on induction force principle, Roodenburg et al. [ROOD 2008] have presented an actuator of the type III. The mobile part of the actuator is able to switch vertically. The working principle is illustrated in Figure I-8. When a current (i_q) flows through the inductor, a magnetic flux density (B) is generated and produces induced current in a copper plate (i_p) integrated with the movable part. The induced current is oriented in opposite direction as compared to the current in the inductor. A repulsive force is then generated between the inductor and the copper plate. The repulsion force exerted on the copper plate generates a downward switch of the mobile part. The switching in the opposite direction is obtained via the contact spring force. The actuator stroke is 25 mm, which is a quite big value compared to [ZHAN 2007, WANG 2009] (tens to hundreds micrometers). Its maximum actuation force is 200 kN for a current of 8 kA and switching time of 2 ms.

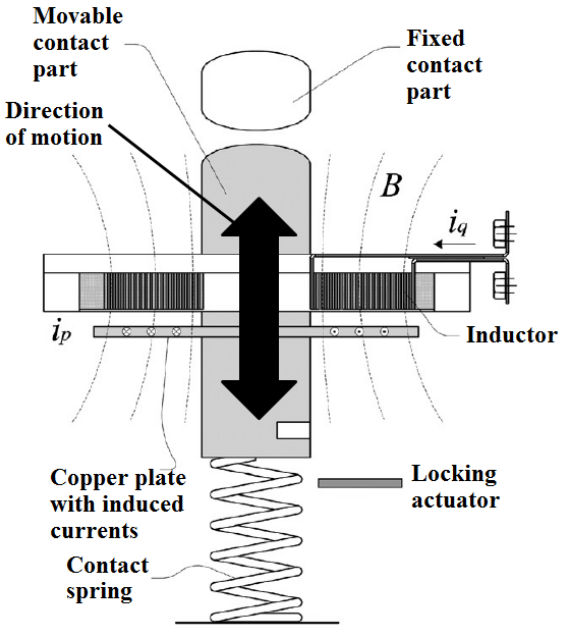


Fig I-8: Roodenburg et al. [ROOD 2008]

I.2.1.2. Thermal Principle

The second physical principle which has been widely used for digital actuators is the thermal principle. This principle can be applied in three different ways. The first form is based on thermal phenomenon based on the heating or cooling of a fluid in order to change its volume

thus realizing a change in pressure. The pressure variation is used to switch the mobile part of the actuator. The second form is based on a thermal mechanical expansion or contraction of materials as they undergo temperature changes without any phase change. Thermal actuators exhibit strong forces compared to other physical principles but the main drawbacks include their temperature dependency, slow actuation and control difficulties. The last form is based on the property of Shape Memory Alloy (SMA) material. SMAs have shown the remarkable property to return to a predefined shape when heated. This unique property is called Shape Memory Effect (SME). The SME occurs due to a solid-solid phase transformation between austenite and martensite phases due to local temperature changes within the solid.

Based on the first thermal phenomenon, Huesgen et al. [HUES 2010] have developed a type III digital actuator which is a thermo-pneumatic actuator for liquid flow control. The schematic cross section of the valve is shown in the Figure I-9. The actuator chamber (filled with a working fluid) is bounded on top by a bistable buckling membrane which is the mobile part of the actuator and on bottom by a micro scale Peltier element. On the opposite side, the Peltier element is fixed to a heat sink. When the sink is heated, it enables to thermally either expand or compress the working fluid and hence, the variation of the pressure switches the membrane between two stable positions (upward or downward). When no energy is supplied, the bistable membrane remains in either stable position. In the upward stable position, the membrane closes the inlet channel of the valve. When switched downwards stable position, the valve is open and allows a liquid flow. The switching energy for the valve is only 1 J for the closing and 2 J for the opening.

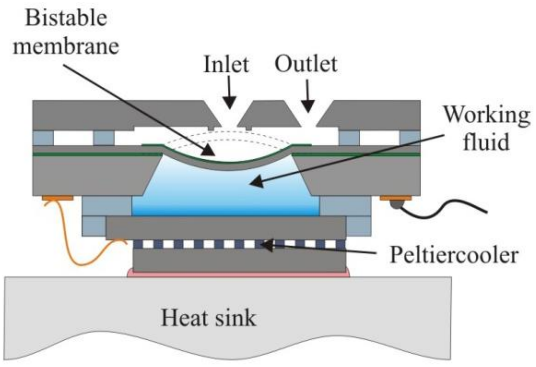


Fig I-9: Schematic cross section of the valve, HUESGEN et al. [HUES 2010]

In another study, Zaidi et al. [ZAID 2011] used the deformation of the Shape Memory Alloy material to switch a bistable curved-beam. Laser heating is used to induce temperature change for switching. This actuator is a type III digital actuator with two stable positions. The

actuator consists of three major elements. The first element is the bistable curved-beam which is a monolithic bistable mechanism. The second part is two pieces of SMA material on two sides of the beam separately shown in Figure I-10. The third part is the energy source, i.e., the laser. To switch the beam downward (stable position 2), SMA "1" is heated by laser which generates a phase change then induces the deformation of SMA "1". The deformation of SMA "1" generates the switch of the beam which induces a deformation of SMA "2". On the contrary, the beam can be switched upward (stable position 1) by heating the SMA "2". This beam has been fabricated by 3D printer and a SMA sample with the dimensions 3 × 1 × 0.1 mm^3 is used. The switching time is between 2s and 4s.

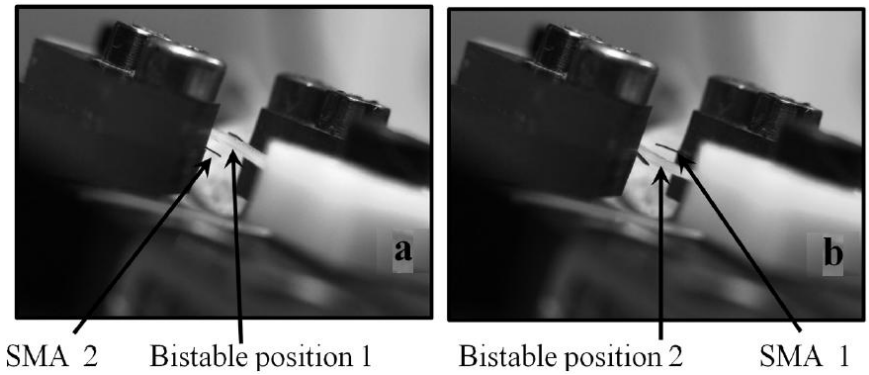
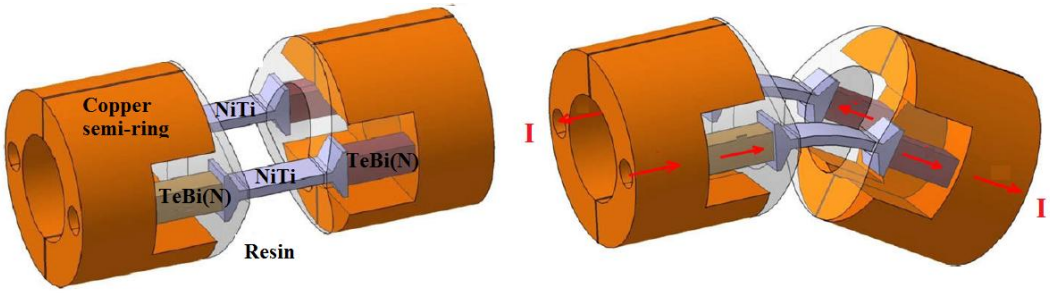


Fig I-10: Bistable actuator by Zaidi et al. [ZAID 2011]: a. Beam's first stable position b. Beam's second stable position

Abadie et al. [ABAD 2009] presented a new micro-actuator of type II for active endoscopy using SMA. In this device, the SMA deformation is obtained using Joule effect heating. The actuator is an assembly of two identical elementary stages as shown in Figure I-11. Each stage consists of two copper semi-rings. A single semi-ring has been realized with a Bi_2Te_3 N doped ingot, a NiTi blade, a Bi_2Te_3 P doped ingot. The overall dimensions of the actuator are 4 mm in diameter, 9 mm in length and 200 µm in thickness (for the NiTi blade). With a 0.6 A driving current, the actuator is able to produce a rotation of 25°. Moreover, by inverting the current, a symmetric deflection can be obtained. The reached deflection angle (stable states) can be maintained even when the current is removed [ABAD 2009].



a b

Fig I-11: Actuator constitution (left), electrically supplied actuator (right), Abadie et al. [ABAD 2009]

I.2.1.3. Electrostatic Principle

The third physical principle used for the switching function in digital actuators is the electrostatic principle. Electrostatic effect is based on the generation of attractive or repulsive force between two opposite or identical electric charges respectively. An actuator based on electrostatic principle generally consists of two facing surfaces called electrodes. These surfaces use the opposite or same changes to generate an attractive or repulsive electrostatic force between them. The force between the electrodes is derived from the gradient of electrostatic potential between the two electrodes as shown in Equation I-4. Electrostatic actuators provide contactless actuation but the main drawback of these actuators is their dependency on the electrode facing surface area and the air gap in between. As a result, their working range (stroke) is always limited. In the following text, examples are discussed based on the electrostatic actuation principle.

$$U = \frac{1}{2}CV^2$$
$$\vec{F}_{ES} = \frac{\partial U}{\partial x} = -\frac{\varepsilon_0 \varepsilon_r S V^2}{2x^2} \qquad \text{(I-4)}$$

U : Potential energy (J),

C : Capacitance (F),

V : Voltage across the two plates (V),

$\vec{F}_{ES}$: Electrostatic force normal to the plane of the electrodes (N),

ε_0 : Vacuum permittivity (F/m),

ε_r : Relative static permittivity of the medium between the electrodes (F/m),

S : Surface area of the facing electrode (m^2),

x : Gap between the two electrodes (m).

CHARLOT et al. [CHAR 2008] have used this principle to realize a bistable nanowire for

micromechanical memory. Electrostatic interaction force between an electrode and a nanowire has been used for switching. This actuator is also of type III and has two stable positions. The Figure I-12 presents a schematic layout of the structure. It consists of a pre-stressed beam nanowire (i.e., mobile part of the actuator) placed between two adjacent electrodes. Binary data are stored as the mechanical position of the beam. By applying a sufficiently large driving voltage (90 V) to a designated electrode, the electrically grounded nanowire will be electrostatically attracted and displaced to the stable position that is closer to the active electrode. Thus, the writing or erasing function is then achieved. The reading function is made by measuring the capacity between the nanowire and one of the side electrodes. Depending on the stability of the buckled structure, data can be stored permanently without the need of sustaining energy.

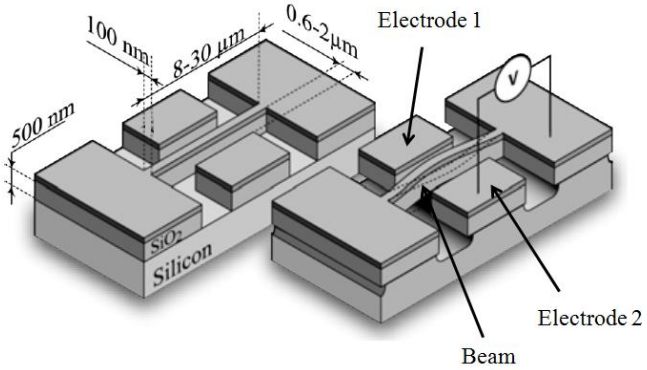


Fig I-12: Schematic of the in-plane pre-stressed buckling beam to be used as a non-volatile bistable mechanical memory, CHARLOT et al. [CHAR 2008]

CHAPUIS et al. [CHAP 2004] also used the electrostatic actuation principle between electrodes and have developed a planar conveyance actuators array. The elementary actuator is of type II digital actuator. The Figure I-13 illustrates the cross-sectional structure of the actuator. The electrostatic principle is used to orientate air-flows used to move the conveyed object. The actuator is composed of two silicon substrates. The top substrate is a through-hole for air-flow. The bottom substrate consists of a movable part with suspension beams electrodes. It has one stable position (middle position) and two discrete positions (left and right position). Without energy supply, the movable part stays in the center position (stable position). The electrodes on the left and right side are used to switch the mobile part. When the electrode on the right side is supplied, the movable part is driven toward the right side (right discrete position), the left-hand side hole of the movable part opens to eject the air to the right (Figure I-13-b). On the contrary, when the electrode on the left side is supplied, the movable part is driven toward the right side (right discrete position), the left-hand side hole of

the movable part opens to eject the air to the right. A number of these elementary actuators has been assembled together and formed a planar conveyance device. This application will be explained in detail in section I.3.2.2.3.

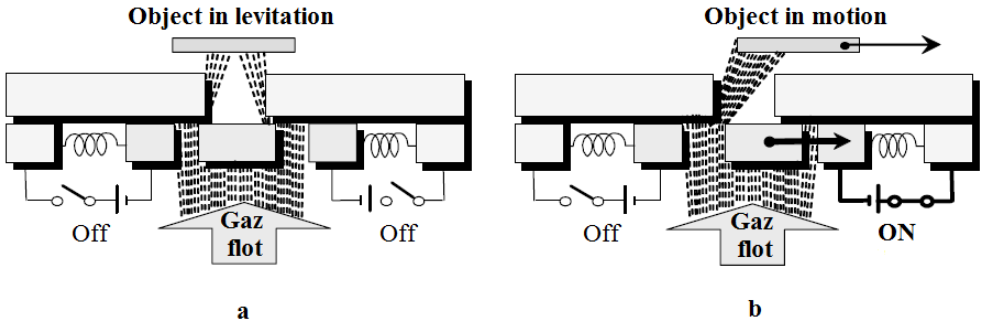


Fig I-13: Principle of the air-flow micro actuator, CHAPUIS et al. [CHAP 2004]: a. No control of the actuator, b. Control on the right of the actuator snooze

I.2.1.4. Piezoelectric Principle

Digital actuators based on piezoelectricity phenomenon are also used to realize the switching function. However, it is much less encountered than the other mentioned principles. Piezoelectricity is the ability of some materials (notably crystal, certain ceramics, and biological matter such as bone, DNA and various proteins) to generate a difference of electric potential in response to the applied mechanical stress. The effect is closely related to the appearance of an electric dipole density within the material's volume. An applied stress induces charge surface densities on the electrodes deposited onto the piezoelectric material. Piezoelectric effect is also a reversible effect, such as the production of the stress or strain under the applied difference of electric potential can be observed. This inverse piezo-effect can be utilized for actuation. Piezoelectric actuators provide several advantages, i.e. instant response, high energy conversion and etc. However, the main drawback is the small displacement capacity [GIAN 2007].

In literatures, the most common way to use the piezoelectric principle is to integrate piezoelectric material to some bistable structures or mechanism like bucked-beam or some laminates. Cazottes et al. [CAZO 2008] have designed a digital actuator using the property of a piezoelectric material in his study. MFC (Macro-Fiber Composite) is attached to a precompressed bistable buckled-beam as shown in the Figure I-14-a. When the MFC is supplied with external input electric energy, an extension generated by the MFC is applied to the skin of the beam all along the MFC active area. The beam is then switched from the upward stable position to the downward discrete position. To keep this discrete position, a

continuous energy supply is needed. When the supplied electric energy is removed, the MFC will shrink and force the beam back to the upward stable position. This actuator is then grouped in the type II because it has one stable position and one discrete position. Giddings et al. [GIDD 2011] and Portela et al. [PORT 2008] have integrated the MFC to a laminate as shown in Figure I-14-b and c, to realize the switching of a bistable actuator. Both of the two laminates can be switched between two states (one discrete position and one stable position). They are then regrouped in the type II digital actuators.

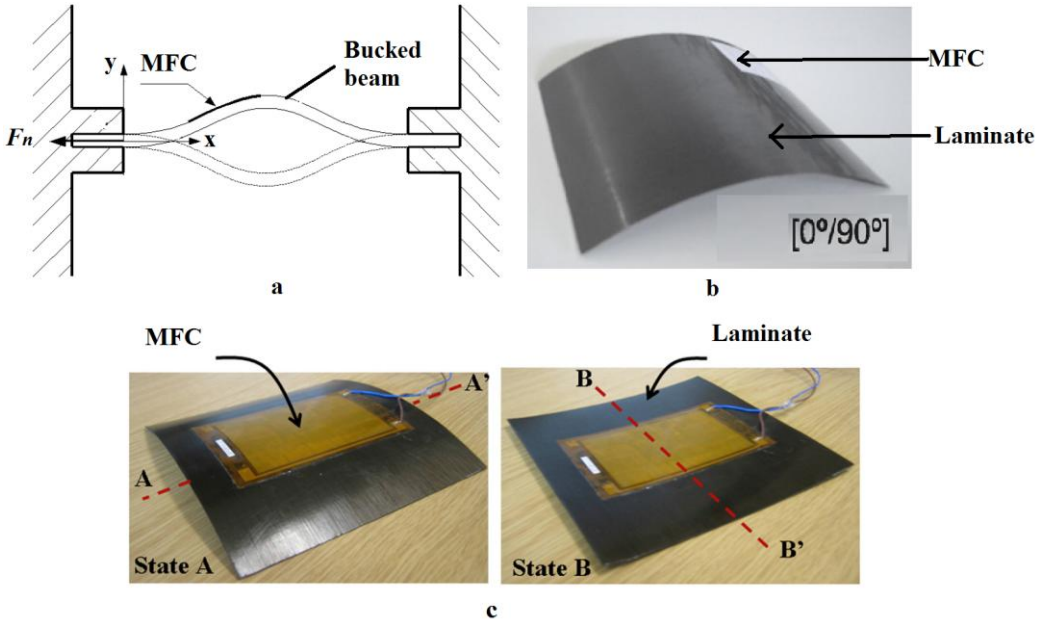


Fig I-14: Piezoelectric actuator: a. Cazottes et al. [CAZO 2008]
b. Giddings et al. [GIDD 2011], c. Portela et al. [PORT 2008]

I.2.2. Holding Methods

In this section, the holding function of the digital actuator is presented. Holding function is the second important function of digital actuators. This function ensures a holding of the mobile part in discrete or stable positions. It gives the mobile part some immunity to the external force.

In literature, the technological solutions to realize the holding function can be found in various forms, i.e., magnetic holding, buckled-beam holding, holding based on another mechanism or actuator, etc... These different holding principles have one advantage in common: continuous external energy supply is not needed to hold the actuators mobile part at their stable positions. However in some situation, actuators based on a continuous switching function to realize the holding function of the mobile part in discrete position can also be

found. These actuators then have the disadvantage of continuous energy consumption during holding when compared to the other mentioned holding forms. In the following part, the different principles to realize the holding function in digital actuators are explained in detail with examples.

I.2.2.1. Magnetic holding principle

The magnetic holding principle is based on the generation of a magnetic interaction force between magnetic materials. It can be realized in different forms: interaction between permanent magnets, between permanent magnet and ferromagnetic parts, using a magnetic circuit etc... The holding solutions based on a magnetic principle do not consume external energy for the holding of the mobile part in stable positions. The main advantages of this holding principle are the easy realization and utilization. In the following paragraphs, several examples of magnetic holding in digital actuators are presented.

Zhao et al. [ZHAO 2013] have developed a type III tristable actuator based on a magnetic holding principle. This mechanism can be switched among three stable positions by sensing outer acceleration exerted on the mobile part. A moving magnet is fixed at the extremity of a cantilever. Magnetic interaction force between one mobile magnet and three fixed magnets has been used to realize the holding function as shown in Figure I-15. Three fixed magnets have been added at the three stable positions. When the mobile part is switched from one to another stable position, the nearer fixed magnet attracts and holds the mobile magnet. The holding function is then realized.

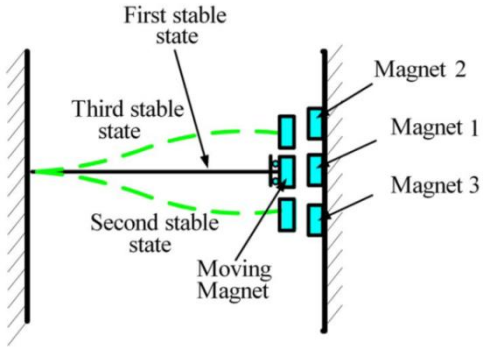


Fig I-15: Cross section view of micro actuator, Zhao et al. [ZHAO 2013]

Magnetic holding force can also be realized by interaction force between a permanent magnet and ferromagnetic parts. Barth et al. [BART 2012] (see Figure I-16-a) and Yang et al. [YANG 2011] (see Figure I-16-b) have developed digital actuators using the magnetic holding

principle with ferromagnetic parts. Barth et al. [BART 2012] have developed a bistable magnetic latched microvalve which consists of a mobile part composed of two SMA microbridges, a Permanent Magnet (PM) and a fixed part which consists of two soft-magnetic layers. The PM has been added to the mobile part and the two small soft-magnetic layers have also been added on the upper side and the lower side of the actuator. When the mobile part is switched up or down, magnetic attraction force (holding force) is generated between the PM and the soft-magnetic layer. The holding of the mobile part in stable position is then realized. The overall dimensions of the prototype are 11 mm × 6 mm × 3 mm. Yang et al. [YANG 2011] have also designed and manufactured a bistable micro-valve with the magnetic holding principle. The actuator consists of a PMMA housing, two ring permanent magnets, two pistons and a magnet. When the soft magnet is switched upward, it drives the upper piston upward. The upper sealing membrane is then deformed and blocks the upper flow channel. The upper flow channel is closed. Due to magnetic attraction force between the upper ring magnet and the soft magnet, the upper stable position of the piston is held. Similarly, when the soft magnet is switched downward, the lower flow channel is closed. The overall dimensions of the prototype are 26 mm × 26 mm × 10.9 mm. These two digital actuators belong to the type III digital actuators due to their two stable positions, i.e., up and down.

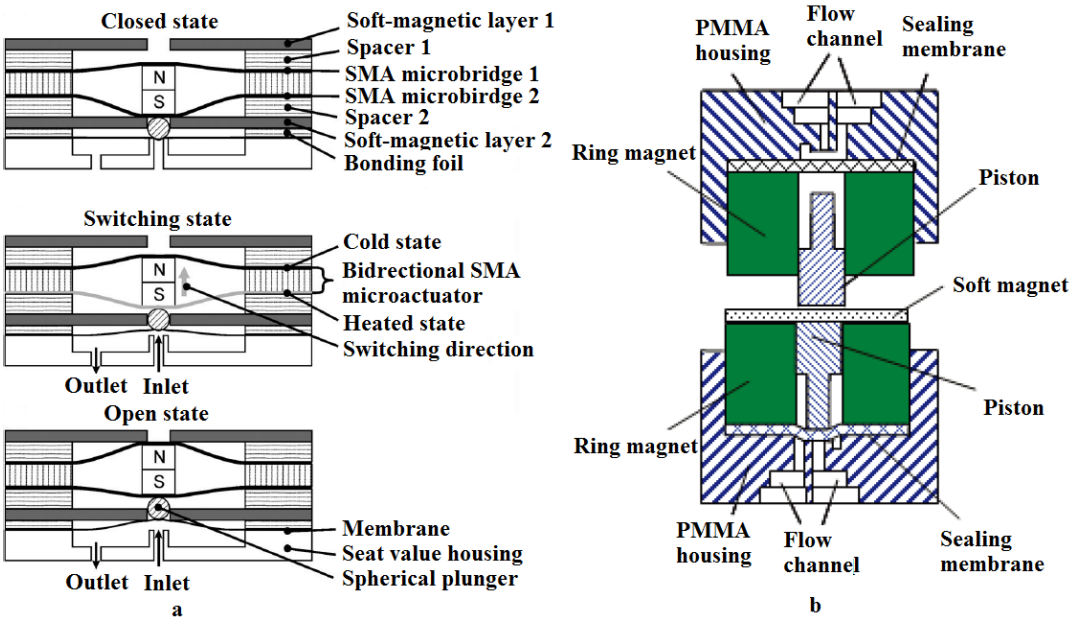


Fig I-16: Cross section view of micro actuator,
a. Barth et al. [BART 2012]
b. Yang et al. [YANG 2011]

I.2.2.2. Buckled structure holding principle

In literature, digital actuators which use buckled structure for the holding are often

encountered. One of the well-known bistable mechanical structures is a buckled beam or membrane [PARK 2008]. The holding function of these types of digital actuators is based on the properties of the beams or membranes which deform. The inner stress of the beam or membrane generated by the deformation ensures the bistability of these structures. The holding function is then realized without the need of external input energy. In the following paragraphs, several examples are discussed to present digital actuators with holding realized by the buckled beam structures.

Park et al. [PARK 2008] (see Figure I-17) have presented a type III pre-shaped buckled–beam actuator with two stable positions. The holding of the stable positions is ensured by the inner stress of the buckled-beam structure. This beam has been realized in copper material using micro fabrication technology with dimensions of 3000 µm × 10 µm × 25 µm. Due to the properties of the pre-shaped buckled-beam structure, this actuator has a high repeatability level of stable positions as it can show bistability characteristic at least up to 10 KHz when a bipolar square-wave switching current is applied to control it.

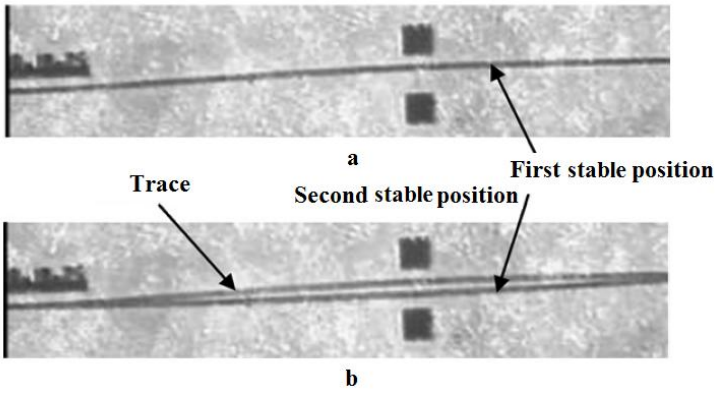


Fig I-17: a. the first stable postion b. the second stable position
Park et al. [PARK 2008]

Pham et al. [PHAM 2011] (See Figure I-18-a) and Gerson et al. [GERS 2012] (see Figure I-18-b) have developed two digital actuators based on buckle beam structures. In these two studies, more than two stable positions have been obtained by a combination of buckled-beams. Pham has developed a quadristable mechanism which combined two bistable mechanisms. The four stable states are illustrated in Figure I-18, 1-4. In Figure I-18-b, Gerson has developed a long displacement multistable micro actuator with serially connected flexible bistable buckled beams. This multistable actuator is driven with an electrostatic switching principle (not shown in Figure I-18). This kind of design gives the possibility to obtain digital actuators with high number of stable positions. The number of stable positions depends on the

number of the connected beams and is 2^n where n represents the number of connected beams. These two examples of digital actuators belongs to the type III digital actuators.

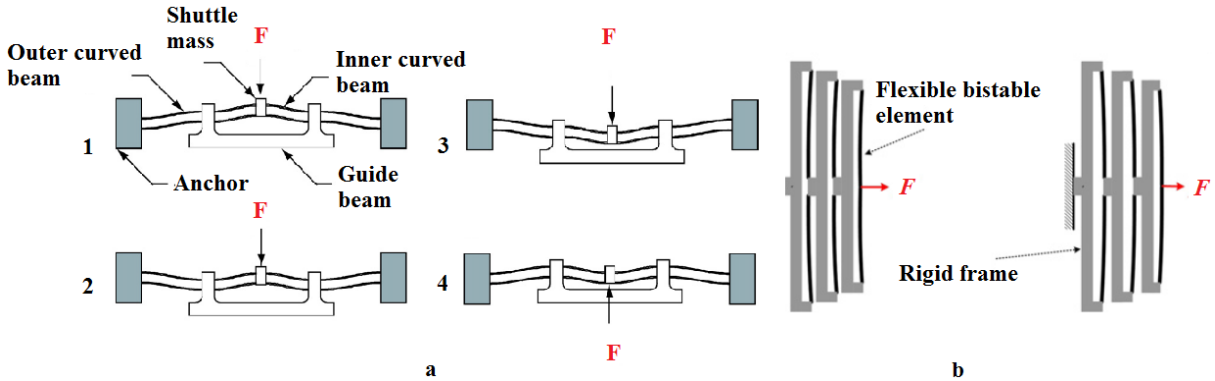


Fig I-18:a. Pham et al. [PHAM 2011]
b. Gerson et al. [GERS 2012]

I.2.2.3. Holding function realized via complex mechanism/external actuators

The third method to realize the holding function of digital actuators consists in adding external locking mechanisms or actuated device. Chen et al. [CHEN 2011] have developed a micro-fabricated bistable module for digital micro-robotics (not shown in figure). In this design, a stop block has been developed to guarantee the repeatability of the two stable positions and to limit the mobile part (see Figure I-19). The mechanism consists of two stop blocks placed at each extremity of the mobile part and two deformable beams fabricated on a central shuttle. Due to monolithic microfabrication of the overall module, a first activation is necessary to insert the mobile part of the actuator between the two stops blocks. Then the switching of the central shuttle is thermally obtained (not shown in the figure).

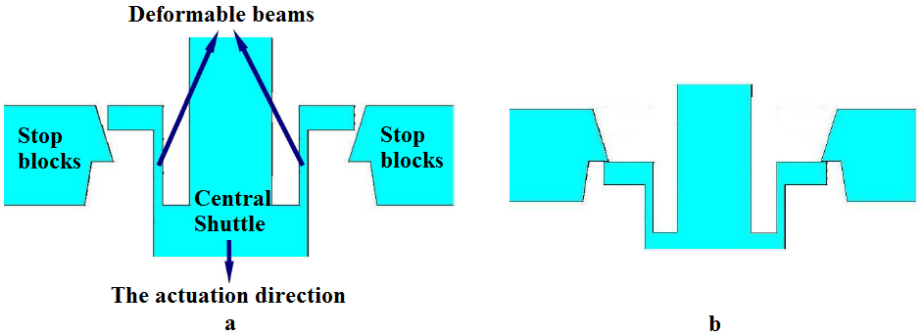


Fig I-19: a. First discrete position b. Second discrete position, Chen et al. [CHEN 2011]

Driesen et al. [DRIE 2010] (see Figure I-20-a), Cochran et al. [COCH 2005] (see Figure I-20-b) and Oberhammer et al. [OBER 2006] (see Figure I-20-c) have developed digital actuators with locking actuators. Driesen et al. [DRIE 2010] have developed a Nickel-plated thermal

switch with electrostatic latch. In this switch, a thermal actuator (part A in Figure I-20-a) is used for the switching and an electrostatic actuator (part B in Figure I-20-b) for the holding. One plate of the electrostatic actuator is connected to the mobile part and the other one is fixed. When the switching of the thermal actuator is done, the holding is actuated by the electrostatic actuator (capacitor) in a contactless way.

In other studies holding function have been realized in mechanic contact way. For example, Cochran et al. [COCH 2005] have developed an optical microswitch based on electrothermal actuators for the switching and the holding functions. During the switching, the locking actuator is drawn back. The switching actuator is switched upward or downward to move the spring supported slider. Then, the position of the output fiber is moved upward (close state) or downward (open state). The locking actuator inserts in the groove of the slider and holds the slider position.

Oberhammer et al. [OBER 2006] have developed an actuator composed of four electrostatic actuators to realize the switching and holding functions. This switch has one stable position and two discrete positions (center position, left position and right position) (Figure I-20-c). The switching and holding functions are realized by the electrostatic actuator [V1 and V2] and [V0 and V3] respectively. When there is no switching command, the mobile part of the actuator stays in the center stable position. When V1/V2 switching actuator is actuated, the mobile switched to the left/right side, respectively. After the switch, the holding actuator V0/ V3 is actuated. The mobile part of the V0/V3 is switched and in contact with V1/V2. Due to the mechanic hooking between the V1/V02 and V0/V3, the holding function is then realized. These three studies are all regrouped in the type II digital actuators.

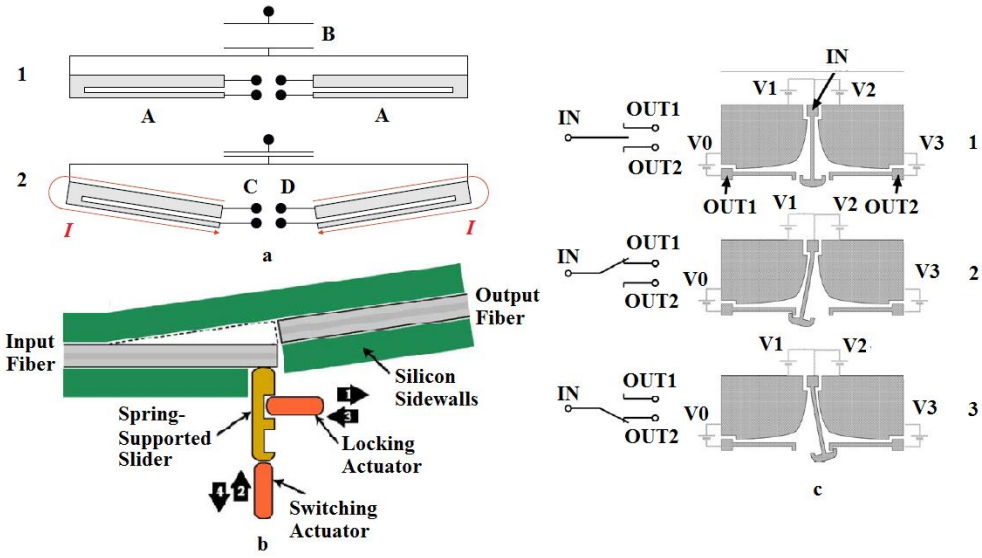


Fig I-20: Actuator locking with another actuator:
a. Driesen et al. [DRIE 2010], b. Cochran et al. [COCH 2005], c. Oberhammer et al. [OBER 2006]

I.2.2.4. Holding function realized via continuous switching function

As it has been presented previously, digital actuator holding function can also be realized via continuous switching function. Herding et al. [HERD 2004] has developed an optical switch (see Figure I-21) based on the movement of an optical fiber. This device is composed of an input fiber, two output fibers and two fixed electrodes which are placed on both sides of the input fiber. The input fiber is normally in the center position and covered with a conductive metal layer. To switch the input fiber, voltage is applied between one of the two electrodes and the metal layer. Due to the electrostatic force, the input fiber is attracted and bent to one side. The input fiber and the output fiber are then connected. Signal can then be transmitted until the voltage is cut off, the input fiber will return to its center position. As a result, this switching function (electrostatic actuation) has to be continuously applied in order to maintain the discrete positions. This actuator is regrouped in the type II digital actuators. Besides, the devices developed by Cazottes et al. [CAZO 2008], Giddings et al. [GIDD 2011] and Portela et al. [PORT 2008], which have been presented previously in this chapter, also realize the holding function via continuous switching function.

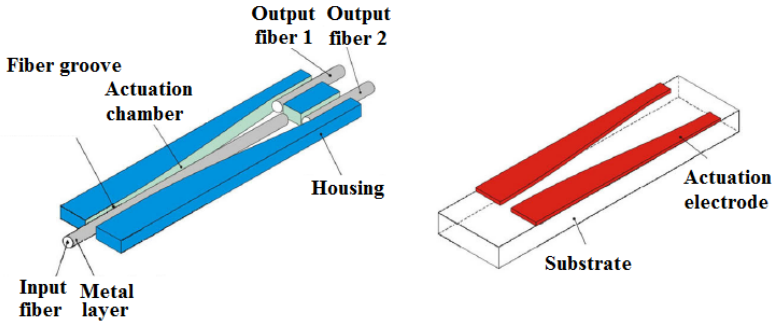


Fig I-21: Actuator holding via switching: Herding et al. [HERD 2004]

In this section, the two basic functions of digital actuators have been presented: the switching and holding functions. For the switching function, the physical principles used in literature including electromagnetic, electro-thermal, electrostatic and piezoelectric have been presented. For the electromagnetic principle, the main advantages include high speed, fast response, simple design and low cost [KHAN 2014]. The thermal switching principle has the advantage to exhibit strong forces but the main drawbacks include temperature dependency, slow actuation and control difficulties [ZAID 2011]. The electrostatic switching principle provides contactless actuation but the main drawback of these actuators is their limited stroke. The piezoelectric switching principle provides the advantages of instant response and high energy conversion. However, the main drawback is the small displacement capacity [GIAN 2007].

For the holding function, magnetic holding, buckle-beam holding and external mechanism/actuator holding principles have been presented. The magnetic holding function provides a contactless holding function but added magnets, ferromagnetic materials or magnetic circuits have to be integrated. The buckle-beam holding principle is based on deformation properties to realize the holding function. No additional element is needed to realize the holding. Holding with an external mechanism/actuator holding principle provides huge holding force but extra input energy is necessary. The integration of the external mechanism/actuator may also be complex. Holding function realized via switching function is also available but continuous energy has to be applied which is its main drawback.

Based on these different switching and holding principles, various actuator designs have been realized and used in different applications. In the following section, applications of digital actuators are presented and classified into two major categories. These two application categories will be presented in detail with examples.

I.3. Applications

Digital actuators are widely used in lot of domains. Their applications can be divided into two major groups, the single actuations and the multiple actuations [PETI 2012]. The single actuation regroups applications based on only one single digital actuator. For the multiple actuations, several actuators are integrated together in order to realize complex tasks. They could collaborate with each other or work separately without collaboration. In this part, the two major groups of digital actuator applications will be presented and illustrated with examples.

I.3.1. Single Actuation

Single actuation application regroups devices composed of only one digital actuator. The number of discrete positions is then limited for this type of application. In literature, the main applications based on a single actuation are the devices aimed for discrete displacement, switches, etc. In this section, the application of the single actuation will be presented by their functionality.

I.3.1.1. Discrete displacement output

In literature, actuators have been encountered which are aimed for discrete displacement output. The digital actuators can assure a stable fixed output displacement with high repeatability. This behavior is due to its digital functioning based on a discrete displacement of a mobile part between well known and repeatable positions.

Chalvet et al. [CHAL 2013] have developed a microfabricated planar digital microrobot for precise positioning based on a bistable module (see Figure I-22). This device is based on a thermal switching principle. With the actuation of the thermal actuator, the bistable structure (mobile part) can move between two stop blocks (stable positions). The dimensions of the module are 9 mm in width, 2 mm in height and maximum thickness of 500 µm. It can output a precise vertical displacement of 10 µm. This actuator belongs to the type III digital actuators.

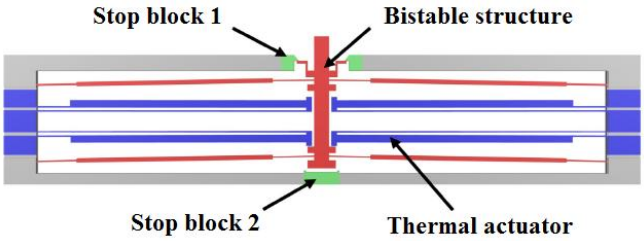


Fig I-22: Bistable Module, Chalvet et al. [CHAL 2013]

In another study, Wingert et al. [WING 2006] (see Figure I-23) have presented a digital mechatronic device based on bistable elements with a high stroke (8 mm) compared to [CHAL 2013]. This device consists of a thin elastic film sandwiched between compliant electrodes and four linear bistable elements (LBE). When a voltage is applied across the electrodes, the electrostatic forces cause the film to expand. One discrete position is obtained (Figure I-23-b). When the voltage supply is cut off, the film compresses and the stable position is reached (Figure I-23-a). This actuator is part of the type II digital actuators.

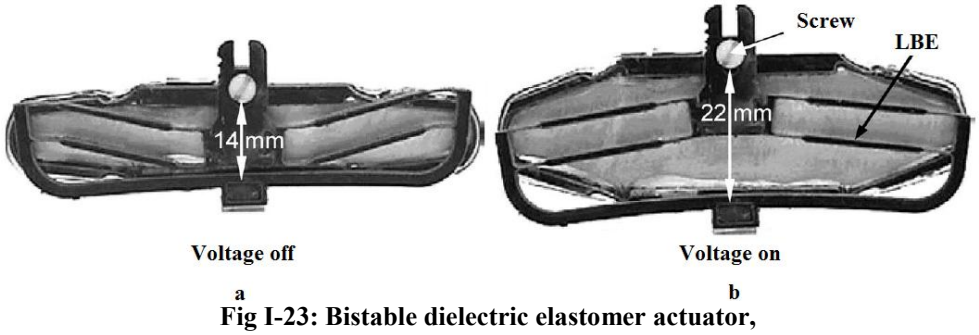


Fig I-23: Bistable dielectric elastomer actuator, Wingert et al. [WING 2006]

Chouinard et al. [CHOU 2012] have developed a type III bistable actuator for binary robotics (Figure I-24). In this actuator, two prestretched elastomer films with compliant electrodes located at each side (cell 1 and cell 2) (one side fixed and the other one attached to the mobile part) can be expanded with actuation voltage. A bidirectional rotation of the mobile part can be obtained by actuating separately the two films. The maximum rotation (± 40°) of the center piece is limited by the stopper situated along both sides (see Figure I-24-b).

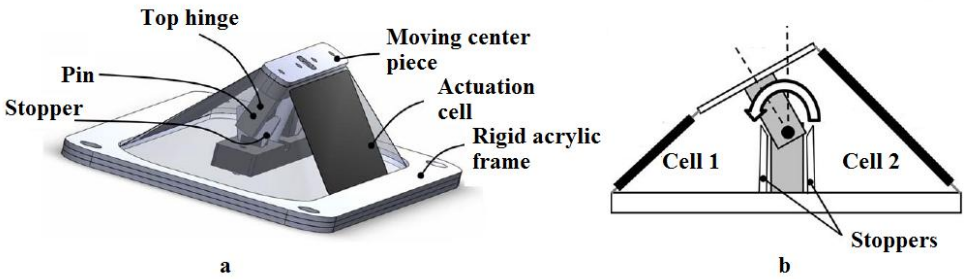


Fig I-24: Discrete displacement for rotation, Chouinard et al. [CHOU 2012]

I.3.1.2. Mechanical Switch

Another application of single actuation is the realization of mechanical switches. Switches are usually used as a key part of control elements. Digital actuators have been used to realize different types of switches for fluidic, optical and electrical applications. In this section, single digital actuator used for switches are presented in detail.

I.3.1.2.1. Fludic Switch

In literature, digital actuators have been used for fluidic switch with different switching principles, such as thermal principle, electromagnetic principle, electrostatic principle, etc... In the following text, several examples of fluidic switches based on digital actuators are presented.

Ogden et al. [OGDE 2012] (see Figure I-25) have developed a latchable actuator which is used as high-pressure valves based on thermal switching principle. In Figure I-25, the blue, white and red parts represent the solid low-melting-point (LMA), the solid paraffin and the molten material (both paraffin and LMA) respectively. The switching function of the actuator is based on the solid-to-liquid phase transition of paraffin and of the LMA. When the paraffin and LMA are both heated, the paraffin and the LMA are molten. The valve is then closed due to the expansion of paraffin and LMA (Figure I-25, 1-2). The holding function is achieved due to the different solidifying temperature of paraffin and LMA. When the heat is cut off, the LMA is solidified before the paraffin. The valve then stays closed (Figure I-25, 3-4). The actuator has been fabricated using standard batch-processes as photochemical machining, wet etching and photolithography. It consumes a switching energy of 0.14 mW and can sustain a pressure of 1.8 MPa. The dimensions of the actuator are 7.5 mm × 7.5 mm × 0.5 mm. This actuator belongs to the type III digital actuator.

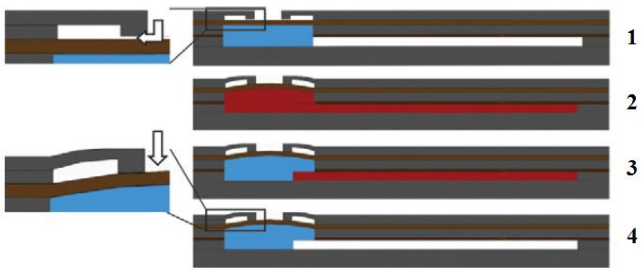


Fig I-25: Cross section view of the fluidic switch, Ogden et al. [OGDE 2012]

The digital actuator developed by Hues et al. [HUES 2010] (Figure I-9) has also been developed for fluidic switch application. [LUHA 2008] (Figure I-5) and [YANG 2011] (Figure I-16-b) have used the electromagnetic switching principle and designed a micro fluid valve (switch) based on digital actuation.

I.3.1.2.2. Optical Switch

Digital actuators have been used in optical applications as optical switches. According to literature, numerous solutions have been employed to realize these switches. For example, Liao et al. [LIAO 2010] (Figure I-26) have developed an optical switch using electromagnetic bistable actuators. The optical switch consists in a monolithically micro machined silicon micro-mirror structure (Figure I-26-a) and two mini-actuators (Figure I-26-c). Each electromagnetic actuator consists in a ferromagnetic seesaw, a permanent magnet, an electromagnetic coil and two stoppers. It is connected with mirror structure via the L-shape arm. The switching function is realized by electromagnetic force between the seesaw and the electromagnetic coil when a current is passed through the coil. Two stable positions are obtained upon different driving current directions. The holding function is realized with the magnetic force between the permanent magnet and the seesaw. The bistable electromagnetic actuators can then move the mirrors with cantilevers which realize the switch the light path. The switching time of the switch is less than 13 ms.

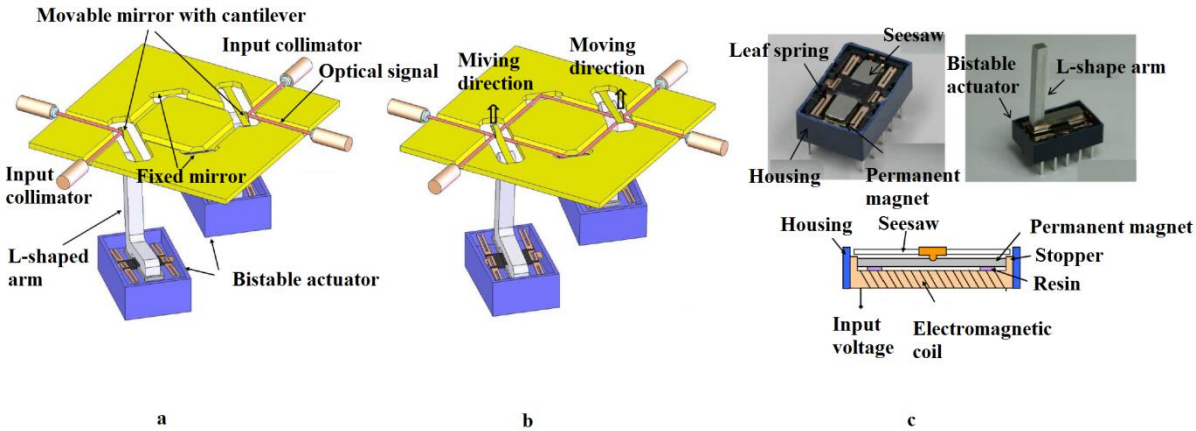


Fig I-26: Operational principles: Liao et al. [LIAO 2010]: a. the bar state, b. the cross state, c. digital actuator

In another study, Michael et al. [MICH 2008] have developed a bistable micro bridge of type III actuator for optical switching applications of planar waveguides. The micro bridge consists of a beam with two springs integrated on both sides. The switching of the micro bridge is obtained using thermal switching principle. When the bridge is heated, it expands and

compresses the spring (Figure I-27-a). The deflection of the beam reduces and the bridge flattens (Figure I-27-b). When the bridge is cooled, the compressive stress in the beam starts to build up and causes downward deflection. The bridge remains in the buckled-down stable position (Figure I-27-c) after cooling. The holding function of this actuator is ensured by the buckled-beam structure. The micro bridge has been micro fabricated with SiO_2 using Plasma Enhanced Chemically Vapor Deposition (PECVD) technology. The switching time is 1 ms with a 7 V voltage pulse.

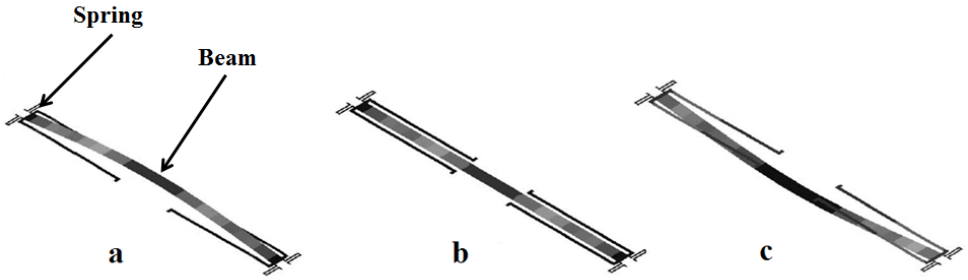


Fig I-27: Michael et al. [MICH 2008]

The digital actuator based on thermally actuation principle developed by Barth et al. [BART 2012] (see Figure I-16-a) and Cochran et al. [COCH 2005] (see Figure I-20-b) were also designed for optical switching applications.

I.3.1.2.3. Electrical Switch

Digital actuators have been developed to realize low cost, highly stable and low energy consuming electrical switches. As previously mentioned, numerous solutions based on different switching principle (e.g., electromagnetic, thermal, etc.) have been employed to realize electrical switches.

Miao et al. [MIAO 2011] have developed a bistable electromagnetic actuator for electrical switching. The actuator consists of a permanent magnet loaded microspring (mobile part) separated by an air gap from the microcoil using SU-8 spacers (see Figure I-28). The switching function of the actuator is realized using electromagnetic force between the permanent magnet and the microcoil. Positive or negative current can be sent through the coil, electromagnetic force is then generated to attract or repulse the permanent magnet. Two stable positions (upper side and lower side) are then achieved. At the upper or lower position, the contactors are cut off/linked, the electrical switch is then in OFF/ON state. The holding function has been realized in two different methods for maintaining the upper and lower

stable positions. For the upper and lower stable position, the holding function is realized by the spring force and magnetic force respectively. The switching time for the actuator is about 4.7 ms.

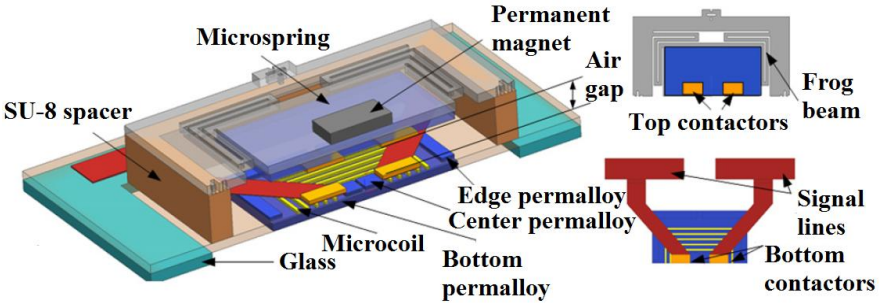


Fig I-28: Bistable electromagnetic actuator, Miao et al. [MIAO 2011]

Mao et al. [MAO 2010] (see Figure I-29) have developed a latching bistable micro thermal actuator for electrical switching applications. The actuator consists of two bimorph electro-thermal beams, conductive electric and metal contacts pair. The switching of the actuator between the on and off states is realized in 5 steps illustrated in Figure I-29, 1-5. The two beams are heated and cooled in a consecutive order. The beams are deformed or reformed to let the contact pair contact or off contact, respectively. The holding function is obtained by the mechanical contact force between the contact pair.

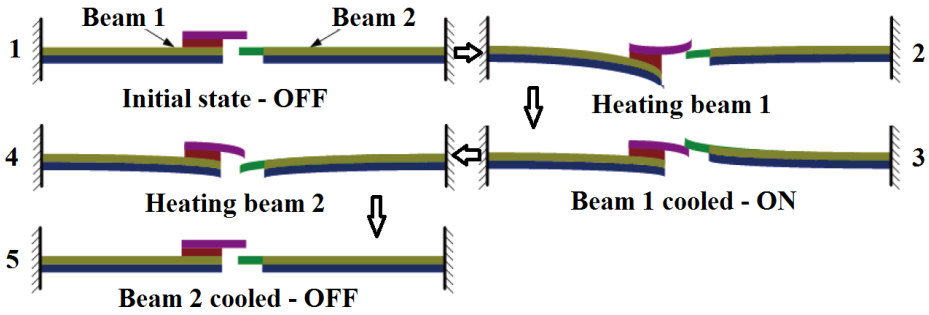


Fig I-29: Working process of bistable actuator, Mao et al. [MAO 2010]

I.3.2. Multiple actuation based applications

Assemblies of digital actuators can also be fund in literature. The assemblies of actuators can provide more discrete positions compared to the single actuation and are then able to accomplish complex applications. These assemblies are able to perform actions obtained by combination of several elementary actions. The applications of these assemblies are detailed in this section. Based on the working method, multiple actuation applications can be classified into two types. The first one regroups multiple applications where each elementary actuator works independently without collaboration with others actuators. In this case, a task can be

accomplished by each elementary actuator. The second type regroups multiple applications where there is collaboration between the elementary actuators. The task can then be realized by contribution of all the elementary actuators.

I.3.2.1. Multiple application without collaboration

In this section, the multiple applications focusing on arrangement of several actuators which work independently without collaboration is presented. In literature, several applications have been developed such as tactile display, optical switch array, mechanical memories, etc...

I.3.2.1.1. Tactile display

Tactile display systems are composed of digital basic modules controlled independently and placed one beside the other to form an array. In this application, each elementary module has the ability to move a pin between a lower position/input and a high position/output. Such devices can, for example, display messages in Braille to be read by contact between the fingers and the pads. Vitushinsky et al. [VITU 2009] have developed an array of bistable thin-film shape memory actuators for application in tactile display. The array consists of 100 elementary actuators arranged in a 10 × 10 matrix form (see Figure I-30-a). Each elementary actuator (see Figure I-30-b) consists of a buckled thin-film composite with active SMA (Ti-Ni-Hf) layers (mobile part) and a passive metal carrier layer (fixed part). The active SMA layer is connected to a pin placed on it. Based on a thermal switching principle, the active SMA can be switched between two stable positions (up and down) and then drives the pin up and down. The holding function of the two positions is realized with buckled thin-film composite. The dimensions of the prototype designed array are of 20-30 mm width and 30-35 mm length.

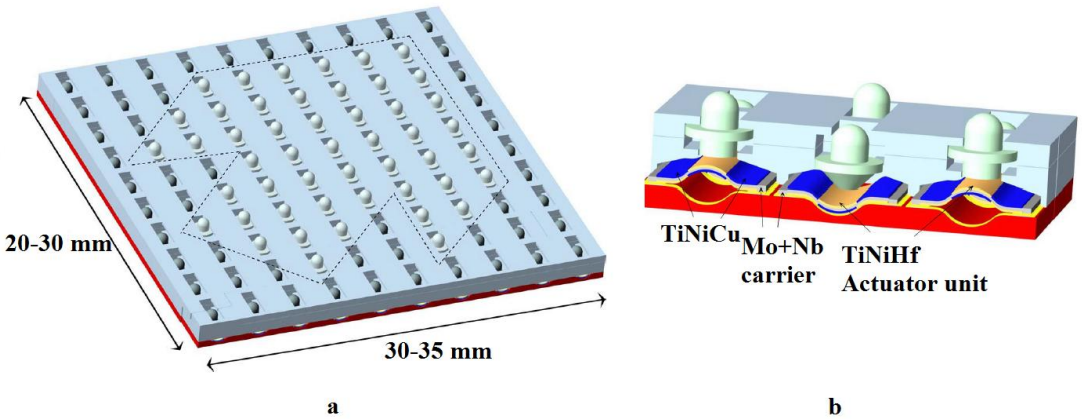


Fig I-30: 10 x 10 pixel actuators array, Vitushinsky et al. [VITU 2009]

Matsunaga et al. [MATS 2013] have developed a 10 × 10 SMA micro-coil actuators array (see Figure I-31-a) for tactile display application. The elementary actuator (see Figure I-31-b) consists of a magnetic latch, two SMA micro-coils and a driving circuit. A pin cap is attached to a shaft which is connected with the SMA. The moving parts of the actuator (SMA micro-coils) can be switched thanks to a thermal switching principle. The holding function is realized by magnetic attraction force between magnetic tubes and the PM (magnetic latch). For the prototype design, the stroke of each elementary actuator is 2 mm.

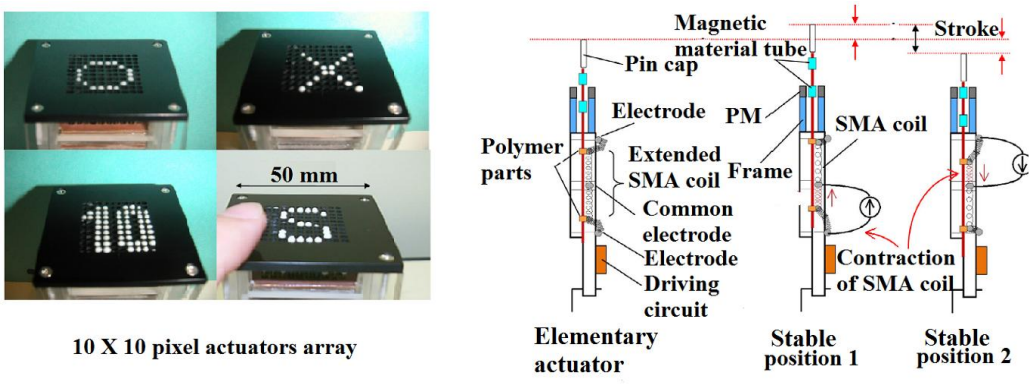


Fig I-31: 10 x 10 pixel array, Matsunaga et al. [MATS 2013]

I.3.2.1.2. Optical Switch array

In literature, optical switch array composed of several digital actuators have also been developed. Jia et al. [JIA 2009] have developed a silicon-based 8 × 8 MEMS optical switch array (Figure I-32-a) by assembly of 64 electrostatic elementary actuators. Each elementary actuator (see Figure I-32-b) is composed of two electrodes (not shown in figure), a mirror and a torsion beam. One electrode is integrated into the beam and the second one is placed under the beam. The mirror is fixed on the cantilever beam and is parallel to the torsion beam. Thanks to the electrostatic switching principle, the beam can be switched between two positions (bar state and cross-state). When one of the elementary actuator is actuated, the corresponding incoming optical signal is reflected to the selected output port. A switching time less than 6 ms and an actuating voltage of about 65 V have been reported by the author.

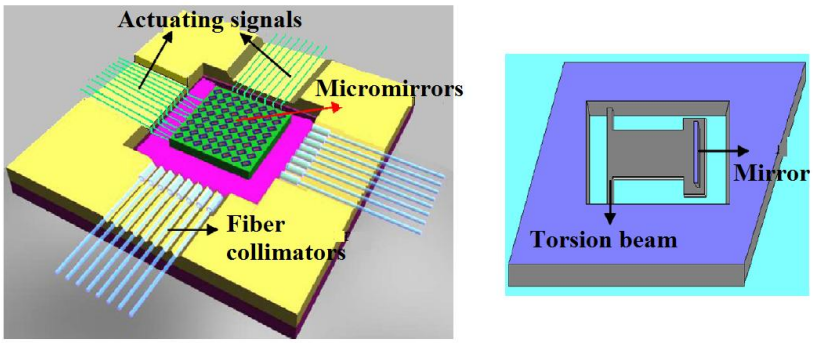


Fig I-32: Overview of 8 x 8 MEMS optical switch array, Jia et al. [JIA 2009]

I.3.2.1.3. Mechanical memories

Another type of multiple actuation application is the realization of micromechanical or nanomechanical memories. Tsuchiya et al. [TSUC 2006] have developed a nanomechanical memory device (see Figure I-33) incorporating nanocrystalline Si (nc-Si) dots which can realize high-speed and nonvolatile memory operation. The device (Figure I-33-a) consists of 100 electrostatic switched elementary actuators. Each element actuator (Figure I-33-b) is a suspended floating gate beam (mobile part) placed in a cavity and under a gate electrode. The floating gate beam contains the nc-Si dots as charge storage. When the gate voltage is applied, the floating gate beam moves, thanks to electrostatic interactions between the gate electrode and the charge in the nc-Si dots. Two stable positions (upward and downward) can then be achieved. The holding function is realized based on a buckled structure of the beam. This device can achieve a switching speed of 1 GHz which is a high speed for the operation of memory storage.

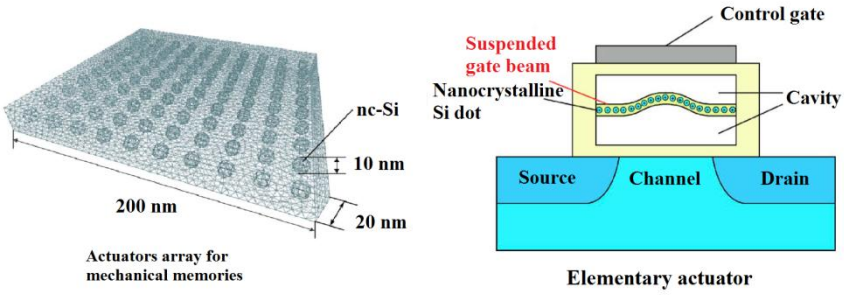


Fig I-33: Mechanical memories array, Tsuchyia et al. [TSUC 2006]

I.3.2.2. Multiple application with collaboration

In this section, multiple applications focusing on arrangement of several actuators which work with collaboration is presented. In literature, many types of applications have been developed based on the collaboration of several assembled elementary actuators such as digital robots, digital to analog converters, displacement table, etc…

I.3.2.2.1. Digital robots

In literature, digital robots composed by elementary modules are often encountered to be actuated by digital actuators. Digital robots can then benefit from the advantages of digital actuators presented early in this chapter. One simple digital robot can be actuated by the collaboration between minimum two digital actuators. Kim et al. [WONK 2010] have developed a flytrap robot (Figure I-34) based on two elementary actuators. The robot consists of two bistable laminated composite structure (bistable leaf), two SMA coil spring actuators, a clamping bolt, Y-shaped holder and two acryl plates. The SMA coil spring actuators are based on the electrothermal switching principle. When the two actuators are cooled or heated simultaneously, the robot succeeds in winging one time. The holding function is ensured by bistable leafs. It has been reported by the author that one fly motion takes about 100 ms to be accomplished.

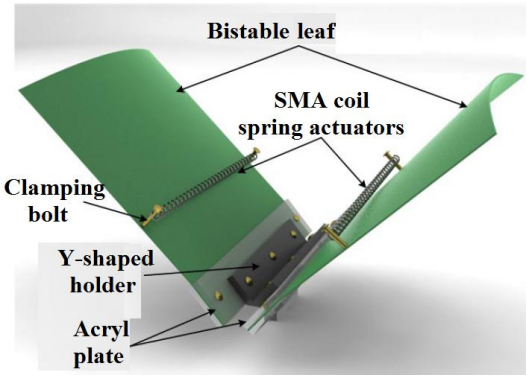


Fig I-34: Flytrap robot, Won kim et al. [WONK 2010]

In another study, Wang et al. [WANG 2011] have developed a binary driven hyper-redundant robot platform (Figure I-35-a) via a more complex combination of elementary actuators. This platform consists of six elementary actuators (Figure I-35-b). Based on the electromagnetic switching principle, each elementary actuator can be switched between two stable positions (upward and downward). The plate form can then perform $2^6 = 64$ stable positions using different combinations of elementary actuators states.

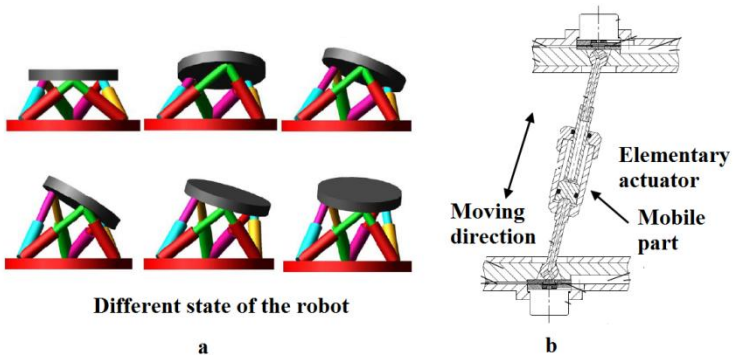


Fig I-35: a. Digital Robotics platform, b. elementary actuator, Wang et al. [WANG 2011]

I.3.2.2.2. Digital to analog converters

In literature, digital-to-analog converters realized using digital actuators have also been developed. In these devices, each elementary digital actuator corresponds to a digital bit. Zhou et al. [ZHOU 2004] have developed a 3 bits micromechanical digital-to-analog converter. This device is composed of three elementary actuators which are actuated by electrostatic principle. Each actuator is switched and held with the help of 2 pairs of driving and holding electrodes which are placed on both sides of the movable part respectively (see Figure I-36-a). All the elementary actuators are connected to a rigid platform via torsional beam (Figure I-36-b). The bit information is shown in Figure I-34-c, 8 digital states can be obtained with a combination of 3 elements actuators. Zhou et al. have fabricated an experimental device which consists in two basic bits and experimentally validated the principle.

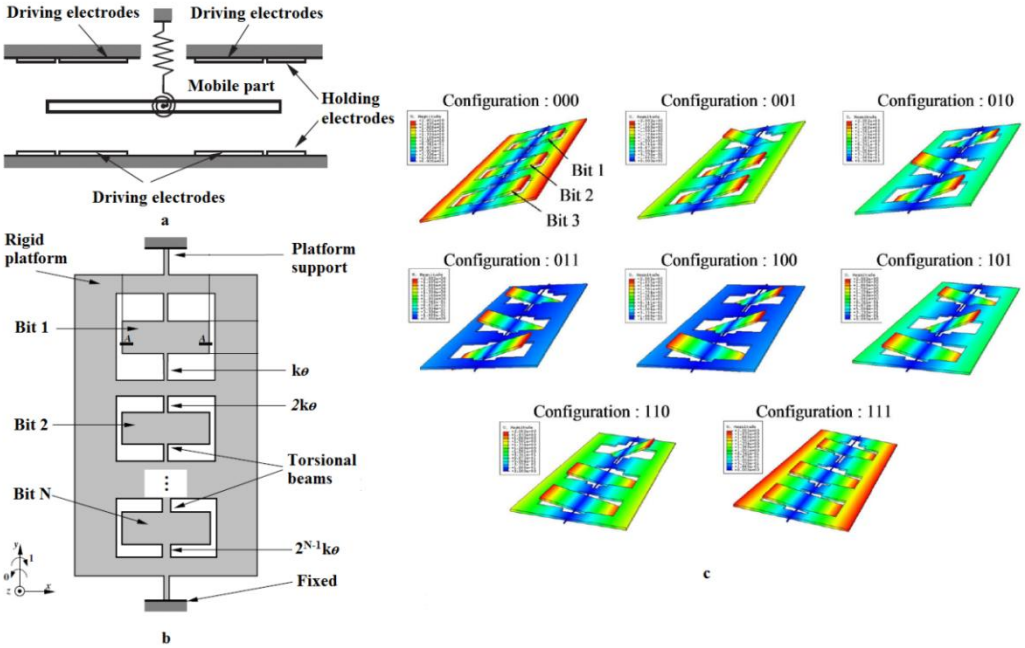


Fig I-36: Schematic illustration of digital to analog converter, Zhou et al. [ZHOU 2004]:a. Front view of the elementary actuator, b. Top view of the elementary actuator, c. Different states of the device

I.3.2.2.3. Displacement table

Cooperation of many actuators makes it possible to convey a micro object relatively larger than each micro actuator component [CHAP 2004]. In literature, displacement tables composed of many digital actuators which are able to convey an object have been developed. Chapuis et al. [CHAP 2004] (Figure I-37) have developed a displacement table composed of electrostatic elementary actuators (see Figure I-13). A prototype composed of 169 actuators and with dimensions of 13 mm × 13mm has been developed.

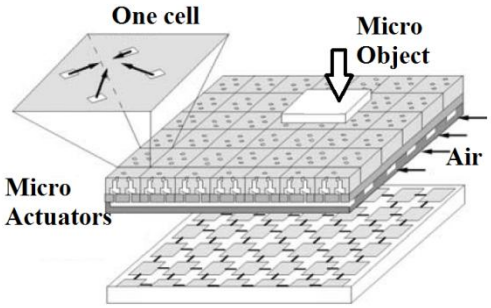


Fig I-37: Displacement table, Chapuis et al. [CHAP 2004]

PETIT et al. [PETI 2009] (Figure I-38) have developed a digital actuators array composed of 25 elementary actuators for a planar object conveyance task. Each elementary actuator is actuated via the electromagnetic principle. The elementary actuator is composed of 4 fixed magnets and 1 mobile magnet (placed in a square cavity). The switching function is obtained thanks to the electromagnetic Lorentz force. Four stable positions have been obtained which are located at the four corners of the square cavity. The holding function is realized magnetically with the interaction between the mobile and the fixed magnets. A prototype array composed of 5 × 5 elementary actuators with a stroke of 200 µm has been developed.

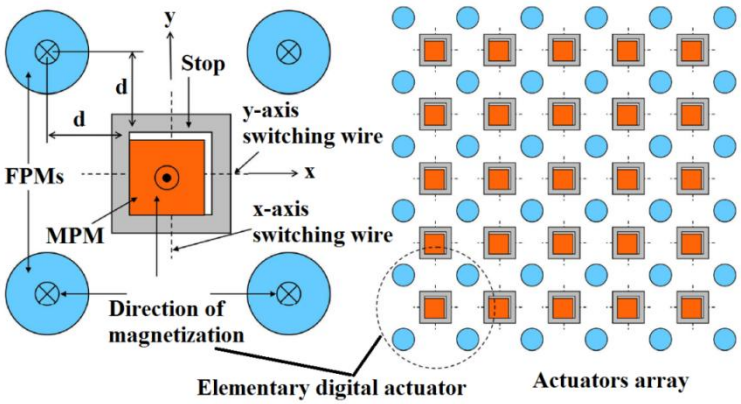


Fig I-38: Actuators array, Laurent PETIT al. [PETI 2009]

I.4. Conclusion

In this first chapter, a state of art focusing on digital actuation has been realized. A classification of the digital actuators has been proposed by the author that enables to regroup the digital actuators based on their properties (the number of stable positions it owns).

According to the state of the art, there are two elementary functions in digital actuators: the switching and the holding functions. For the switching function, four major physical principles have been used in literature: electromagnetic, electrostatic, thermal and piezoelectric. The electromagnetic principle is well suited as switching between stable positions because it has the advantages of high speed, simple design and low cost. The majority of digital actuators based on this principle have also a magnetic holding of their stable positions. This option simplifies then the architecture of these actuators because the magnetic properties of the mobile part are used as well as for the switching and the holding functions. The thermal principle is also adapted to the switching of digital actuators because it uses the expansion of materials (mostly solids) or phase change of some smart materials (SMA) when subjected to a heating source which is easy realized. However, slow response is always its main drawback. The electrostatic switching principle is based on the generation of attraction or repulsive force between two opposite or identical electric charges respectively. Due to the principle, it can provide contactless actuation but the main drawback is their dependency to the electrode facing surfaces area and the air gap in between. As a result, their working range (stroke) is always limited. The piezoelectricity switching principle is much less encountered than the other mentioned principles. It is based on the piezoelectricity of some materials to generate a difference of electric potential in response to the applied mechanical stress. It always provides the several advantages, i.e. instant response, high energy conversion and etc. However, the main drawback is the small displacement capacity [GIAN 2007].

In literature, four physical principles have been seen to realize the holding function of the digital actuators: the magnetic holding, buckle structures, holding function realized via complex mechanism/external actuators and holding function realized via continuous switching function. Magnetic holding principle is well suited to realize the holding function because it uses the magnetic interaction force between magnetic materials that does not consume external energy for the holding of the mobile part in stable positions. The main advantages of this holding principle are the easy realization and utilization. Holding function

realized by using buckled structures is also often encountered in literature. It is based on the utilization of inner stress of buckled beam or membrane which assures the holding function. As a result, the holding function can also be realized without any external energy input. However, specific materials have to be used and fabricated in beam/membrane shape. Compared to the other mentioned principles, holding via complex mechanism/external actuators is available but generally more difficult to implement. It requires the addition of a compliant structure or a holding actuator which increase the complexity both for the device and the control. While, holding via continuous switching function avoids the drawback of integrate more structures to the system. However, continuous energy input is required to maintain the switching function.

The Table I-1 provides a comparison of the different digital actuators properties presented in this chapter. Several performances indicators, properties and parameters are compared i.e. digital actuator types, size ("Dimensions"), stroke, switching time, energy consumption (Energy) and force or torque generated (F or C output). According to this table, it is visible that most of developed digital actuators have two stable positions (bistable actuators) and a millimeter scale in dimension. Based on different switching principle, their switching time varies from several microseconds to a few seconds. Their strokes are also different from each other which change from several micrometers to a few millimeters.

Based on the research of a former study realized at the Roberval laboratory of UTC [PETI 2009], a digital actuators array composed of 25 elementary digital actuators have been developed. Each elementary actuator has four stable positions with two orthogonal displacement directions. Thanks to the advantages of electromagnetic switching principle and magnetic holding principle, the switching function and the holding function can be easily realized without energy consumption for maintaining the mobile part in the stable positions.

The originality of the proposed actuators array is that the actuator structure is not composed of an assembly of two unidirectional actuation direction structures but directly a 2D structure. This 2D architecture reduces the potential assembly error of two unidirectional structures and simplifies the design of the array. Moreover, the potential application of the actuators array is focused on the planar conveyance. In this thesis, the principle, the modeling, fabrication prototype experimental results based on the planar conveyance application, dimensional optimization of the actuators array and the prospective will be presented respectively in the following chapters.

Reference	NSP	Dimensions (S) (L × W × H)	Stroke	Switching Time	Energy or Power	F or C Output
[ABAD09]	2	4 × 9 mm^2, 200µm	25°	-	-	-
[BART12]	2	7 × 7 × 4 mm^3	84 µm	-	-	33 mN
[CHOU12]	2	-	±40°	-	-	-
[GERS12]	2^n	-	80 µm	-	33 V	-
[HUES10]	2	-	±25 µm	-	1-2 J	-
[OGDE12]	2	7.5 × 7.5 × 0.5 mm^3	30 µm	-	0.14 mW	-
[PARK08]	2	3000 × 10 × 25 $µm^3$	20 µm	-	0.2 mW	10 µN-
[PHAM11]	4	-	-	-	-	-
[ZAID11]	2	3.6 × 5.8 × 0.25 mm^3	-	10-15s	70 mW	403 mN
[WING06]	2	-	8 mm	-	-	-
[YANG11]	2	-	40 µm	-	-	94 mN-
[CHAR08]	2	8 × 1.8 × h mm^3	-	-	90 V	-
[CHEN11]	2	6 × 6 × 3 mm^3	29 µm	0.37-1.38 s	12 mJ	-
[MIAO11]	2	-	380 µm	4.96 ms	25 mJ	-
[MORE10]	2	-	-	3.2 s	0.7 J	-
[WU10]	2	150 × 150 × 0.32 mm^3	-	-	-	-
[GIDD11]	1	Ø 3 mm	1 mm	50-75 s	-	-
[LUHA08]	2	3.4 × 6 × h mm^3	10°	-	-	1 µNm
[VITU09]	2	4 × 1 × h mm^3	700 µm	100 ms	80 mW	2.2 mN
[WANG09]	2	-	90 µm	1 ms	-	-
[LIAO10]	2	-	350 µm	3-12 ms	200 mW	-
[MAO10]	2	-	50 µm	-	-	2 mN-
[MICH08]	2	350 × 3 × 10 $µm^3$	31 µm	-	-	-
[PARE09]	2	-	20 µm	-	-	229 µN-
[WANG11]	2	240 × 80 × 160 mm^3	-	-	-	-
[WONK12]	2	-	-	100 ms	-	-
[MIRO07]	2	12 × 12 in^2	-	-	-	-
[CHAP04]	1	180 × 240 $µm^2$	15 µm	-	-	-
[BOHR96]	2	-	5 µm	-	-	10 µN
[COCH05]	2	3 × 50 mm^2	130 µm	40 ms	5280 mW	-
[CAZO08]	2	200 × 20 nm^2	-	-	-	-
[TSUC06]	2	8 × 300 × 200 nm^3	±50 µm	1 Ghz	-	-
[PETI09]	4	100 × 100 mm^2	200 µm	-	-	-
[ZHAN07]	2	2 × 2.2 mm^2	17 µm	20 µs	-	-
[WU11]	2	-	-	-	-	-
[DRIE11]	2	50 × 50 mm^2	-	30 ms	30mJ	-
[MATS13]	2	-	2 mm	0.3 s	-	-
[OBER06]	1	1 × 1 mm^2	-	400 µs	-	-
[HERD04]	1	-	65 µm	7 ms	50 V	-
[ZHAO13]	3	-	-	-	-	-
[CHAL13]	2	-	1.5 µm	-	-	-

NDP : Number of stable positions

Table I-1: Comparison of the presented digital actuators

Chapter 2: Principle and modelling of digital electromagnetic actuators array

In the former thesis [PETI 2009], an electromagnetic digital actuator with four discrete positions has been designed and developed. Static and dynamic models have been proposed to simulate the behaviour and characterize the performances of the actuators array. A prototype has been manufactured and its performances have been determined. Moreover, a comparison between experimental and simulated results has been done and has shown a good accordance. A digital actuators array composed of 25 identical elementary actuators arranged in matrix architecture has been designed and a prototype has been manufactured.

In this chapter, the principles of the elementary electromagnetic digital actuator and of the actuators array are presented. An application of this array as a planar conveyance device will be considered and tested in the present thesis. The principle of this application will then be also described in this chapter.

A static model of the actuators array has been developed and is presented in this chapter. This model has been used to characterize the array behaviour and an optimization study of the actuators array will be presented in Chapter IV using this model.

II.1. Actuators array architecture

II.1.1. Elementary actuator principle

The elementary actuator of the array is composed of a mobile and a fixed part. The mobile part is composed of a cubic Mobile Permanent Magnet (MPM). This MPM is placed in a square cavity and can move according to the fixed part which regroups four Fixed Permanent Magnets (FPMs) and two orthogonal wires (Figure II-1). The dimensions and the properties of the magnets are given in Table II-1. The MPM can reach the four corners of the cavity which correspond to the four stable positions of the actuator. The presented digital actuator has then two orthogonal and independent displacement axes that represent its main originality compared to the literature.

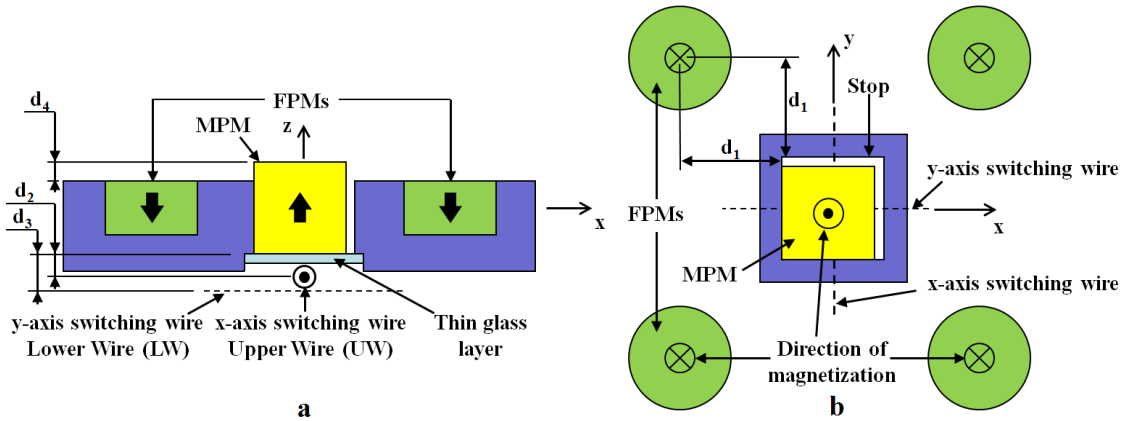


Fig II-1: a. Side view of the elementary digital actuator
b. Top view of the elementary digital actuator

Magnet	Dimensions		Magnetization
MPM	2 mm × 2 mm × 2 mm		1.45T
FPM	Ø2.26 mm × 1.25 mm		1.45T
MPM Stroke			0.2 × 0.2 mm^2
	Distances		
d_1	3850 µm	d_2	222 µm
d_3	458 µm	d_4	375 µm
	Material		Mass
MPM	NdFeB		0.06g
Square cavity	Aluminium		

Table II-1: Elementary digital actuator properties

The four FPMs placed around the cavity generate a magnetic holding force on the MPM along the two orthogonal axes. This force ensures a holding of the MPM in each corner of the square cavity without external energy supply. As a result, the four corners of the square cavity

are called stable positions.

To switch the MPM between the stable positions, two orthogonal electric wires placed below the square cavity are used. When a current passes through a wire surrounded by the magnetic flux density from the MPM, a Lorentz force is generated on the wire. Because the wire is fixed, the reaction force is exerted on the MPM which switches from one discrete position to another one. For the realization of the experimental prototype and to avoid any electrical contact between the two wires, a double side Printed Circuit Board (PCB) has been used (Figure II-2). With this technical solution, one wire, called Upper Wire (UW), is printed on the top side of the PCB and the other one, called Lower Wire (LW), on the bottom side. In this case, the distance between the UW and the bottom side of the MPM (distance d_2 in Figure II-1) is smaller than the distance between the LW and the bottom side of the MPM (distance d_3 in Figure II-1). Using the same current value, the electromagnetic generated force is then lower using the LW than using the UW. In order to reduce this force difference, the distance between the two wires, which corresponds to the PCB thickness, has been chosen as small as possible and is 200 µm. In order to avoid electrical contact between the MPM and the UW, a thin glass layer (thickness 170 µm) is placed between the MPM and the PCB. This thin glass layer ensures also a flat surface on which the MPM moves.

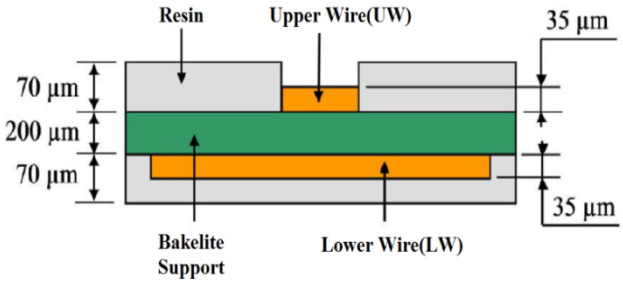


Fig II-2: Cross section of the PCB

The Figure II-3 illustrates two configurations of the MPM switching and holding. In Figure II-3-a, the MPM is initially placed in the (-x; -y) discrete position. To switch the MPM along the +y-axis direction, a current, called driving current, oriented along the +x-axis direction is sent through the LW (Figure II-3-b). This current generates a Lorentz force oriented along –y-axis on the LW. The driving force (resulting force) oriented along +y-axis is then exerted on the MPM. If the driving force is higher than the sum of the magnetic holding force along y-axis and the adhesion forces, the MPM switches (Figure II-3-c). To switch back the MPM (along -y-axis), the driving current direction is reversed and oriented along -x-axis. In the case

of a y-axis switching (using the LW to generate the driving force), a second current, called holding current, can be injected through the UW in order to increase the lateral contact force between the MPM and the lateral stop. In Figure II-3(e-f), the MPM is initially placed in the (-x; +y) position and is switched to the (-x; -y) position with a driving current through the LW and oriented along -x-axis. In this configuration, a holding current is sent through the UW and oriented along +y-axis. This holding force can be interesting to ensure the lateral contact between the MPM and the stop during the switch then to reduce the straightness error or the influence of external disturbances.

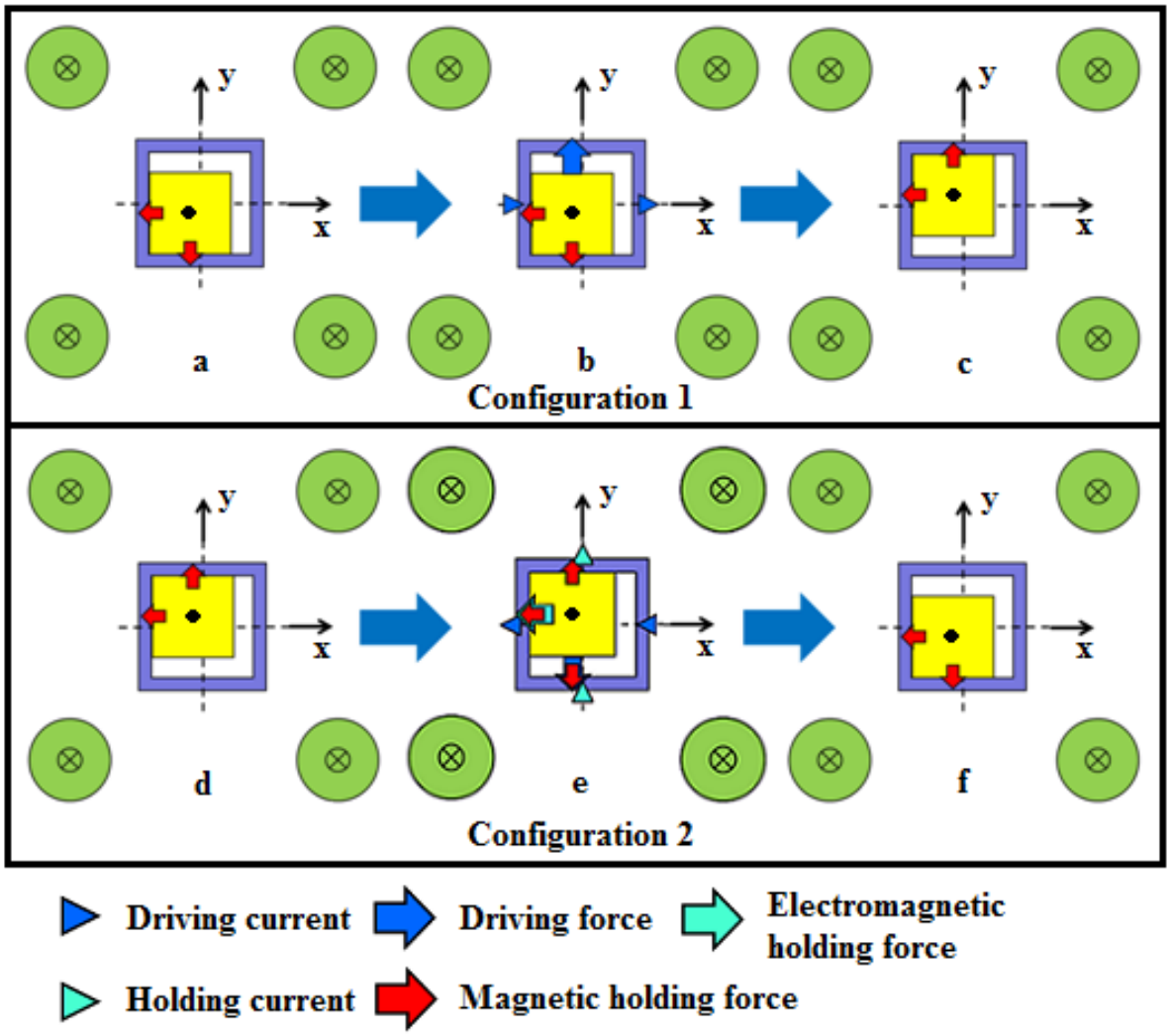


Fig II-3: a-c. MPM switching in + x direction
e-g. MPM switching in the – x direction with holding current

Upon this principle, two displacement directions and four discrete positions can be achieved. However, the actuation possibility of a single digital actuator is limited. An actuators array composed of several elementary actuators offer the possibility to realize complex actions. The

principle of an actuator array composed of several elementary digital actuators is presented in the following section.

II.1.2. Actuators array principle

In this section, the principle of the digital actuators array is presented. The design of the array has been realized in the former thesis [PETI 2009]. During the design, the interactions between the elementary actuators have been considered. A model has been developed using the Mathematica software to compute the electromagnetic and magnetic forces present in the array. A matrix architecture (Figure II-5) has been chosen for the array because the elementary actuator has a square geometry.

In order to validate the principle, an array architecture composed of 25 elementary actuators regrouped in a 5 × 5 matrix form has been selected. In order to reduce the size of the array, two adjacent actuators share the FPMs situated at their boundaries. In order to ensure a magnetic equilibrium of all elementary actuators of the array, additional FPMs (AFPMs) are added around the array. The AFPMs help to balance the magnetic force exerted on the elementary actuator located at the boundaries of the array. The characteristics of AFPMs have been determined in the previous study [PETI 2009]. 84 AFPMs have been used for the prototype design and have been divided into three rows in a square pattern at the boundary of the array. These three rows include 24, 28, 32 AFPMs respectively. The AFPMs of the first and third rows have the same magnetization orientation as the MPMs. The AFPMs of the second row have the same magnetization orientation as the FPMs. If the array was larger (more than 5 × 5 elementary actuators), the AFPMs of the first and third rows and of the second rows will correspond to MPMs and FPMs respectively. The dimensions of the AFPMs and the distances between the three AFPMs rows are given in Table II-2. For the prototype design, the AFPMs magnetizations and the distances between the three AFPMs rows (d_5, d_6 and d_7) are identical for all the AFPMs.

AFPMs	Dimensions	Magnetization
1 row	Ø2.26 mm × 2 mm	1.45T
2 row	Ø2.26 mm × 1.25 mm	1.45T
3 row	Ø2.26 mm × 2 mm	1.45T
Distance (d_5, d_6, d_7)	4.95 mm	

Table II-2: Additional magnets dimensions

A schematic layout of the array is provided in Figure II-4-a where all MPMs are placed in the

lower-left corner ($-x_{MPM}$; $-y_{MPM}$). In order to ensure the magnetic equilibrium of the MPM along the vertical direction (z-axis), the centers of gravity of all the PMs (MPMs, FPMs and AFPMs) are placed at the same position along this axis (Figure II-4-b). The manufacturing of the mechanical support of the array has been realized using conventional machining. All the fixed PMs (FPMs and AFPMs) of the array have a cylindrical shape in order to facilitate the manufacturing of the mechanical support of the array.

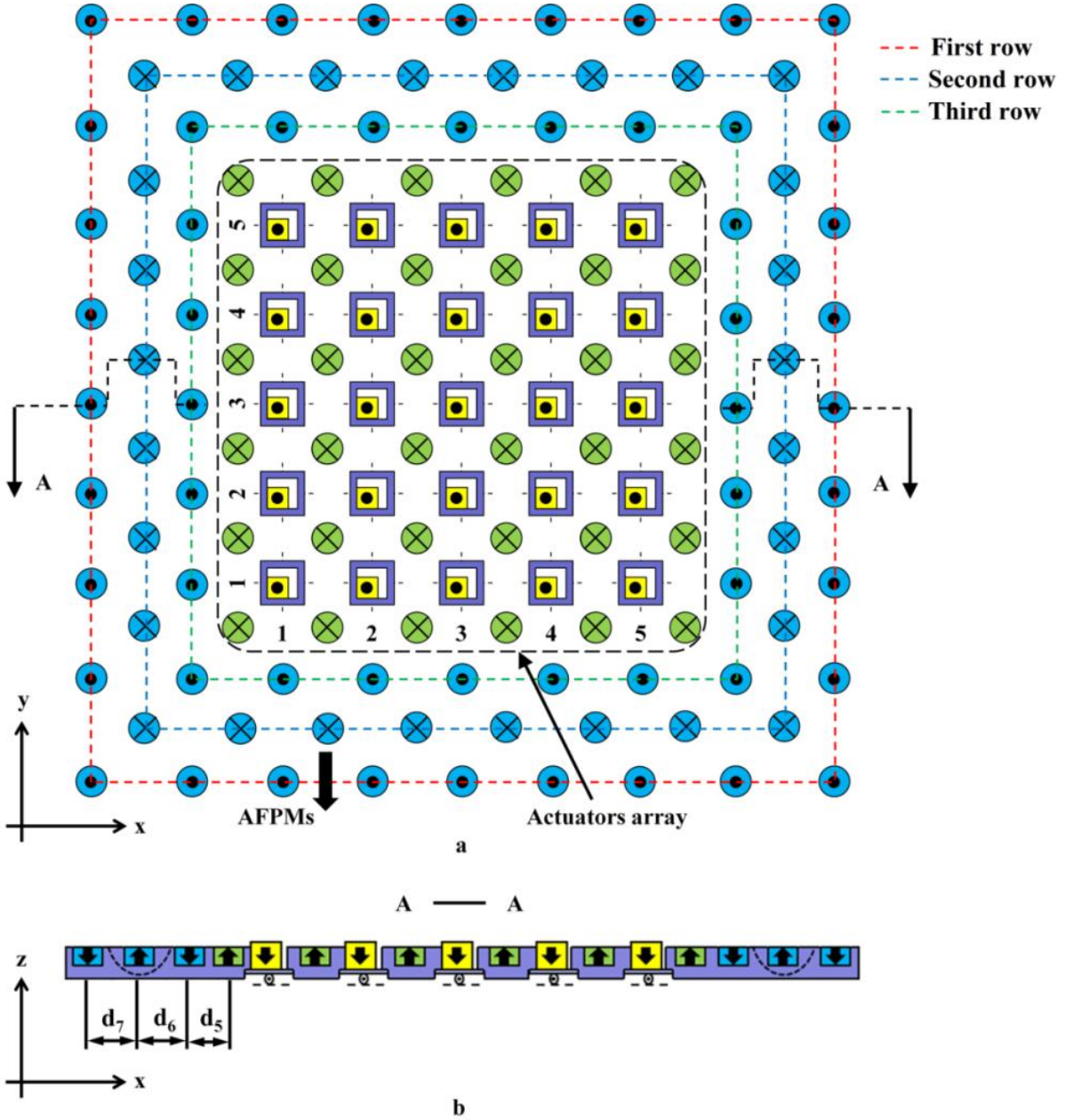


Fig II-4: Schematic layout of the digital actuators array
a. Top view of the array
b. Front view of the array

II.1.3. Application of the array

Compared to a single elementary actuator, a digital actuators array is able to realize complex tasks by combining elementary actions. In the present thesis, an application of the array has been studied and characterized. This application consists of a planar displacement table. In this application, a thin plate is placed on the top side of the array and is in contact with the top side of all MPMs. To move the plate, the displacement strategy illustrated in Figure II-5 has been used. This figure represents a side view of an array composed of only 3 × 3 in order to facilitate the understanding.

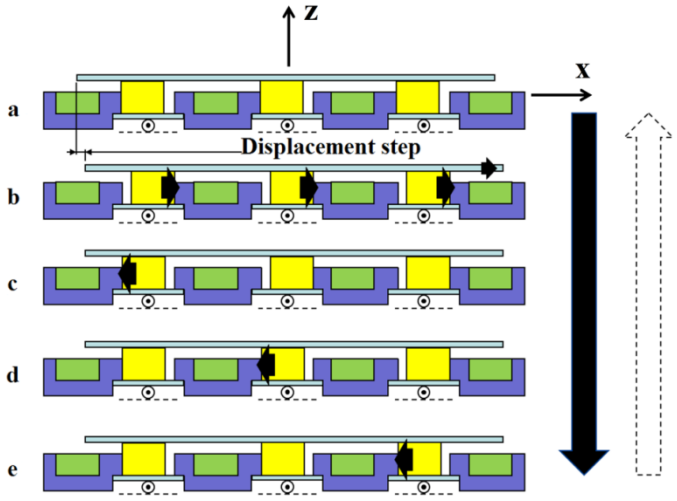


Fig II-5: Front view of the sequence for a plate displacement

The Figure II-5-a represents the initial configuration of the array. In this configuration, all the MPMs are located in the same initial position. At the first step (Figure II-5-b), all the MPMs are switched simultaneously in the same direction. At this step, the plate is moved in the same direction as the MPMs thanks to the friction force between the MPMs and the plate. At the next steps (Figure II-5c-e), the MPMs are switched alternatively in the reverse direction so that they reach the initial position. During these steps, there is no plate displacement because the friction force between the switched MPM and the plate is not high enough to move it. When all MPMs are back to their initial positions, a second displacement sequence can be realized. Using this displacement strategy, the actuators array is able to move the plate in the plane on long distances. The stroke of this displacement table is only limited by the size of the array.

The Figure II-6 represents the possible plate displacements using the array. In Figure II-6-a and b, plate displacements along x and y-axes are presented. These displacements are

obtained with a switch of all MPMs along the same direction (x or y). A diagonal plate displacement is also possible by switching all the MPMs along the two directions at the same time (Figure II-6-c).

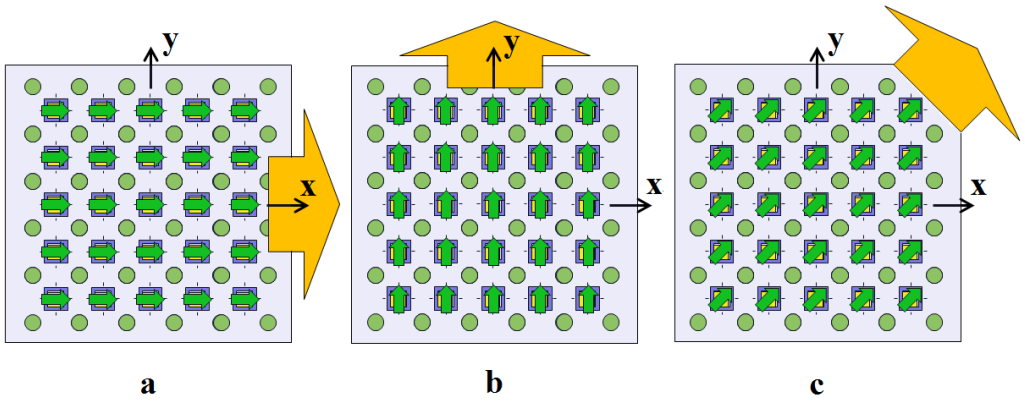


Fig II-6: a. Top view of displacement in x direction
b. Top view of displacement in y direction
c. Top view of displacement in diagonal direction

Plate rotations can also be obtained as represented in Figure II-7. Three examples of controlling strategies are presented. In Figure II-7-a and b, plate rotations can be obtained by a combination of MPMs switches along x and y direction respectively. The Figure II-7-c presents a more complex MPMs switch combination to realize a plate rotation. With the combination, the MPMs at the corners of the array are switched in the diagonal direction and the other ones are switched either along x-axis or y-axis. With the three configurations, plate rotations can all be achieved. However, with the third configuration, a better rotation performance of the plate can be achieved compared to the first and second configuration. With this configuration, there is less friction force between the plate and the MPMs compared to the first and the second configuration. Meanwhile, more energy will also be needed for the third configuration because several elementary actuators have to be controlled along two displacement axes. In Figure II-7, clockwise rotations are presented but counter clockwise rotations can be obtained by inversing the switching directions of the MPMs.

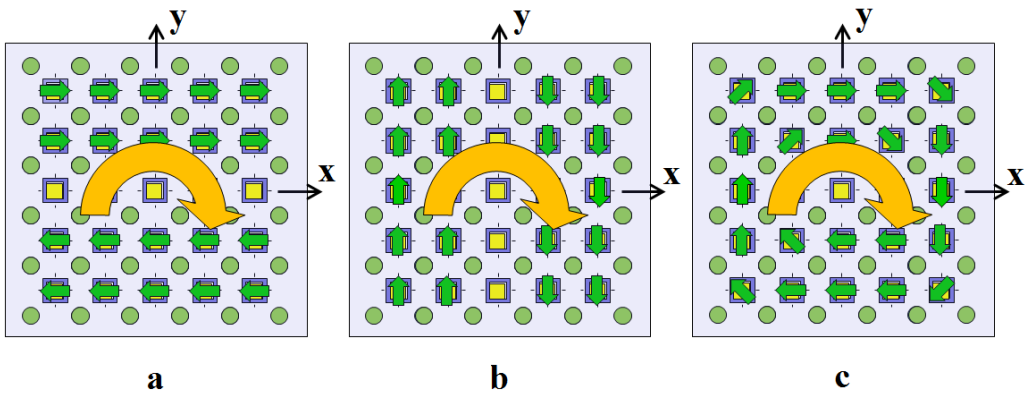


Fig II-7: Rotation application in three different forms (a – c)

II.2. Modelling of the array

In this section, two static magnetic modelling of the array which takes into account of all the magnetic forces exerted on the MPMs are presented. These two models have been used to characterize the array.

II.2.1. Choice of modeling tools

Two static models of the array have been developed using two softwares. Firstly, a semi-analytical model has been developed in MATHEMATICA software by using the RADIA package. Secondly, an analytic model has been developed in MATLAB software. These two static modelling are both needed because they have different uses. The first modelling helps to characterize the array and the second one is used to design and optimize the array as it is easier to be integrated into other optimization algorithm.

The first software used is RADIA, a semi-analytical electromagnetic computing software based on the MATHEMATICA environment. This software has been selected due to its simple use and the possibility to obtain a rapid visualization of the modelled objects that is an important parameter because the considered array is composed of many PMs [PETI 2009]. RADIA is based on a method of limit integration which is different from methods based on finite element calculation. With this method, there is no need to mesh the magnet field and integrations of the field can be calculated directly using the analytical equations [ELLA 1997]. The volume objects are created and divided into sub-objects for which the software solves the general problem in terms of magnetization. The objective of the RADIA model is to

determine the static magnetic forces exerted on each MPM of the array. In addition, this model helps to understand the physical phenomena observed in the experiments (presented in Chapter III). Furthermore, this model has also been used to verify the correctness of the second model.

The second used software is MATLAB. With this software, an analytical model of the array has been developed. The objective of this model is to calculate the total magnetic forces exerted on each MPM in the array. Furthermore, this model has been developed in order to be integrated into a global MATLAB program able to determine the influence of manufacturing errors on the array behaviour (chapter III). In chapter IV, this model has also been integrated with an optimization algorithm to optimize the array design.

Both of these two static models are able to calculate the magnetic forces exerted on each MPM. They have been used to compute the forces exerted on each MPM in order to ensure that each elementary actuator is working with a homogeneous behaviour (e.g., holding force). At this point, in both of these two models, several hypotheses have been considered. The geometries and dimensions of all PMs are considered perfect and their magnetization uniform and oriented along the z-axis.

Moreover, in order to facilitate the magnetic computation with the two models, the FPMs and AFPMs shape have been considered as cuboid shape instead of cylindrical shape. In [PETI 2009], it has been verified that the hypothesis is valid for PMs with the same volume and the same magnetization value. The dimensions of the FPMs and AFPMs considered in the two models are presented in Table II-3. In this chapter, manufacturing errors of the PMs and of the square cavity have not been taken into account. In the next chapter, a study on the influence of the manufacturing errors while considering the prototype configuration will be presented in detail. In the following section, the two models are separately presented.

PMs	Dimensions
MPMs	$2.00 \times 2.00 \times 2.00$ mm^3
FPMs	$2.00 \times 2.00 \times 1.25$ mm^3
AFPM1	$2.00 \times 2.00 \times 2.00$ mm^3
AFPM2	$2.00 \times 2.00 \times 1.25$ mm^3
AFPM3	$2.00 \times 2.00 \times 2.00$ mm^3

Table II-3: FPMs and AFPMs dimensions considered in the two models

II.2.2. Semi-analytical modeling with RADIA

The static model of the digital actuators array developed with RADIA has been firstly studied. In the Figure II-8, a 3D view of the array is presented thanks to the quick visualization of RADIA. The red, blue and green cuboid shapes represent the MPMs, FPMs and AFPMs, respectively.

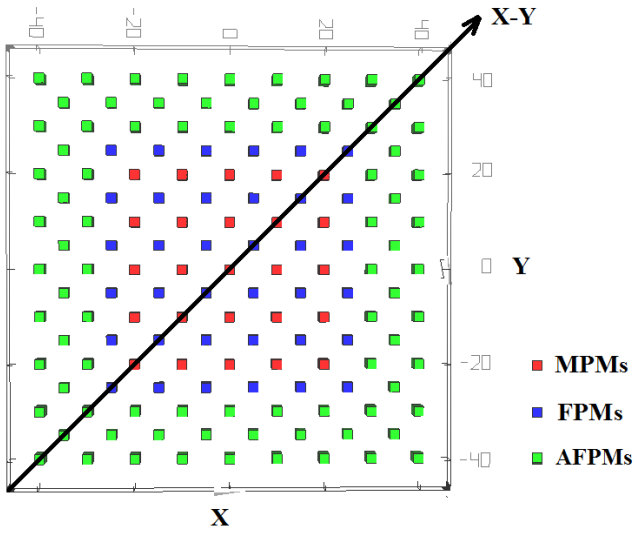


Fig II-8: 3D view of the actuators array in RADIA

It has been previously presented that the application of the digital actuators array is based on the contribution of each elementary actuator. A homogeneous behaviour of all elementary actuators is then crucial. The calculation of the magnetic forces exerted on all the MPMs of the array has then been realized using this model. A magnetic force is exerted on each MPM by the influence of the MPMs, the FPMs and the AFPMs. By using this RADIA model, the magnetic forces generated by the three types of PMs have been calculated separately. In the following sections, the magnetic forces generated from the FPMs, the MPMs, the AFPMs and the total magnetic force over the array will be presented separately.

II.2.2.1. Magnetic holding force

In this section, the magnetic holding forces exerted by the FPMs on each MPM of the array are presented. As it has been presented previously, the magnetic holding force ensures the holding function of the MPMs in their stable positions. In this study, the magnetic holding forces exerted on each MPM are only considered (array configuration show in Figure II-9). The magnetic forces along x- and y-axis exerted by the FPMs on the 25 MPMs have then been computed and are presented in Figure II-10.

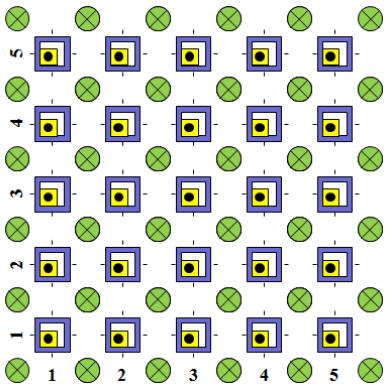
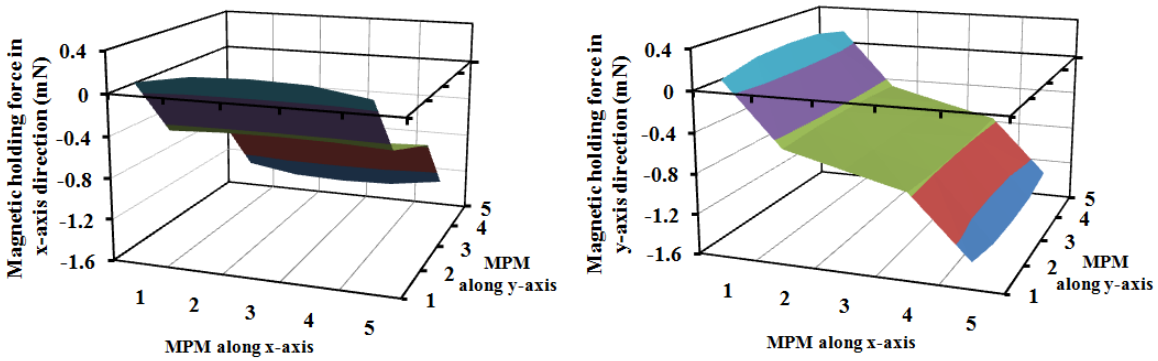


Figure II-9: Array configuration considered to calculate holding force



a b

Figure II-10: a. Magnetic holding force on each MPM in x-axis direction
b. Magnetic holding force on each MPM in y-axis direction

For this calculation, all the MPMs are placed in the lower-left positions ($-x_{MPM}$; $-y_{MPM}$) (Figure II-5). It can be observed that the distributions of the magnetic holding forces along the x and y axes are identical but transposed by 90°. The average magnetic holding force exerted by the FPMs on the MPMs is -0.62 ± 0.52 mN along both axes. The magnetic forces exerted on the MPMs placed at the array boundaries are strongly different compared to the magnetic forces exerted on MPMs of actuators placed at the center of the array. The elementary actuators at the center are indeed well magnetically balanced because there are as many elementary actuators on their left and on their right. For the elementary actuators placed at the boundaries of the array, there is a magnetic force deficit due to the lack of elementary actuators at one side.

II.2.2.2. Magnetic interaction force

In this section, the magnetic interaction forces between the MPMs are only considered and studied (array configuration shown in Figure II-11). These types of magnetic forces are considered as interaction forces which are caused by the assembly of several elementary actuators. The array is composed of a matrix assembly of 25 elementary actuators. In this

configuration, there are magnetic interactions between the MPMs that can disturb the array homogenous behaviour. In order to qualify these interactions, the magnetic interaction forces along the x- and y-axes exerted on each MPM by the other ones have then been computed and are presented in Figure II-12.

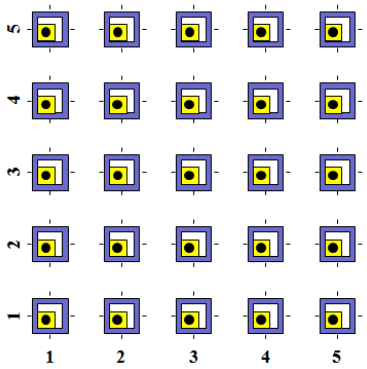


Figure II-11: Array configuration considered to calculate interaction force

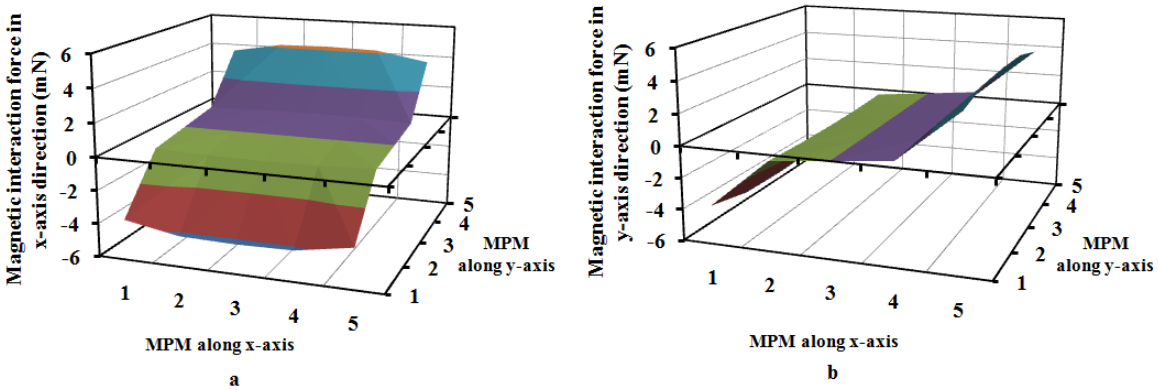


Figure II-12: a. Magnetic interaction force on each MPM in x-axis direction
c. Magnetic interaction force on each MPM in y-axis direction

As the magnetic force exerted by the FPMs, it can be observed that the distributions of the magnetic interaction forces along the x- and y-axis are identical but transposed by 90° due to the symmetrical MPMs positions in the array. The average value of the magnetic interaction forces is 0.00 ± 2.57 mN along both axes. The average value is null because of the symmetrical architecture of the array. The magnetic interaction forces exerted on the MPMs placed at the center of the array are small (approximate to 0 mN) because these MPMs are magnetically balanced. For the MPMs placed at the boundaries of the array, there is a magnetic force deficit due to the lack of MPMs at one side. They are then not balanced magnetically. For this reason, the magnetic interaction forces for the MPMs placed at the boundaries represent about 4 mN.

II.2.2.3. Magnetic balance force

In the two previous sections, it has been presented that the magnetic holding forces and the interaction forces are not identical for all the elementary actuators of the array. The MPMs of the elementary actuators placed at the boundaries of the array are indeed not magnetically balanced. In order to balance these magnetic forces, three rows of AFPMs in matrix form are placed around which has been presented previously in Figure II-4. The magnetic forces generated by the AFPMs are then called magnetic balance forces in this study. In this section, the magnetic balance forces generated by the AFPMs are only considered (array configuration shown in Figure II-13) and presented (Figure II-14).

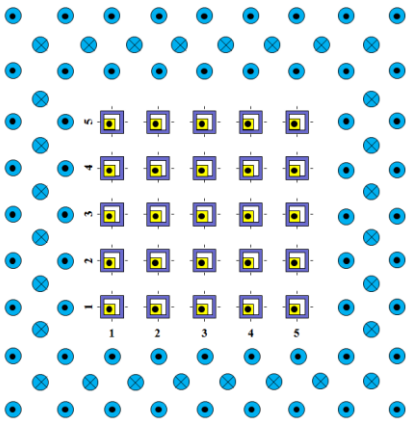


Figure II-13: Array configuration considered to calculate the magnetic balance force

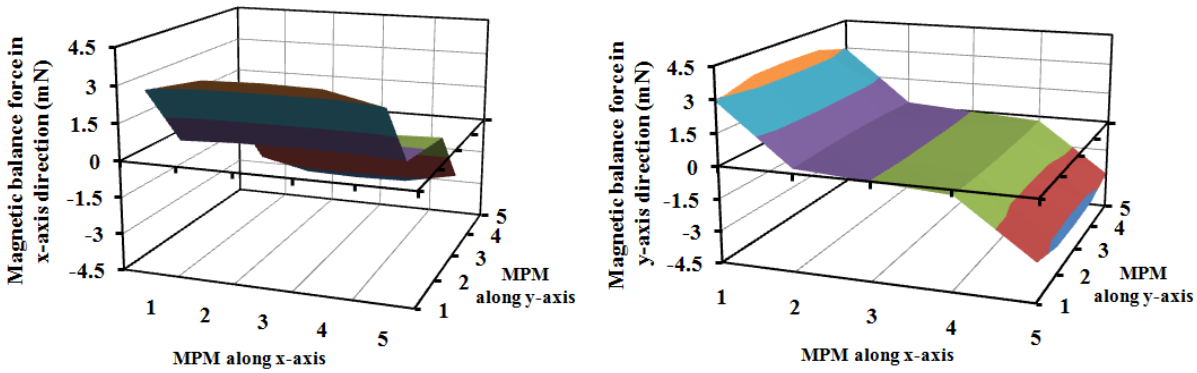


Figure II-14: a. Magnetic balance force on each MPM in x-axis direction
b. Magnetic balance force on each MPM in y-axis direction

The Figure II-14 represents the magnetic balance forces generated by the AFPMs and exerted on all the MPMs along x- and y- axes. As for the holding and the interaction forces, the distributions of the magnetic balance forces are identical with a transposition of 90°. The average value of the magnetic balance forces is -0.04 ± 2.05 mN along both axes. It has been

observed that the magnetic balance force decreases from the edge to the center which just compensates and balances the magnetic holding forces and the interaction forces.

II.2.2.4. Total magnetic force

In this section, the total magnetic forces exerted on all the MPMs along x- and y-axes have been computed. The total magnetic forces consist of the sum of the magnetic holding forces, the interaction forces and the balance forces exerted on the MPMs by the interactions with the FPMs, MPMs and AFPMs respectively. In order to present the contributions of the magnetic balance forces generated from the AFPMs, one magnetic force configuration of the array without considering the balance forces have also been presented for a comparison. The Figure II-15 presents the total magnetic holding forces exerted on the 25 MPMs in the x- and y-axes without and with considering the magnetic balance forces respectively.

The average magnetic forces value without considering the magnetic balance forces is -0.62 ± 2.05 mN (Figure II-15-a and b). Without AFPMs, the elementary actuators placed at the center of the array are well magnetically balanced by the elementary actuators around. However, the elementary actuators placed at the boundaries of the array are not magnetically balanced due to the lack of elementary actuators on one side or another. The high magnetic forces variation value of 2.05 mN is then observed. But when the magnetic balance forces are considered (Figure II-15-c and d), the average total magnetic forces value exerted on all MPMs is -0.57 ± 0.06 mN. The elementary actuators placed at the boundaries of the array are better magnetically balanced. A more homogeneous total magnetic forces over the array has then been achieved. The AFPMs enable then to balance the elementary actuators of the array. A prototype of array based on this design (Figure II-4) has been manufactured during the former thesis [PETI 2009]. This prototype has been experimentally tested and its performances will be presented in the next chapter.

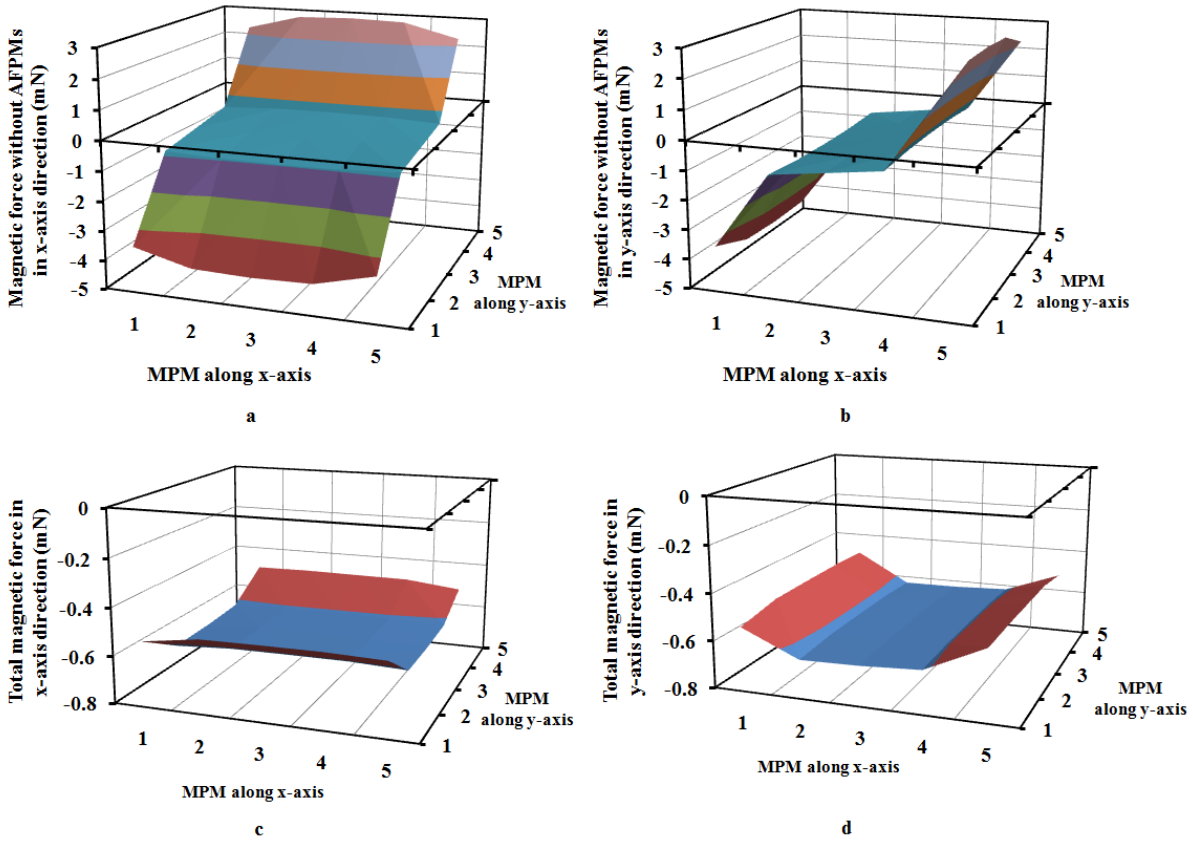


Fig II-15: a. Magnetic force without considering balance force in x-axis direction
b. Magnetic force without considering balance force in y-axis direction
c. Total magnetic holding force on each MPM in x-axis direction
d. Total magnetic holding force on each MPM in y-axis direction

In conclusion, the development of the RADIA static model enables to calculate the static magnetic forces exerted on all the MPMs including the magnetic forces from the FPMs, the MPMs and the AFPMs. A homogeneous behavior of the array has been achieved. In the next section, a static model based on MATLAB software is presented. The main advantage of this analytical model developed in MATLAB software is the possibility to integrate this model in another MATLAB programs which can be used to improve the array design.

II.2.3. Analytical modeling with MATLAB

The static model of the actuators array developed in MATLAB software is presented in this section. A static model of the elementary actuator is firstly presented to show the basic principle of magnetic calculation in MATLAB. Then, a static model of the actuators array is described.

II.2.3.1. Modelling of the elementary actuator

In this section, the static modelling of the elementary actuator is presented. This model has been used to characterize the elementary actuator performances. In this section, the magnetic and electromagnetic force models and an important static parameter called "Self Returning Zone" (SRZ) are presented.

II.2.3.1.1. Magnetic flux density

To compute the magnetic and electromagnetic forces, a magnetic flux density model has to be developed. An analytical model able to calculate the magnetic flux density generated by the PMs has then been developed. This model is based on two assumptions. Firstly, the PMs geometries are considered perfect and in free space. Secondly, the PMs magnetizations are considered uniform and oriented along z-axis. In the model, each PM is reduced to a distribution of equivalent magnetic charge [FURL 2001]. The determination of the magnetic flux density expressions have been realized considering the PM presented in Figure II-16. The dimensions of the PM are $(x_2 - x_1)$ $(y_2 - y_1)$ and $(z_2 - z_1)$ respectively along the three directions (x, y and z). The origin of the coordinate system (0; 0; 0) is located at the center of the PM, its north and south poles are placed on the surfaces (+z) and (-z) respectively. The expressions of the magnetic flux density generated by a PM are then given by Equation II-1 [FURL 2001]. The computation of the external magnetic flux density components B (generated by the PM) at the any point (x; y; z) located outside of the PM is realized using these equations.

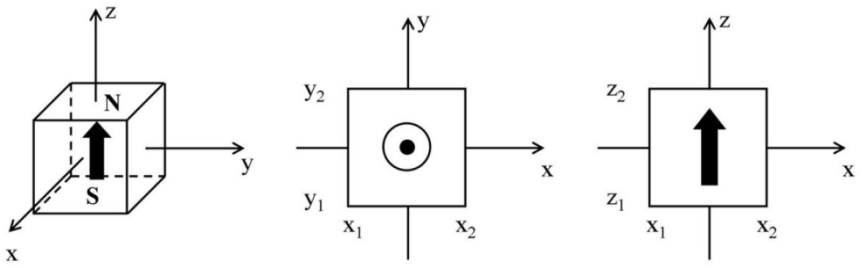


Fig II-16: PM and coordinate for the modeling of magnetic flux density

$$B_x(x,y,z) = \frac{\mu_0 M_S}{4\pi}\sum_{k=1}^{2}\sum_{m=1}^{2}(-1)^{k+m}\ln\left(\frac{(y-y_1)+\left((x-x_m)^2+(y-y_1)^2+(z-z_k)^2\right)^{1/2}}{(y-y_2)+\left((x-x_m)^2+(y-y_2)^2+(z-z_k)^2\right)^{1/2}}\right)$$

$$B_y(x,y,z) = \frac{\mu_0 M_S}{4\pi}\sum_{k=1}^{2}\sum_{m=1}^{2}(-1)^{k+m}\ln\left(\frac{(x-x_1)+\left((x-x_1)^2+(y-y_m)^2+(z-z_k)^2\right)^{1/2}}{(x-x_2)+\left((x-x_2)^2+(y-y_m)^2+(z-z_k)^2\right)^{1/2}}\right) \quad \text{(II-1)}$$

$$B_z(x,y,z) = \frac{\mu_0 M_S}{4\pi}\sum_{k=1}^{2}\sum_{n=1}^{2}\sum_{m=1}^{2}(-1)^{k+n+m}\times$$

$$\tan^{-1}\left(\frac{(x-x_n)(y-y_m)}{(z-z_k)(y-y_2)\left((x-x_n)^2+(y-y_m)^2+(z-z_k)^2\right)^{1/2}}\right)$$

Where,

B_x, B_y, B_z : Magnetic flux density components (T) along x-, y- and z-axis respectively,

μ_0 : Magnetic permeability of air ($4\pi \times 10^{-7}$) ($N \cdot A^{-2}$),

M_S : Magnetization of the permanent magnet ($A.m^{-1}$),

(x; y; z) : Coordinates of the computing point (m).

II.2.3.1.2. Magnetic holding force

In this section, the magnetic interaction force between two PMs is modeled. In order to determine the expression of this magnetic force, the PMs A and B presented in Figure II-17 are considered. The expression of the magnetic force generated by PM A and exerted on the PM B is given by Equation II-2 [FURL 2001]. This force model is based on the magnetic flux density model presented in the previous section.

$$F_{Magnetic} = \iint_S \sigma_m B_{ext}\, ds \quad \text{(II-2)}$$

Where,

$F_{magnetic}$: Magnetic force (N),

σ_m : Surface charge density ($A.m^{-1}$),

B_{ext} : Magnetic flux density (T) generated by PM A.

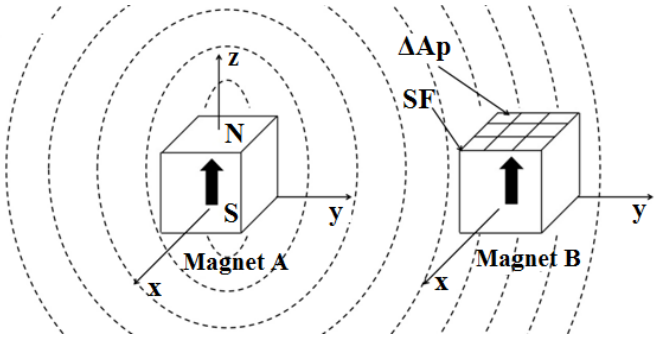


Fig II-17: Magnets and coordinate system illustrated for magnetic holding force calculation

In most of cases, as Furlani has explained in his book, the Equation II-2 cannot be used for an analytical calculation. A discretization of the pole surfaces (SF) of PM B into sub-surfaces ΔA_p (where p is corresponding to the number of surface elements) is needed (Figure II-17). With this discretization of the PM Pole surface, the magnetic flux density (B_{ext}) is computed for each sub-surface with Equation II-1. The magnetic force is then obtained with Equation II-3.

$$F_{Magnetic} = \sum_{p} \sigma_m(x_p) B_{ext}(x_p) \Delta A_p \qquad \text{(II-3)}$$

The Figure II-18 illustrates 3 examples of PM pole surface discretizations with different p values (1, 9 and 25). For a discretization of the pole surface with value p, the surface of the magnet pole surface is divided into N × N sub-surfaces in rectangular ($p = N^2$). With a high N value, the calculation for the magnetic holding force is then more precise but more time-consuming [PETI 2009].

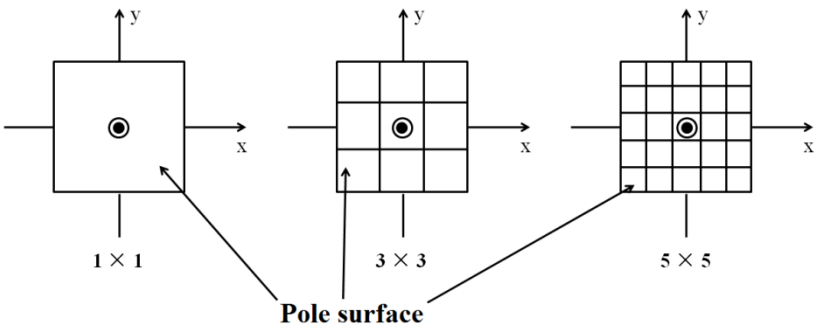


Fig II-18: Different discretization value illustrated on the pole surface

Using this model, the magnetic holding force exerted on the MPM for different positions between two discrete positions is presented in Figure II-19. The force components along the displacement direction (Figure II-19-a) and orthogonal to the displacement direction (Figure II-19-b) are presented. During the former thesis [PETI 2009], a study on the value of N has been realized and according to this study, the value of N has been fixed at 10. With this value, the discretization error is indeed negligible. However, a study which aims to verify the influence of value N on the magnetic forces value computation (for the actuators array) generated by the MATLAB model will be presented at the end of this chapter.

It can be observed in Figure II-19-a that the magnetic holding force value is symmetrical to the reference frame origin (0; 0) along the MPM displacement direction. This phenomenon is due to the symmetrical geometry design of the elementary actuator. The maximum amplitude of the holding force value is ±0.6 mN and is obtained when the MPM is located in stable positions (±0.1 mm). When the MPM is located in the middle position of the square cavity (0 mm), the magnetic holding force is 0 mN. At this position, the distance between the MPM and the FPMs located at its left and at its right are indeed identical. Moreover, the shape of the holding force follows a linear course due to the small stroke of the MPM when compared to the distance between the cavity and square FPMs. In Figure II-16-b, it can be observed that during a switch of the MPM between two stable positions, the variation in the magnetic force perpendicular to the displacement direction can be neglected.

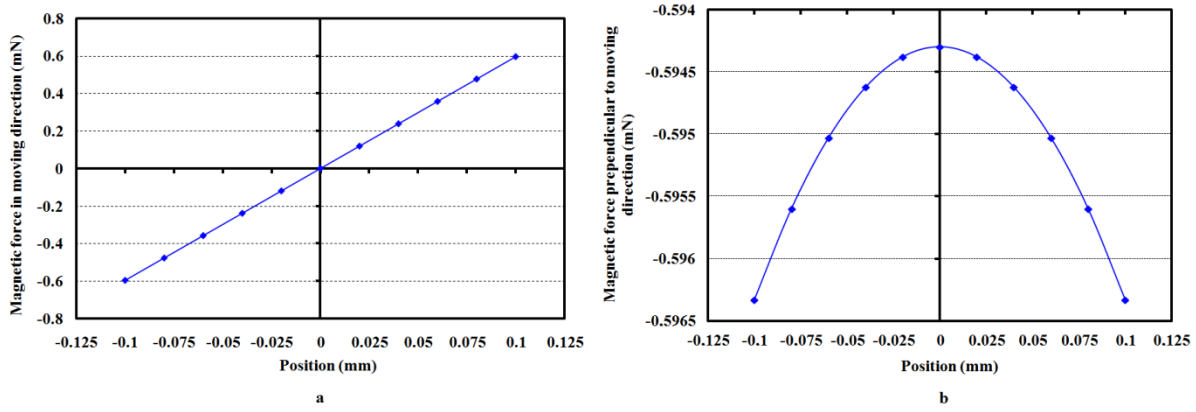


Fig II-19: a. Magnetic force in moving direction
b. Magnetic force perpendicular to moving direction

II.2.3.1.3. Electromagnetic force modelling

In this section, the electromagnetic force (Lorentz force) used for the switching function and exerted on the MPM to switch it between the stable positions is modelled. The expression of this force is given by Equation II-4.

$$F_{Electromagnetic} = I\int_{Wire} dl \times B_{ext} \qquad \text{(II-4)}$$

Where:

I : Driving current sent in the wires below the MPM,

B_{ext} : Magnetic flux density generated by the MPM around the considered wire.

For each MPM, two components (horizontal along x or y-axis and vertical along z-axis) of electromagnetic force exerted on each MPM have been calculated and plotted in Figure II-20. Without driving current (0A), the electromagnetic force is null and when a current passes through the wire, an electromagnetic Lorentz force is generated. When the MPM is misaligned with the wire (Figure II-21), there is a horizontal component along the x or y-axis of the magnetic flux density from the MPM on the wire. This horizontal component generates a vertical component of the electromagnetic force.

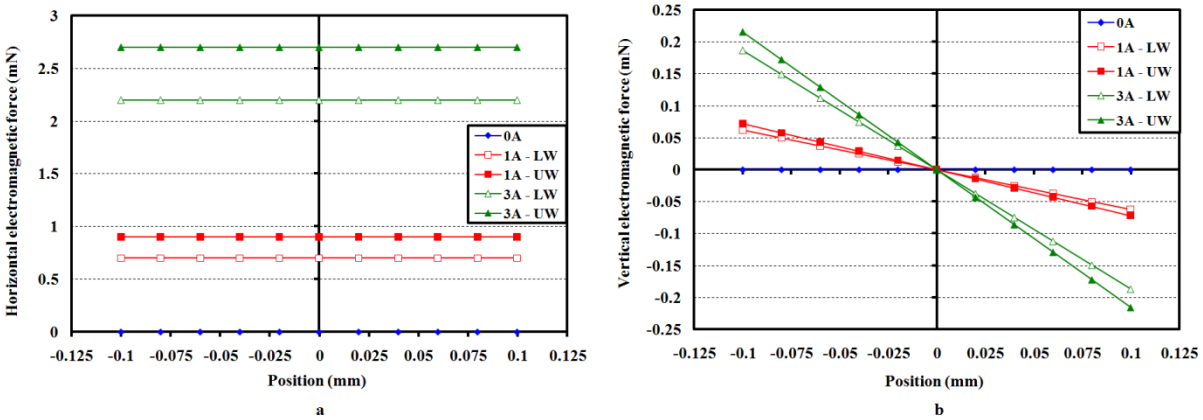


Fig II-20: a. Electromagnetic force component in horizontal direction
b. Electromagnetic force component in vertical direction

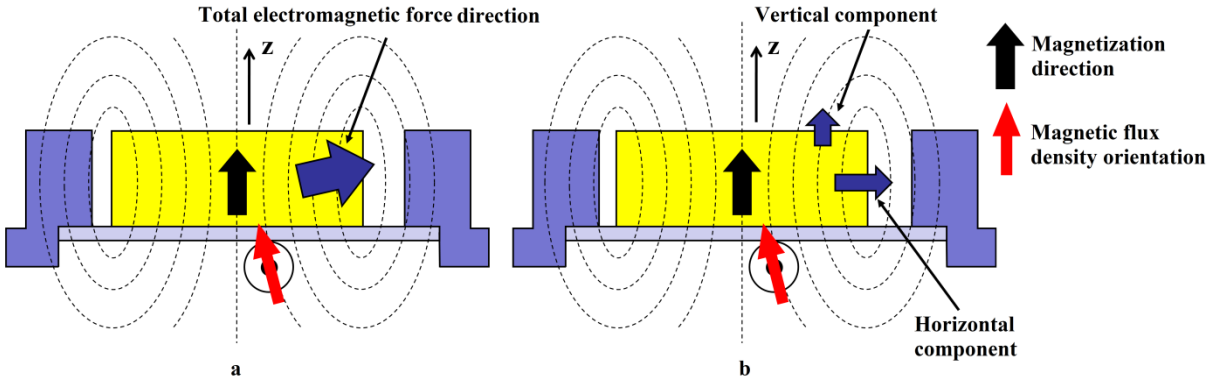


Fig II-21: a. Illustration of the total electromagnetic force
b. Illustration of the two components of the electromagnetic force

It can be observed in Figure II-20-a that the electromagnetic force values are constant in the horizontal direction. The horizontal component of the electromagnetic force doesn't change with the MPM position between two stable positions. However, the vertical components of the electromagnetic forces are not constant. They changes with the MPM position between two stable positions (Figure II-20-b). This phenomenon is due to the relative position change between the MPM and the wires below.

Moreover, it can also be observed that the electromagnetic force generated by the UW is always bigger than the one generated by the LW. This result is due to the longer distance between the LW and the MPM than between the UW and the MPM. The MPM introduces a higher magnetic flux density (in z direction) around the UW than LW. As a result, with the same current value, a higher electromagnetic force is generated by the UW than the LW. The horizontal and vertical components of the electromagnetic force are indicated in Table II-4 for 1A current value.

Electromagnetic force with 1A	UW	LW
Horizontal	0.90 mN	0.73 mN
Vertical (in stable position)	0.07 mN	0.06 mN

Table II-4: Electromagnetic force values for 1A driving current

II.2.3.1.4. Self-returning zone calculation

In this section, the Self-Returning Zone (*SRZ*) of the elementary digital actuator is presented and calculated by using the MATLAB model. The *SRZ* is an important parameter for the digital actuator because it characterizes its digital behavior. It corresponds to the maximum distance from the stable position where the MPM could return to the nearest discrete position without energy consumption. This parameter has been given in [PETI 2009] and helps to

evaluate the holding function of the digital actuator. The *SRZ* represents the robustness of the actuator (ability of maintaining the stable positions) to external disturbance: if the MPM displacement generated by the disturbance is less than the length of *SRZ*, the MPM will return to its stable positions; otherwise the MPM cannot return. The Figure II-22 provides a representation of the actuator behavior and of the *SRZ* concept. The circle and the inclined zone represent the mobile part of the actuator at an Intermediate Zone (*IZ*) and two *SRZ* respectively. When the MPM is placed in the square cavity, it is subjected to the magnetic holding force and the adhesion forces between the MPM and the cavity. In the *SRZ*, the magnetic holding force is higher than the adhesion force. In the *IZ*, the magnetic holding force is less than the friction force. If an external disturbance moves the MPM to the *SRZ*, the MPM can return to its stable position thanks to the magnetic holding force without external energy consumption. On the contrary, if the external disturbance moves the MPM to the *IZ*, the MPM will stay in the *IZ*.

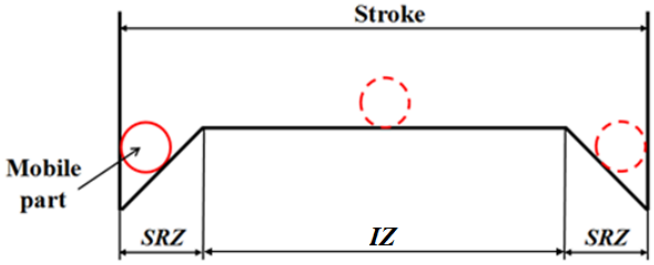


Figure II-22: Self-returning zone of the elementary actuator

In order to calculate the length of *SRZ*, force analysis has been done on the MPM. When the MPM is placed in the square cavity, it is subjected to the magnetic holding force ($F_{holding}$) (presented in Figure II-19) and total adhesion force ($F_{adhesion}$). The total adhesion force consists of two components which are the horizontal adhesion force ($F_{horizontal}$) (between the MPM and the glass layer) and the lateral adhesion force ($F_{lateral}$) (between the MPM and the square cavity). Their expressions are given in Equation II-5. In the former thesis [PETI 2009], the horizontal coefficient of adhesion ($\mu_{horizontal}$) and the lateral coefficient of adhesion ($\mu_{vertical}$) have been experimentally determined and are 0.41 and 0.30 respectively. As the magnet holding force value varies with the MPM position change in the square cavity, there are then two symmetrical equilibrium positions for the MPM which locate on the boundary of the *SRZ* (positions A and B in Figure II-23-a). At these two positions, the magnetic holding force exerted on the MPM equals to the total adhesion force between the MPM and the square cavity. To facilitate the understanding, half of the stroke is used to illustrate the relationship between the holding force and the adhesion force (Figure II-23-b). In the *SRZ*, the magnetic

holding force is higher than the adhesion force. In the *IZ*, the magnetic holding force is equal to the adhesion force. The adhesion force expression is shown in Equation II-5.

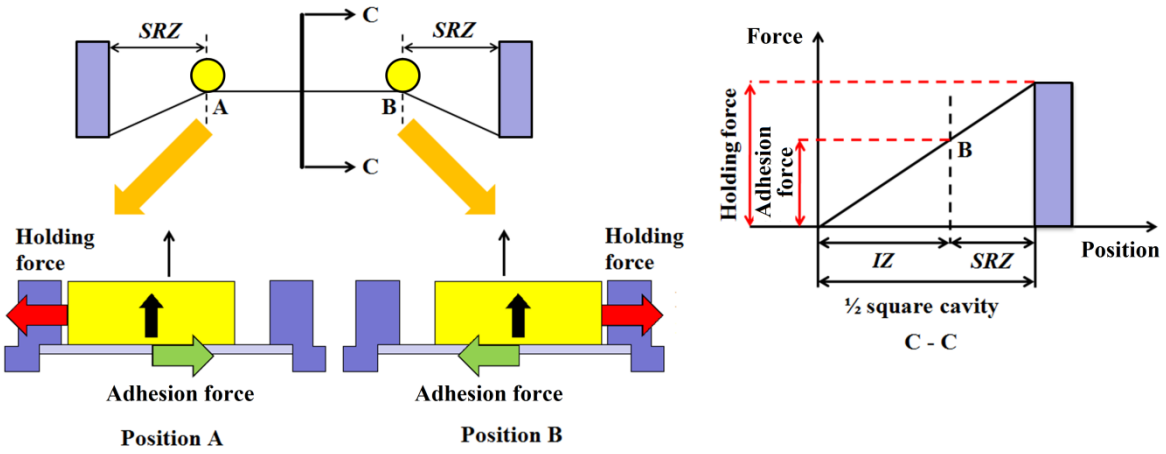


Fig II-23: a. Two equilibrium positions (A, B) of the actuator
b. Relationship between the holding force and the *SRZ*

$$\begin{aligned} F_{adhesion} &= F_{horizontal} + F_{lateral} \\ F_{horizontal} &= \mu_{horizontal} \times m_{MPM} \times g \\ F_{lateral} &= \mu_{lateral} \times F_{holding} \end{aligned} \tag{II-5}$$

Where,

m_{MPM} : MPM mass (g),

g : Gravity acceleration (9.81 m/s^2).

As presented in Figure II-19-a, a linear relationship can be considered between the holding force and the MPM position in the square cavity. With this relationship, the *SRZ* length is computed with Equation II-6.

$$SRZ = \frac{L}{2} \times \left(1 - \frac{F_{holding}}{F_{adhesion}}\right) \tag{II-6}$$

Where,

L : Stroke of the MPM (0.2 mm).

For the presented elementary actuator, the theoretical length of *SRZ* is 30.4 µm. The *SRZ* of the presented digital actuator represents 2 × 15.2% of its stroke (200 µm).

In this section, the elementary actuator performance has been characterized by the MATLAB model. In order to characterize the performance of the array, model of the actuators array has been developed and is presented in the following section.

II.2.3.2. Modelling of the actuators array

In this section, a static model of the actuators array has been developed on MATLAB. The model has been achieved by the integration of the elementary actuator model. The objective of this model is to verify the function homogeneity of the array e.g. holding force. During the modelling of the actuators array, only the magnetic forces have been modelled. The electromagnetic forces have not been taken into account. The electromagnetic forces have only been modelled for the elementary actuator and the electromagnetic disturbances between the elementary actuators have been characterized in the former thesis [PETI 2009]. It showed that when one MPM is switched, the electromagnetic force generated on one of its neighbours is not enough to switch the neighbour MPMs. As a result, the model of the array has been also simplified.

In order to calculate the magnetic forces exerted on each MPM in the array, Equations II-1 are used to calculate the external magnetic flux density (B_{ext}) generated by the others PMs on the pole surfaces of the considered MPM. In our situation, there are lots of PMs (145 PMs in total). Consequently, the calculation of the magnetic flux density for all the MPMs in the array becomes complex and very long. A particular way to analytically calculate the magnetic flux density around each MPM in the array has been proposed.

The magnetic flux density calculation method is illustrated in Figure II-24. This method of calculation consists of 3 steps. At the first step, the total magnetic flux density of the overall array ($B_{Overall}$) has been calculated by summing the magnetic flux density generated by all the MPMs (B_{MPMs}), the FPMs (B_{FPMs}) and the three rows of AFPMs (B_{add1}, B_{add2} and B_{add3}), respectively (Equation II-7).

At the second step (Figure II-24), the external magnetic flux density (B_{ext}) around the considered MPM is calculated by subtracting the contribution of the considered B_{MPM} to the total flux density $B_{Overall}$ (Equation II-8). The total magnetic forces exerted on the considered MPM is then obtained and considered as B_{ext} in Equation II-3. The presented method enables to reduce the magnetic forces calculation time for the array. It enables to give the expressions of the B_{ext} of the considered MPM just by subtracting the magnetic flux density generated by

itself. As a result, there is no need to recalculate the B_{ext} for each MPM by summation of magnetic flux density generated from the other 144 PMs every time. The calculation time is then highly reduced. A comparison of calculation time length has been done between the common method (calculate the B_{ext} for each MPM every time) and the proposed method, a gain time of (15 %) have been achieved for one calculation (obtained with a computer equipped with an Inter i3 CPU (3.3 GHz) and 6 Go RAM memory). This time saving feature of programming is very important because this program has been integrated with an optimization algorithm which requests for a large number of calculations.

$$B_{Overall} = B_{MPMs} + B_{FPMs} + B_{add1} + B_{add2} + B_{add3} \tag{II-7}$$

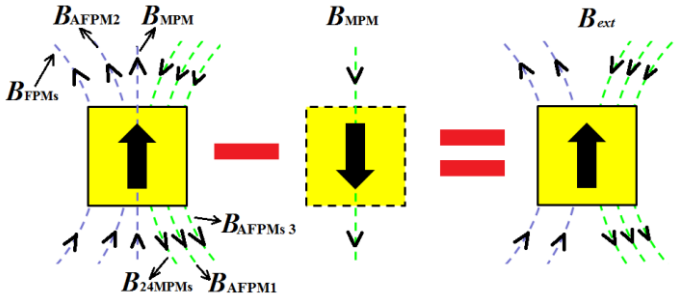


Fig II-24: Calculation of the total external magnetic flux density

$$B_{ext} = B_{Overall} - B_{MPM} \tag{II-8}$$

In this section, a static analytical model has been developed in MATLAB. This model enables to analytically calculate the magnetic forces exerted on each MPM. Moreover, it integrates also the computation of the *SRZ* value using Equation II-6. Figure II-25 represents a 2D quick view of the array which is also achieved via the MATLAB model. This 2D view enables to visualize the array geometry e.g. the dimensions of the PMs, the distances between the PMs, the PMs Magnetization directions, etc. The 2D quickly view function has also been greatly used in chapter IV for a comparison among optimized arrays.

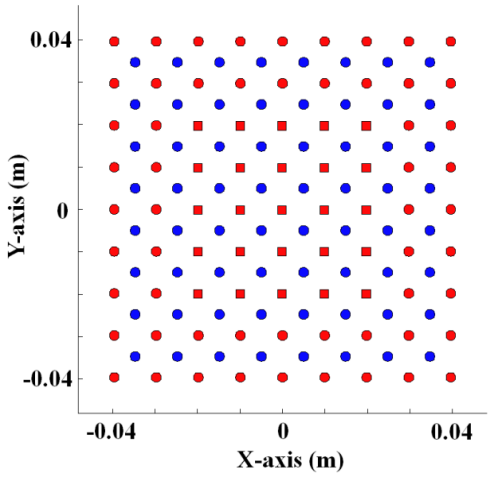


Fig II-25: 2D quick view of the prototype array

II.2.4. Comparison of the two models

In this section, a comparison between the magnetic forces using the two models based on RADIA and MATLAB has been realized in order to verify that the results are correct. The magnetic forces exerted on the 25 MPMs by all the PMs of the array have been computed. For the comparison, all the MPMs have been placed in the lower left stable position ($-x_{MPM}$; $-y_{MPM}$). The magnetic forces have been computed using RADIA and MATLAB with different values of the discretization parameter N. The Table II-5 gives the absolute value of the average total magnetic force exerted on the MPMs by the two models.

Holding force (mN) with RADIA model	0.574 mN		
Holding force (mN) with MATLAB model	**N** = 1	**N** = 3	**N** = 5
	0.525 mN	0.566 mN	0.573 mN
Relative error	8.50%	1.32%	0.21%
MATLAB Computation time	2 min	6 min	10 min

Table II-5: Comparison of the two models

It has been observed that the calculated magnetic force value obtained by MATLAB is more precise when the value of N increases. When the value of the discretization is set to 5, the error between the two models is small enough to be neglected. However, the computation time increases when the value of N increases which is visible in Table II-5. The presented computation times have been obtained with a computer equipped with an Inter i3 CPU (3.3 GHz) and 6 Go RAM memory. It has been previously presented that for the optimization

study which will be presented in chapter IV, the reduced of calculation time is very important due to the massive calculation in optimization algorithm. The increase of N value will greatly increase the calculation times then the program running time. This study of the influence of N value to the calculation time then enables us to choose the proper N value during the optimization of the array.

The comparison between the two models has shown that the proposed model developed on MATLAB gives coherent results as compared with the model developed on RADIA. The correctness of the MATLAB model has then been proved. The influence of the parameter N value has also been analysed from the comparison which enables us to make a compromise in choosing the suitable N value during the optimization in chapter IV with the objective of saving calculation time.

II.3. Conclusion

In this chapter, the principle of a four stable positions elementary digital actuator has been firstly presented. Based on this principle, an actuators array which consists of 25 elementary actuators has been presented. The potential application of the actuators array has also been presented which enables to realize a planar conveyance of a thin plate with the contributions of all the elementary actuators in the array.

Secondly, static models of the elementary actuator and of the actuators array have been presented. Two softwares have been used to develop these models RADIA and MATLAB. This model enables to calculate the magnetic forces exerted on each MPM in the array by all the PMs. The main objective of this model is to characterize the magnetic force behaviour overall the array. It also helps to design the array and verify the correctness of the model developed on MATLAB. The second model enables also to calculate the magnetic forces exerted on all the MPMs in the array. During the modelling, a particular method of calculating the magnetic flux density over each MPM has been proposed which enables to reduce the calculation time. Other parameters can also be achieved by this model e.g. *SRZ* value, quick 2D view, etc. The main objective of the MATLAB model is to be integrated with an optimization program presented in chapter IV. An optimization of the array is then possible.

At the end, a comparison of the models output results between the two models has been presented. This comparison has shown that the proposed MATLAB model gives similar

results than the RADIA model. The influence of the discretization parameter N to the magnetic force computation has been analyzed. It has been observed that when the N parameter value increases, the calculation precision increases but the calculation time also. This effect helps us to make a compromise between time saving and calculation precision in choosing the N value which is considered in the optimization algorithm (presented in chapter IV).

In the next chapter, an experimental prototype based on the presented architecture of the array will be presented. Experimental measurements on the prototype array have been carried out to characterize the array performances. The influences of the manufacturing errors on the magnetic forces have been computed using the MATLAB model developed in this chapter. At the end, several experiments focusing on the planar conveyance application have been done to characterize the dynamic performance of array.

Chapter 3: Experimental realization and characterization of the actuators array

In the previous chapter, the actuation principle, the application principle and finally the modeling of the digital actuators array have been presented. In order to verify the functionality of the array, experimental characterizations of the array behavior are needed. In this chapter, a prototype has been developed in order to validate the array functions experimentally and also its planar conveyance application.

This chapter is divided into three sections. To ensure the homogeneity behavior of the array, the prototype fabrication precision is important. Consequently, the dimensions measurement of the prototype array and the influence of the manufacturing errors on its behavior are firstly presented. Secondly, the experimental setups used are presented. Upon using these setups, several experiments in different configurations of the prototype array have been done and the results are presented and analyzed. Finally, a conclusion of all the experimental results is done.

III.1. Presentation of the prototype

In this section, all the components of the prototype array are presented. The Figure III-1 represents a schematic view of all the prototype array components. The prototype array consists of a thin glass plate, a mechanical base support, FPMs and MPMs a thin glass layer and a back support with bottom PMs. During the experiments, the back support with bottom FPMs has been placed below the base support. These components are added because the MPMs may not all contact with the plate due to the fabrication errors of the MPMs and the flatness of the plate. These bottom PMs (dimensions: Ø2.26 mm × 2 mm, magnetizations: 1.45T) are used to generate a vertical magnetic force on the MPMs which will levitate the MPMs and insure the mechanical contact between the MPMs and the thin glass plate (Figure III-1).

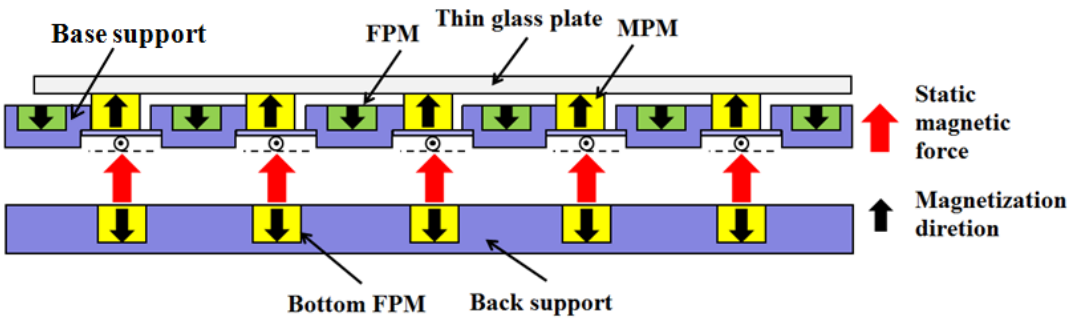


Fig III-1: Schematic view of the array components

The Figure III-2 represents all the experimental components of the array. The biggest parts of the experimental prototype array are the base support (Figure III-2a) and the back support (Figure III-2c). They are made of aluminium and have been manufactured by conventional machining. A conventional milling machine with a milling cutter of 0.8 mm diameter has been used for the fabrication. The aluminium material has been selected because of its non-ferromagnetic property which does not affect the global magnetic flux density generated by the PMs. The FPMs, MPMs, the double side PCB (Figure III-2b) and the thin glass layer, used to avoid electrical contact between the PCB and the MPMs, have been assembled with the base support. In the next section, a geometrical study of the prototype array has then been done to evaluate the influence of the manufacturing errors on the prototype behaviour.

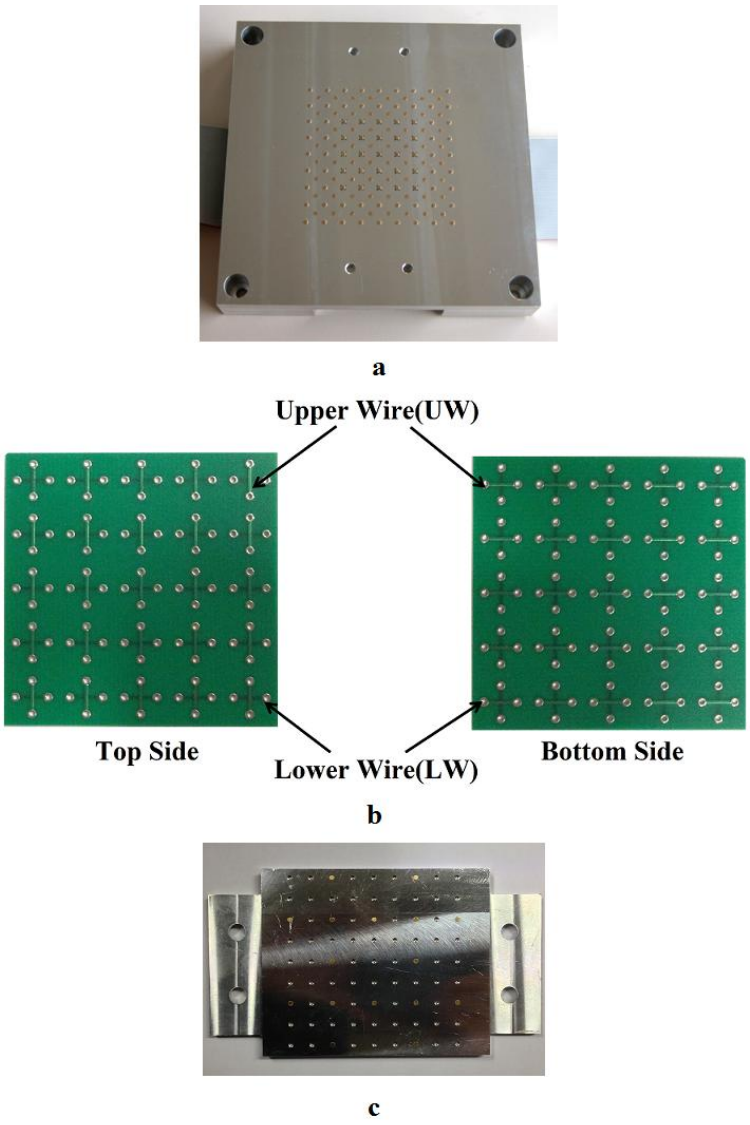


Fig III-2: Practical view of the prototype array components:
a. Base support b. PCB c. Back support

III.2. Geometrical study of the prototype array

This geometrical study of the prototype array consists in two parts. The first one is the measurement of dimensional manufacturing errors of the 25 square cavities. The second one is the measurement of dimensional manufacturing errors of the MPMs. These two measurements are important because they determine the actual strokes of the elementary actuators. Identical strokes are necessary to ensure a homogeneous contribution of each elementary actuator for the conveyance application.

III.2.1. Measurement tools

For the two different measurements, two different tools have been used. Firstly, the measurements of the 25 square cavities in two directions (x- and y-axis) have been performed with a white light interferometer machine ZYGO™ (New view 200) at the Roberval laboratory (Figure III-3).



Fig III-3: Real view of ZYGO™ 200 interferometer microscope

This device is used because of its high precision (its characteristics are presented in Table III-1). The utilization of ZYGO™ can easily realize a high precision contactless measurement of the square cavities.

Vertical Resolution (nm)	Spatial Resolution (µm)	Vertical Scan travel (µm)	Observable surface	Objective lens	Scan Time (sec)	Observable parameters
0.1	0.44 to 8.8	100	140 × 110 µm² to 2.82 × 2.11 mm²	×2.5, ×10 And × 50	55 (Max.)	Macro/micro Roughness, waviness

Table III-1: Typical characteristics of ZYGO™ 200 interferometer microscope

For the measurement of the MPMs dimensions in three direction x-, y- and z-axis, due to its tiny size and magnetic property, a digital micrometer (precision: 0.001 mm) has been used.

III.2.2. Measurement of the dimension and position errors

The measurement of the 25 square cavities dimensions (theoretic value: 2200 µm) has been firstly done. For each square cavity, three measurements have been done for both x- and y-

axes (Figure III-4). An average value has been calculated for the 25 square cavities. The manufacturing error of the 25 square cavities varies from +10 µm to +140 µm and from +12 µm to +118 µm for x and y axes respectively.

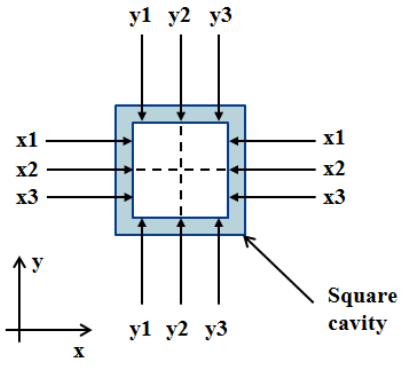


Fig III-4: Measurement of the square cavity

A schematic illustration of the square cavities which presents the spread of the manufacturing errors is given in Figure III-5. It has been observed that the manufacturing errors of the square cavities are irregular and spread over the entire array. However, there are less manufacturing errors along the x-axis direction compared to the y-axis direction. These manufacturing errors of the square cavities all result from the conventional fabrication methods. In the perspectives, these errors can be greatly decreased by using micro-fabrication techniques.

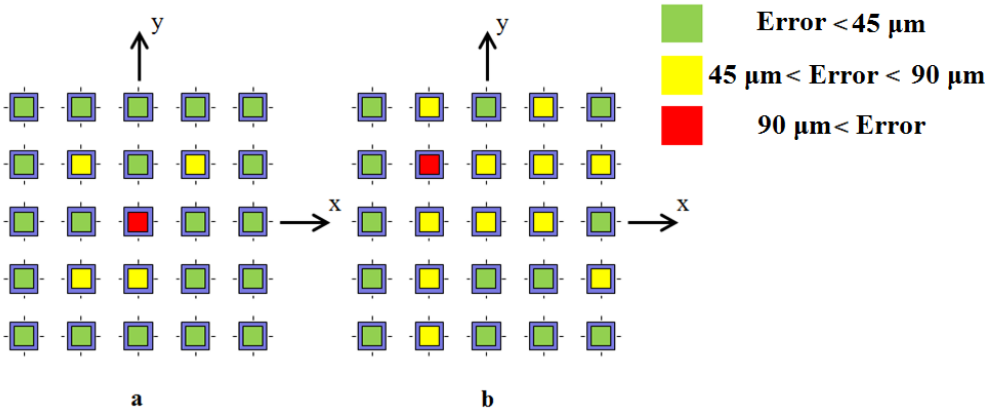


Fig III-5: a. Manufacturing errors along x-axis axis,
b. Manufacturing errors along y-axis axis

The manufacturing errors of a square cavity will affect the corresponding MPM position in the square cavity as illustrated in Figure III-6. The actual MPMs positions have been changed half of the manufacturing error values (5 - 70µm and 6 – 59 µm along x and y axes respectively) compared to the perfect situation (no manufacturing errors) when they are

placed in the square cavities. In the next section of this chapter, the influence of this error on the magnetic behaviour of the array has been considered. This error is then defined as "ERROR I".

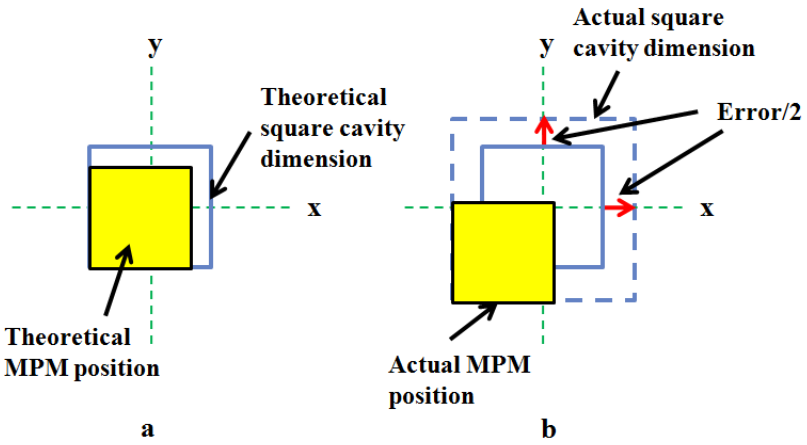


Fig III-6: a. Theoretical MPM position, b. Actual MPM position

Secondly, the dimensions of the 25 MPMs have been measured along the three axes. Similarly with the measurement of the square cavities, each MPM has been measured three times along one axis and the average value has been calculated. This maximum manufacturing error of the MPM along the three axes is defined as "ERROR II" (Figure III-7) and varies from -16 µm to 8 µm. The PM manufacturer has announced the maximum manufacturing errors of the MPMs are within ±50 µm. The measured ERROR II values then confirm the manufacturing errors announced by the fabricant.

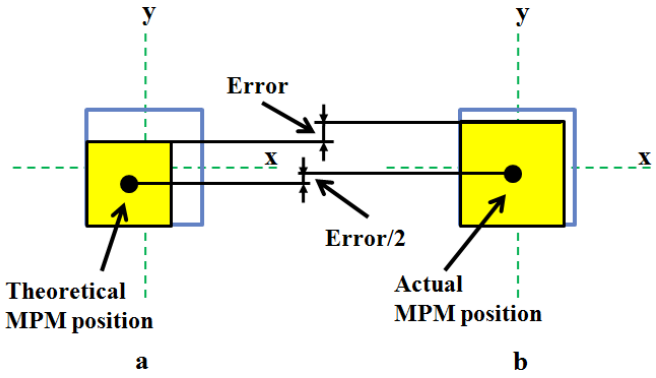


Fig III-7: a. Theoretical MPM position, b. Actual MPM position

Error I results in change of the MPM positions in the array while Error II results in the change of both the MPM position and dimensions. Because of these manufacturing errors, the magnetic holding force exerted on each MPM is not perfectly homogenous. In order to

characterize the real magnetic force exerted on the MPM present in the prototype array, the influence of the two manufacturing errors on the static magnetic holding force has been studied.

III.2.3. Influence of the errors on magnetic holding force

The two measured errors have been taken into account in the RADIA model presented in Chapter II. In these calculations, the maximum and minimum influences of the manufacturing errors on the average magnetic holding force (0.621 mN) have been determined by considering the maximum and minimum error values respectively and are shown in Table III-2.

	Error I	Error II
Manufacturing Error value	+5 µm to +70 µm	-16 µm to +8 µm
Holding Force change	0.635 mN to 0.829 mN	0.592 mN to 0.634 mN
Relative Change	+2.4% to +33.5%	-4.7% to +2.1%

Table III-2: Influence of the fabrication errors on magnetic force

In the first calculation (first row of Table III-2), the manufacturing errors of the square cavities (Error I) are only considered. To calculate the corresponding influence, the manufacturing errors (minimum and maximum values) are only integrated to the square cavity placed at the center of the array. The other square cavities in the array are considered perfectly manufactured. When the Error I varies from 5 µm to 70 µm, its influence on the average magnetic holding force increases from 2.4% to 33.5% compared to the perfect situation. In addition to the MPM stroke variation, Error I increases the average magnetic holding force. Moreover, the unequal strokes of the MPMs induce inhomogeneous characteristics of the array e.g. different switching times. The collaboration switching of the MPMs is then degraded which will result in different contributions from each MPM to the plate during the switching. On the other hand, the high increase in magnetic holding force increases also the lateral adhesion force between the MPMs and the square cavities stops. To

switch, a higher driving force is then needed to overcome the sum of magnetic holding force and the friction force.

In the second calculation (second row of Table III-2), the manufacturing errors of the MPMs dimensions (Error II) are only considered. In consistent with the first calculation, the manufacturing errors of the MPMs are also integrated to the MPM placed in the center cavity. The other MPMs are considered perfect. When the Error II varies from -16 µm to 8 µm, the average magnetic holding force changes from -4.7% to +2.1% compared to the perfect array. The magnetic holding force errors calculated have been obtained while considering the maximum errors for all the 25 MPMs. To minimize the effect of this error, the MPMs have been selected between the available MPMs (several hundred) to match with each square cavity. This error is then not significant and can be neglected.

The influence of the manufacturing errors of the square cavities on the magnetic holding force is higher than the influence of the fabrication errors for the MPMs. Using the model of the array (presented in chapter II), a recommendation of the maximal acceptable manufacturing error of the square cavities can be provided. If the difference between the actual magnetic holding force and theoretical magnetic holding force (0.57 mN taken as reference: 100%) is needed to be less than 10%, the manufacturing error of the square cavity should be within 22 µm. Furthermore, if this difference value needs to be less than 20% or 30%, the fabrication errors of the cavity should be within 43 µm and 64 µm, respectively**.**

An illustration on the influences of Error I over all the 25 square cavities is given in Figure III-8 where each square shape represents a square bracket. The green, yellow and red colour represents the square cavities with Error I less than 22 µm, 43 µm and 64 µm. The magnetic holding force differences are then of 10%, 20% and 30%, respectively.

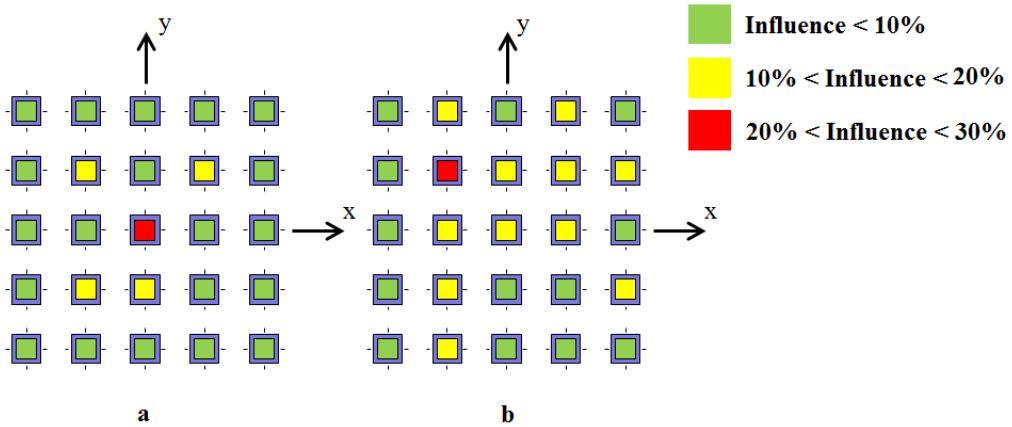


Fig III-8: a. Influence in x-axis direction, b. Influence in y-axis direction

In order to validate the actuation principle, a complete array composed of 25 elementary actuators has been firstly studied. However, strong magnetic interactions among the elementary actuators have been observed. Several MPMs cannot be switched and several MPMs are switched when only one switching control signal is sent. This phenomenon is due to the manufacturing errors of the square cavities. A decision of decreasing the number of MPMs has then done to accomplish the actuation of the array. Moreover, to reduce the stroke variation between the elementary actuators due to the dimensional errors of the square brackets, a pairing of the MPMs with the square cavities has been done. Consequently, 8 MPMs have then been selected and paired with the cavities in order to obtain an identical stroke of 207 µm in both switching x- and y-axis directions for the 8 elementary actuators. Then, a 8-actuators configuration array (Figure III-9) has been formed. The positions of the 8 elementary actuators within the array have been chosen in order to ensure a symmetrical arrangement. The selected square brackets are placed at the corners and at the middle of each side of the array architecture that limits the magnetic interaction force among them. Finally, on an experimental point of view, the use of only 8 actuators simplifies the control of the array compared to 25 actuators array and reduces the cost of experimentation because less independent power supplies (presented in next section) are needed.

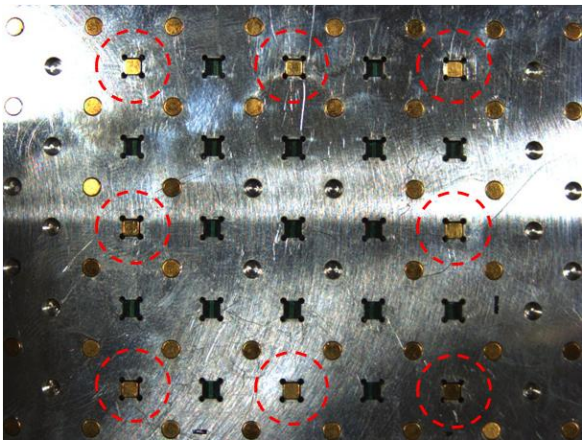


Fig III-9: 8 elementary actuators chosen in experiments

III.3. Experimental characterization

In this section, the experimental characterization of the prototype array and the planar conveyance application are presented.

In this section, firstly, the experimental setup is described. Secondly, the non contact measurement technique used to measure the plate displacement is presented. Finally, the experimental results are detailed.

III.3.1. Equipment setup

In order to control the displacements of the MPMs, a control system has been used. This control system is composed of a computer, a National Instrument (NI) PCI data acquisition board (Table II-3) and four voltage to current converters (V-A converters).

Board	Sampling frequency	Resolution	Utilization	Digital outputs
NI PCI-6733	1 MHz	16 bits	Output	8

Table III-3: PCI card properties

The whole control system is illustrated in Figure III-10. Firstly, a PC equipped with LABVIEW software (NI) is used to generate and send the control signals to the PCI board (PCI-6733). Then, the PCI board outputs 8 independent voltage signals. Each voltage signal is converted by a voltage to current converter (V-A converter) into current signal and then sent to the 8 elementary actuators. However, there is not enough V-A converters to actuate the 8 elementary actuators independently in the lab. The 8 elementary actuators have then actuated by pairs using 4 V-A converters. It has been presented in Chapter II that application of the array is to realize a planar conveyance of a plate. In the experiments, a thin transparent rectangular glass plate with a square black sticker has been used as the plate. The dimensions and the mass of this plate are 50 mm × 50 mm × 0.13 mm and 0.93 g respectively.

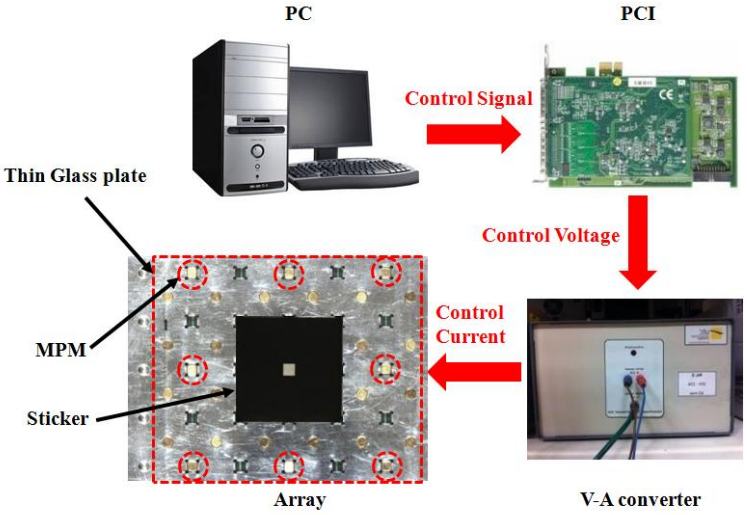


Fig III-10: Array control system

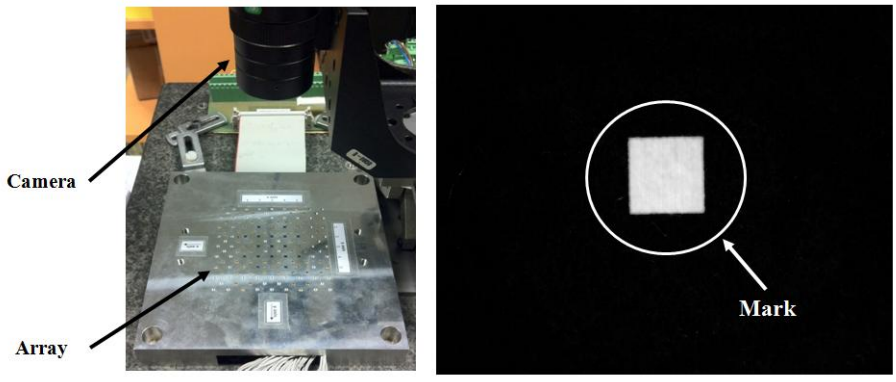
III.3.2. Non contact measurement technique

Using the presented control system, the 8 MPMs of the array have been successfully switched and the glass plate has been successfully moved. However, in order to characterize the performances of the planar conveyance application, a measurement of the plate displacement is necessary. However, this measurement should not disturb the behavior of the device. The mobile part is composed a thin glass layer which is a thin and light object. A contactless measurement technique has then been chosen. A non contact measurement technique based on high frequency capturing camera and a MATLAB image processing program has been developed and implemented. The properties of the camera are given in Table III-4.

Camera	FL2-08S2M/C
Dimensions (L×W×H)	29mm ×29 mm×30mm
Resolution	1032 × 776
Mass	58g
Pixel size	4.65×4.65 µm
Analog to digital converter	12-bit ADC
Maximum Frame Rate	30 FPS
Shutter Speed	0.02 ms -10 s
Image Sensor Model	Sony ICX204 1/3”
Camera Specification	IIDC 1394-based Digital Camera Specification v1.31

Table III-4: Camera properties

The high resolution camera (Figure III-11-a) is placed above the array and is focused on a white square mark on a sticker placed at the center glass plate (Figure III-11-b). The acquisition frequency of the camera has been fixed such that it takes one picture after a switch of all the 8 MPMs.



a **b**

Fig III-11: a. Camera b. Mark on the plate

A MATLAB image post-processing program has been developed and used to analyze the images taken from the camera. The process is illustrated in Figure III-12. Firstly, the image is turned to grayscale (Figure III-12-b) so as to distinguish the square white mark form the sticker. The mark position in the image is then clearer. Secondly, the equations of the sticker four border lines are calculated. By using these equations, the coordinate values of the square white mark four border points are calculated (Figure III-12-c). These coordinate values are used to calculate the coordinate values of the center point on the square white mark which are used to define the plate position.

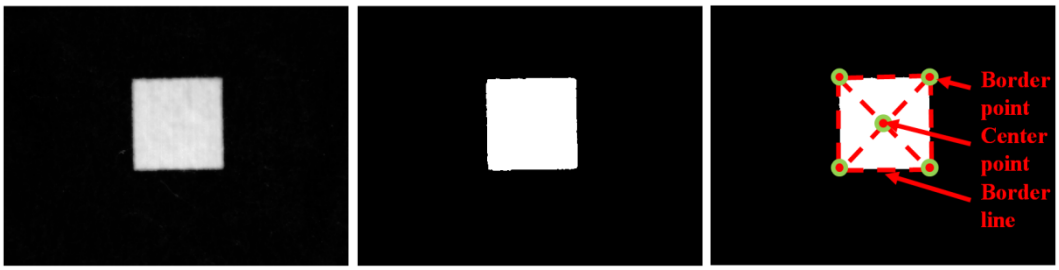


Fig III-12: a. Original image
b. Grayscale model
c. Border and center definition

Finally, the position differences (Figure III-13) of the center point between two consecutive pictures, called "Step size displacement" defines the movement of the thin glass plate. This program is able to measure the step size displacement continuously and outputs the planar trajectory of the sticker.

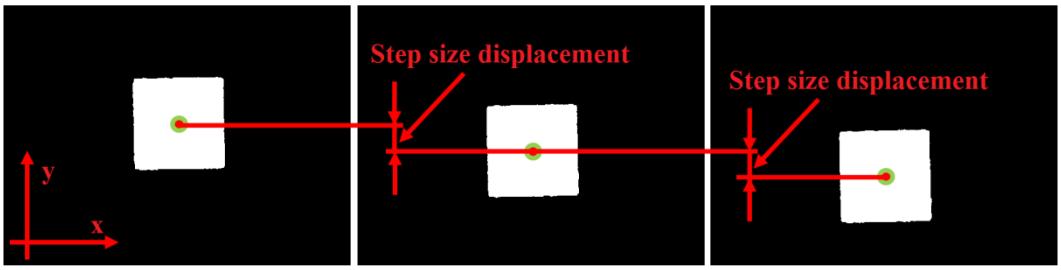


Fig III-13: a. Original image
b. First step movement
c. Second step movement

A calibration target (Figure III-14) with standard diameter dots (62.5 µm) has been used to calibrate the camera (dot center to center spacing is 125 µm). To calibrate the camera, the target is placed on the array and a picture of the target is taken. From this picture, the number of pixels which represents the dots diameter is determined. For the measurement conditions, the camera resolution is determined and corresponds to 10.42 µm/pixel.

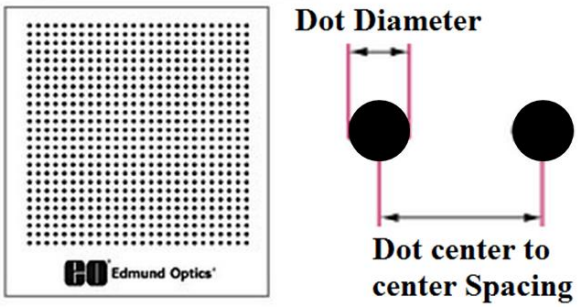


Fig III-14: a. Front view of the target
b. Standard dimension dot

With this non contact measurement technique, the plate displacement (Figure III-15) has been measured and the influences of different controlling parameters have been characterized. In the next section, the experimental results are presented in detail.

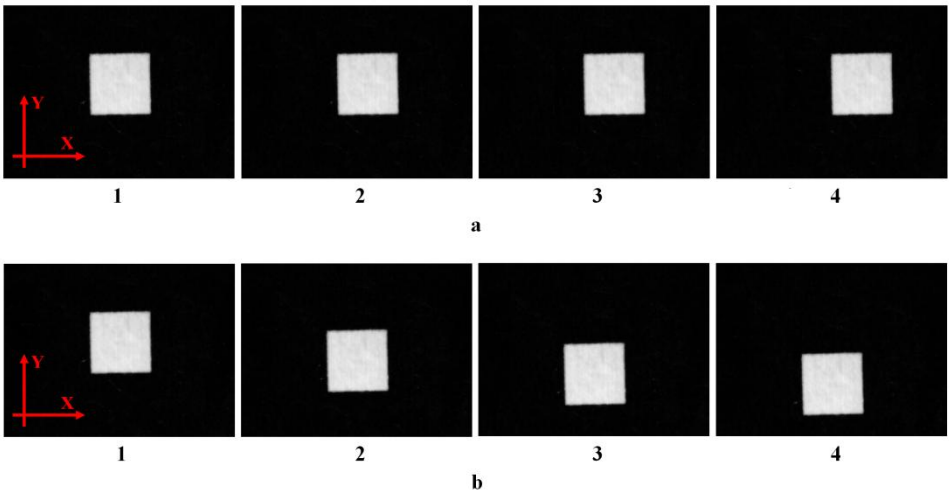


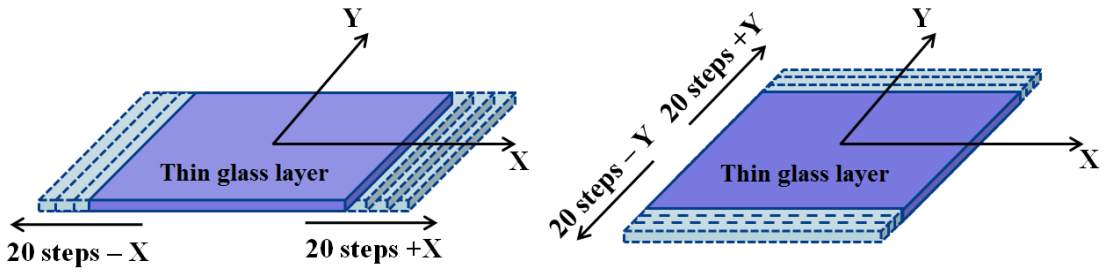
Fig III-15: a. Displacement along x-axis direction
c. Displacement along y-axis direction

III.3.3. Experimental results

In this section, the application of planar conveyance has been tested. According to the switching principle presented in the previous chapter, several control parameters (driving current, holding current, etc…) are used to control the displacement of the MPMs. In order to characterize the behavior of the array, the influences of these parameters on the thin plate displacement value (step size displacement value) have been studied. In the studied application, the thin glass plate has to carry objects placed on its top side. The influence of the additional mass corresponding to these objects has been quantified.

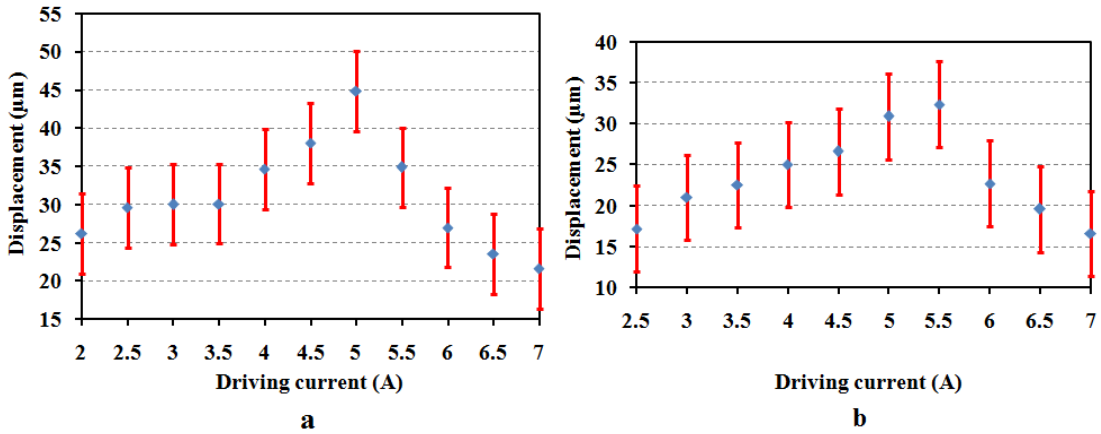
III.3.3.1. Influence of driving current

In this section, the influence of the driving current on the step size has been studied. In this experiment, 20 steps in +x/y direction and then 20 steps in –x/y direction have been realized (Figure III-16). The step size value has been determined for different driving current values set between 2 A and 7 A and no holding current has been used. These driving current values have been chosen because 2A driving current is the minimum current value to displace the thin glass plate and 7A driving current is the maximum current value obtained from the V-A converters. The evolution of the average step size values for different driving current values along x and y-axis are presented in Figure III-17.



a b

Fig III-16: Experimental situation: a. Displacement along x-axis direction, b. Displacement along y-axis direction.



a b

Fig III-17: Influence of driving current to the step size displacement:
a. Displacement along x-axis
b. Displacement along y-axis

The average displacement step size value has been calculated with the 40 displacement step size values (20 steps + and – along x and y-axes respectively). It has been observed that when the driving current increases from 2 A (2.5A for y-axis) to 5 A, the average displacement step size values increases from 26.21 ± 5.21 µm to 44.83 ± 5.21 µm (17.18 ± 5.21 µm to 32.32 ± 5.21 µm) along the x-axis (y-axis) (Figure III-17-a). When the driving current increases from 5 A to 7 A, the average displacement step size values decreases from 44.83 ± 5.21 µm to

21.61 ± 5.21 µm (32.32 ± 5.21 µm to 16.61 ± 5.21 µm). The standard deviation represented in Figure III-17 corresponds to half of a pixel: 5.21 µm (Camera resolution: 10.42 µm). The maximal standard deviations on the average displacement calculated considering the 40 displacement steps are 5.08 µm and 4.83 µm along x and y-axis.

On the other hand, it is expected that when the driving current increases, the displacement step size value decreases. When the driving current increases, the driving forces exerted on the MPMs and their accelerations increase. This acceleration increase generates a high sliding between the plate and the elementary actuators. The displacement step size of the plate will then be small. This phenomenon can be observed for both displacement axes (Figure III-17-a and b), when the driving current value increases from 5 A (5.5 A) to 7 A, the displacement step size value decreases about by half: from about 45µm to 22µm for x-axis and from 32 µm to 17 µm for y-axis. This observation confirms to the sliding phenomena.

However, for the driving current value less than 5/5.5 A, the displacement step size value increases when then driving current value increases. By observing the movement of the elementary actuators, it has been observed that the elementary actuators do not switched simultaneously. This phenomenon is caused by the influences of three factors: the small driving current value, the manufacturing errors of the square cavities and the inhomogeneous contact between all the elementary actuators and the plate. Firstly, small driving current value generates a small driving force on each MPM. Secondly, the manufacturing errors generate inhomogeneous holding forces exerted on all MPM. Thirdly, the inhomogeneous contact between all the elementary actuators and the plate generates inhomogeneous adhesion force between the elementary actuators and the plate. In conclusion, the MPMs, for which the holding and friction forces are the smallest, switch firstly and the switch of the other MPM occurs later thanks to the plate displacement. This time difference induces a loss of collaboration among the elementary actuators which explains the decrease in the average displacement step size value when the driving current is low.

III.3.3.2. Influence of holding current

During the switch of the MPM between two stable positions, a holding current can be used to ensure the contact between the MPM and the lateral stop of the square cavity. In this section, the influence of the holding current value on the displacement step size value is determined. For this experiment, the same conditions as the previous section have been used: 20 steps in + direction and then 20 steps in – direction along x and y axes respectively (Figure III-16). The

holding current value has been set between 0 A and 3 A. The maximum holding current value is set 3 A because it is the maximum holding current to obtain a step size displacement. The influence of the holding current value on the displacement step size value with different driving current is presented in Figure III-18.

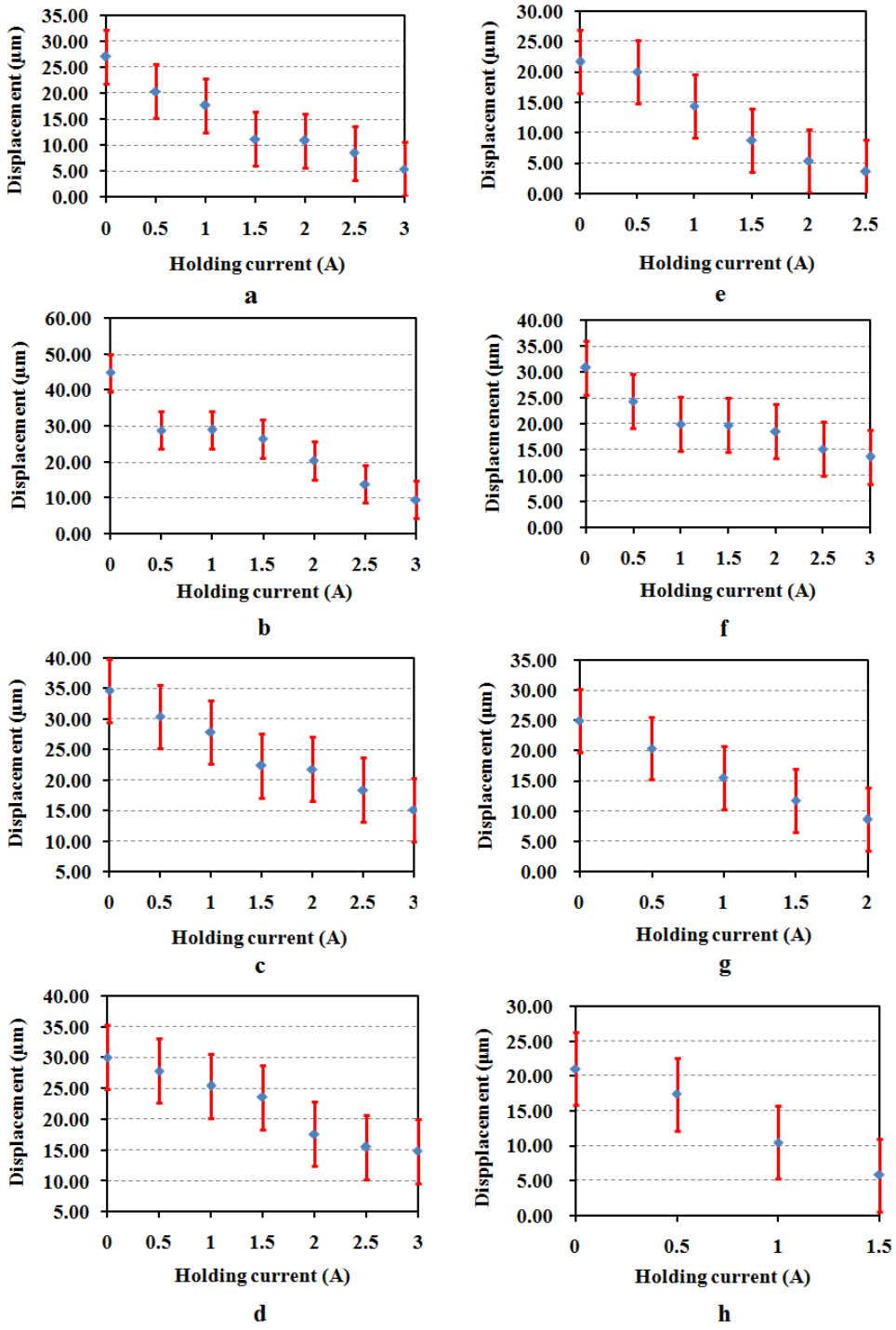


Fig III-18: Influence of holding current on step size displacement:
a. 6A driving current, b. 5A driving current, c. 4A driving current, d. 3A driving current along x-axis
e. 6A driving current, f. 5A driving current, g. 4A driving current, h. 3A driving current along y-axis

In the experiments, 5A driving current is used because it is the nominal current value. In order to do the comparison, 3A, 4A, and 6A driving current are also used in the experiments. The average displacement step size value has been calculated with the 40 displacement step (20 steps + and –, x and y directions respectively) size values of all the experimental test measurements for each holding current value respectively. It has been observed that when the holding current increases, the average displacement step size decreases for all the driving current values (Figure III-18). The maximum standard deviation for the average displacement step size values (4.98 µm) is within the half pixel value (5.21 µm). In the following paragraph, this phenomenon is explained by using Equation III-1 and Figure III-19.

$$F_{holding} = F_{electromagnetic} + F_{magnetic}$$
$$F_{adhesion} = \mu F_{holding} \quad \text{(III-1)}$$

Where $F_{holding}$ is the total holding force, $F_{electromagnetic}$ and $F_{magnetic}$ are the electromagnetic and magnetic holding forces exerted on the MPMs respectively. $F_{adhesion}$ is the friction force between the MPMs and the lateral stop of the square cavities, μ is the corresponding friction coefficient.

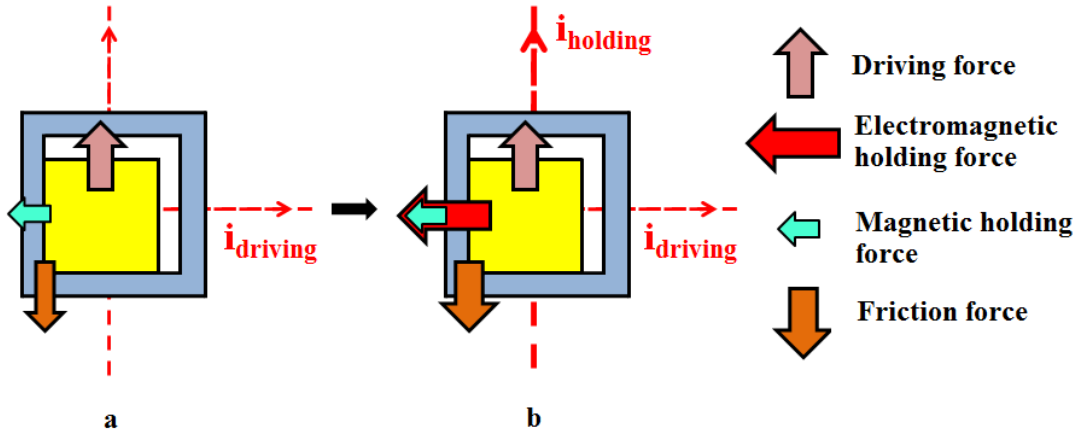


Fig III-19: Influence of holding current: a. Configuration without holding current, b. Configuration with holding current

The use of holding current will generate an electromagnetic holding force exerted on the MPMs which increases the total holding force. The increase of the holding current value generates an increase of the total holding force and of the lateral adhesion force ($F_{adhesion}$) between the MPMs and the lateral stop (Equation III-1). Due to the increasing adhesion force, the net driving force which used to switch the MPMs then decreases. On the other hand, the increase of the adhesion force emphasizes the inhomogeneous adhesion behavior between the

MPMs and the square cavities. The MPMs then don't switch in the same time. The displacement step size values of the plate then decreases. When the holding current value is high enough, $F_{adhesion}$ is high then, the MPMs cannot be switched. As a result, the phenomenon of the displacement step size decreases in value is enlarged.

III.3.3.3. Influence of the current form

In the previous experiments, it has been observed that with a low driving current or with a high holding current, the 8 MPMs don't switch simultaneously. This phenomenon is due to the fact that the adhesion force (between the MPMs and the square cavities) is not perfectly identical for all MPMs. In order to emphasize this effect, experiments on the driving current form have then been performed.

In this experiment, trapezoidal shapes driving current (Figure III-20-b) have been used. With these trapezoidal shapes, the driving current value, then the driving force exerted on each MPM, increases as function of time. With trapezoidal current shapes, the time delay among the MPMs switches will be increased due to the inhomogeneous adhesion forces between the MPMs and their square cavities. This is because the driving forces increase slowly and minimum driving forces to switch each MPM are then different. The current width represents the duration time for which the driving current rises from 0 to its maximum value. When the duration time increases, the slop the current shape will be more flat.

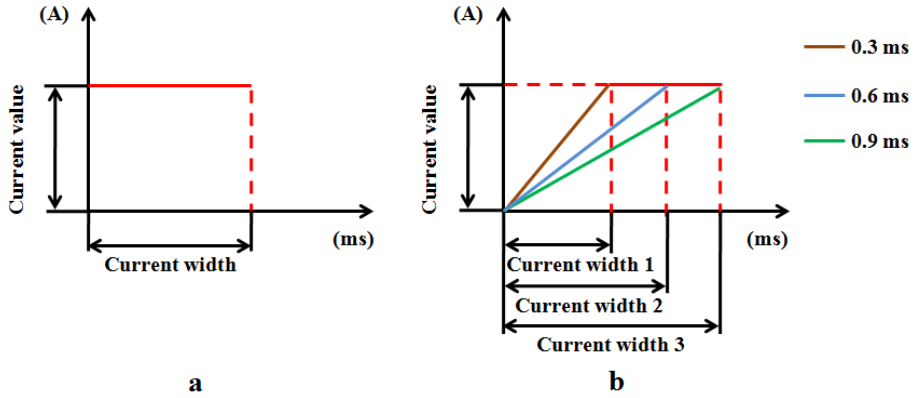


Fig III-20: Driving current type: a. rectangular shape current, b. trapezoidal shape

Experiments have been done using different current slopes characterized by current widths between 0 ms and 1200 ms. A 5 A driving current value (nominal value) has been used for all considered configurations. The relationship between the duration width value of the driving current and the average displacement step size values is shown in Figure III-21 for x-axis. The

maximum standard deviation of all these experimental measurement is 4.26 µm. For a duration time of 0 ms, a rectangular shape driving current has been used for comparison. It has been observed in Figure III-21, an increase of the driving current duration time generates a decrease of the average displacement step size value from 44.83 ± 5.21 µm to 11.52 ± 5.21 µm.

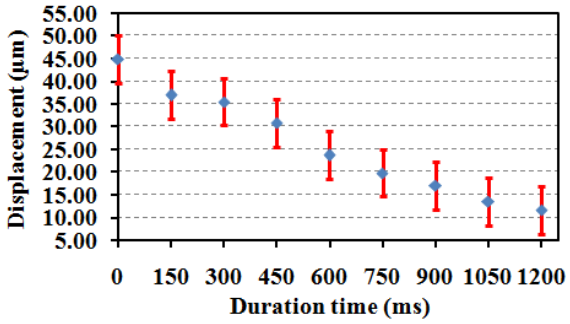


Fig III-21: Influence of trapezoidal shape current

During this experiment, the non-simultaneous switching and the time delay has been clearly observed that confirms the inhomogeneous adhesion force between the MPMs and their square cavities. With the increase of the driving current duration time, the switching time delay among the 8 MPMs is emphasized. The collaborative effect among the MPMs is then highly reduced that generates a low displacement step of the plate (Figure III-21).

III.3.3.4. Influence of the backward displacement of the MPM

As it has been presented in the previous chapter, a full displacement sequence includes simultaneous MPMs displacements along one direction and single backward displacements to the initial position. Theoretically, there is no displacement of the plate during the backward displacement of the MPMs. However, a study on the influence of backward displacement of the MPMs to their initial positions has been carried out to verify this theoretical hypothesis.

In the previous experiments, a picture has been taken after a displacement sequence which includes the simultaneous switch of the 8 MPMs (major step) and the return to the initial positions one after another (small steps). In order to study the backward effect, a picture has been taken after each backward displacement of the MPMs. A 5 A driving current and no holding current have been used for the switch. This current value has been chosen because it ensures the maximum step size displacement. The MPMs backward displacement influence is

then maximized. Ten displacement sequences have been taken into account for illustration in Figure III-22. Each complete step contains 1 major step and 8 small steps.

In Figure III-22-a, the 10 sticker positions are plotted. It has been observed that the influence of the MPMs backward displacement is very small. The details of the first three complete steps are shown in Figure III-22-b. A small variation of the plate position is observed when the MPMs return to their initial positions. The average position change of the plate is 0.70 ± 5.21 µm (the real maximum standard deviation value is 0.50 µm) which represents only 1.56 % of the average major displacement value (44.83 ± 5.21 µm). In conclusion, the influence of MPMs returns to initial positions is negligible.

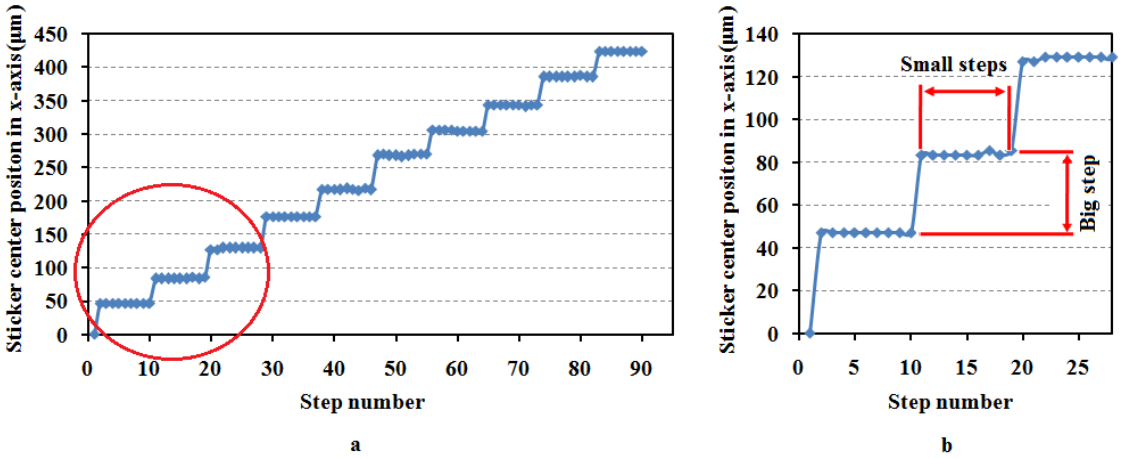


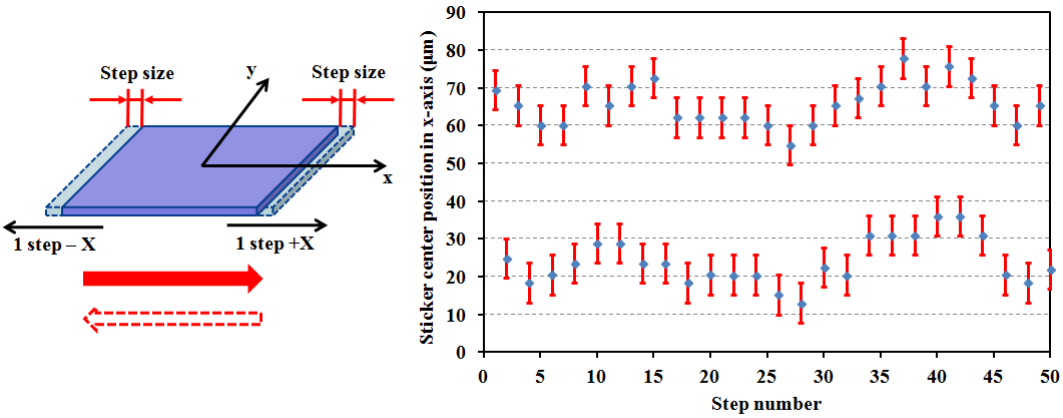
Fig III-22: Influence of displacement step by step: a. Global view b. Focus view

III.3.3.5. Comparison of the forth and back displacements

In the previous experiment, the influence of the backward displacement of the MPM has been studied. It has been proved that the influence of the displacement step size can be neglected. In this section, a study on the repeatability of the major displacement steps is presented. The objective of this study is to verify the repeatability of the displacement step size value.

In this experiment, only the major displacement step is considered, (Figure III-23-a). A 5A driving current and no holding current have been used during this experiment. This driving current value has been used because it can output the maximum displacement step size and is consistent with previous experiments (standard driving current value). During this experiment, 50 forth and backward displacement steps have been realized. The plate position along x-axis is shown in Figure III-23-b. It has been observed that the average major displacement step size value is 43.85 ± 5.21 µm and 41.68 ± 5.21 µm along the x+/-

directions respectively. The real standard deviations of the average major displacement step size along the two directions are 3.84 µm and 3.86 µm respectively.



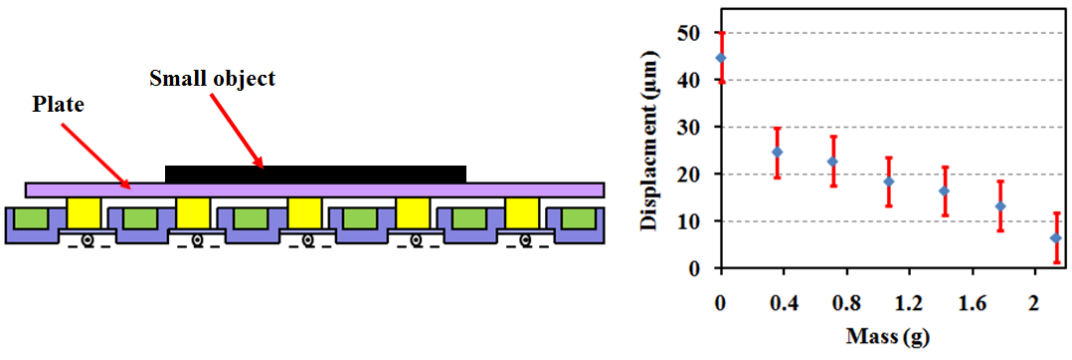
a b

Fig III-23: Influence of forth and back displacement:
a. Motion illustration b. Repeatability illustration

III.3.3.6. Influence of additional mass

The planar conveyance application is considered for the presented array. In this application, an object should be placed on the top side of the plate and moved using the array. The influence of the additional mass due to the presence of this conveyed object has been studied.

In this experiment, small objects (thick paper) with a mass varying between 0 g and 2.1 g have been used. The small objects (Figure III-24-a) have been pasted to the center of the plate surface by the double faced adhesive tape. The mass of the tape has also been taken into account to the total conveyed mass value. A 5 A driving current and no holding current have been used. The experiment has been realized 20 times and the influence of the additional mass value on the average displacement step size is presented in Figure III-24-b.



a b

Fig III-24: Influence of additional mass:
a. Illustration b. Data illustration

It can be observed that an increase of the additional mass value from 0 g to 2.13 g generates a decrease of the average displacement step size from 44.83 ± 5.21 μm to 6.57 ± 5.21 μm (the maximum standard deviation calculated on the 20 displacement sequences is 3.72 μm). This phenomenon can be explained by an adhesion effect. When 8 MPMs have been used, each MPM sustains 1/8 of the total mass (plate mass + additional mass). With the increase of the additional mass value, the adhesion force exerted on each MPM increases, so that the net driving force which is used to move the plate is reduced. The displacement step size is then reduced compared to the situation when on additional mass is added.

With 8 elementary actuators of the prototype array, a maximum additional mass value up to 2.13 g can be successfully conveyed. In perspective, when the complete array with 25 elementary actuators is used, a maximum additional mass value of 6.66 g can then be theoretically conveyed.

III.3.3.7. Realization of long displacement conveyance

During experiments, long displacement plate conveyance has been carried out in order to determine the conveyance displacement limit. This measurement has been realized using a 5 A driving current without holding current. The trajectory of the plate, the relationship between displacement step size and the step number are presented in Figure III-25.

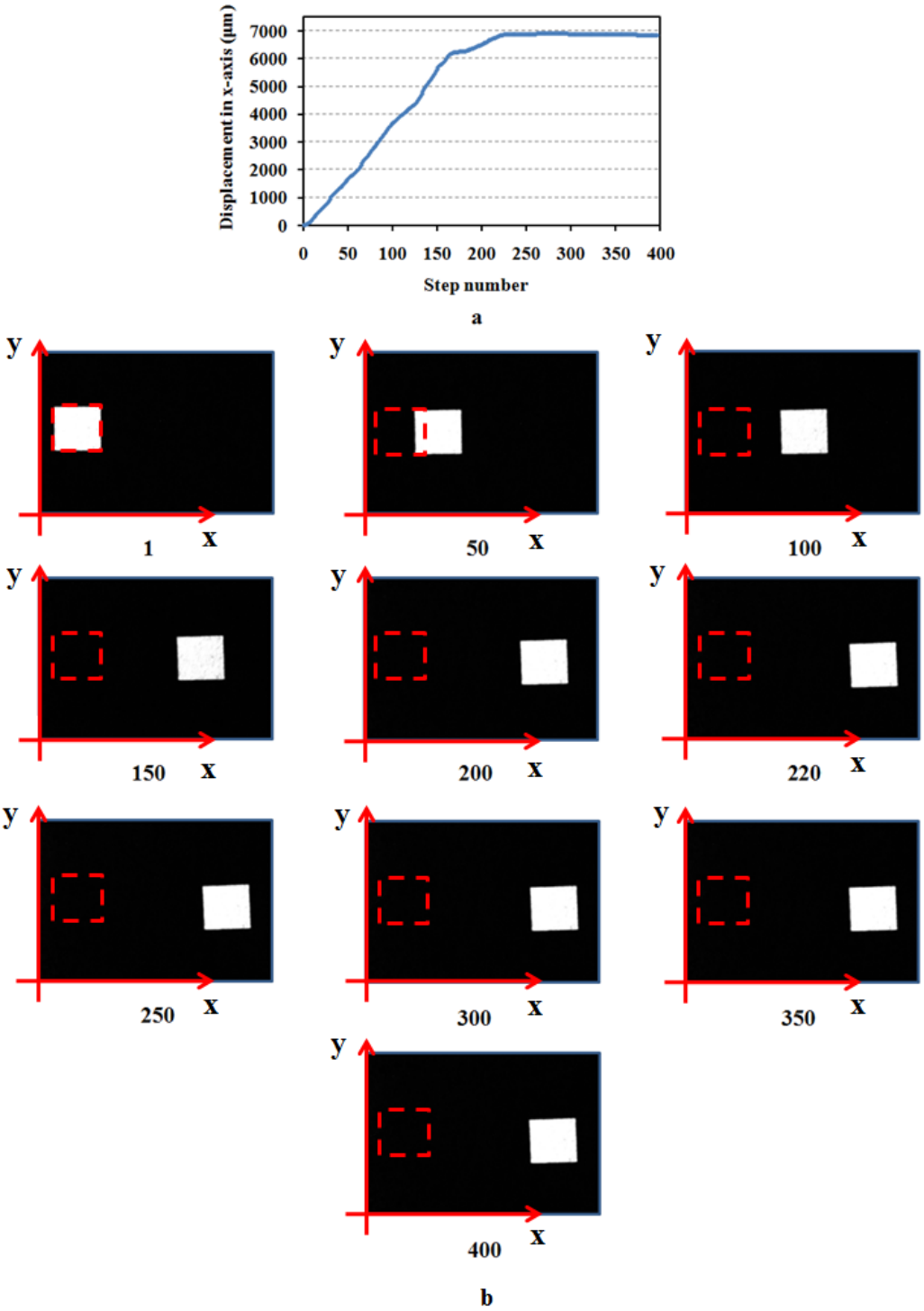


Fig III-25: Influence of long displacement conveyance:
a. Displacement along x-axis b. Sticker position in pictures

In this experiment, 400 displacement sequences have been realized. From Figure III-25-a, it has been firstly observed that with the increase of steps numbers (from 0^{th} to 164^{th}), the displacement step size value of the plate is almost linear (-198.03 µm displacement along y-axis direction in total). From the 164^{th} step to the 218^{th} step, the displacement step of the plate

seems randomly in function of the step number. After 220 steps the glass plate moves so slightly that we could consider that it stops.

This phenomenon can also be explained by the adhesion effect. When the plate is at the central position on the array, the mass of the plate is equally distributed on the MPM. When the glass plate moves, its gravity center moves away from the array center (Figure III-26). The mass distribution is then not perfectly distributed on the MPM and the adhesion forces of the MPMs become inhomogeneous. As a consequence, the displacement step size reduces. When the displacement of the plate reaches 6.88 mm, the plate border has already gone out of the boundary of the array. Several MPMs lose the contact with the plate then it stops to move.

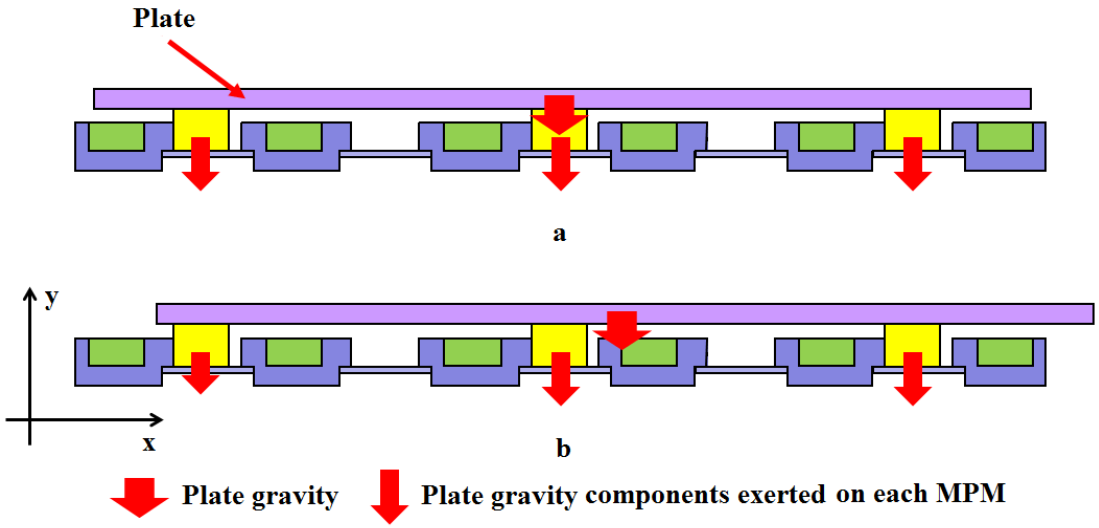


Fig III-26: Influence of long displacement:
a. Plate initial position b. Plate position after several switching

It has been observed that the mark moves linearly along the x-axis direction within 100 steps that represents a pate displacement of 3.71 mm (Figure III-25-b). After 100 steps, the plate begins to rotate. This rotation is also due to the inhomogenous adhesion force from the MPMs to the plate. Finally, when the steps arrive at about 220, it is clear that optically the plate doesn't move (from picture 200 to 400).

In conclusion, by using the prototype array with 8 MPMs, 5 A driving current and no holding current, a maximum long displacement of about 6.8 mm (Figure III-25-a) has been realized along x-axis direction. However, a linear displacement step size of the plate in long range conveyance is possible within 100 steps.

III.3.4. Conclusion

In this chapter, the prototype array and the application as a planar conveyance device have been detailed. From the static point of view, the manufacturing errors of the array components (square cavities and MPMs) have been measured. By using the static model in RADIA (Chapter II), these fabrication errors have been taken into account and their influences characterized using the model. Finally, the array composed of 8 MPMs has been used during the experimental tests.

From the experimental test, firstly the control system (PC + PCI + Power supply + prototype array + Camera) has been described. Secondly, the non-contact measurement method, based on image processing developed on MATLAB, has been presented. Finally, the experimental performances of the prototype array have been studied along x and y-axes. This experimental performance study of the prototype array is based on the planar conveyance application of the array. The influences of several parameters (driving current value, holding current, current shapes and etc...) have been studied based on the functioning of the conveyance system.

From the experiments results, it has been observed that with the increase of the driving current value, the average displacement step size value firstly increases due to the increase of the driving force exerted on each MPM and then decreases due to the sliding effect between the MPMs and the plate. The holding current value and the trapezoidal shape driving current shape both have a negative influence over the step size displacement. An increase of the holding current increases the lateral adhesion force between the MPMs and the stops of the square cavities. There is then not enough net driving force to move the plate. For the trapezoidal shape driving current, it emphasizes the inhomogeneous adhesion force present in the device. As a consequence, the collaboration of the MPMs is degraded. Finally, the device can be used to convey small parts on long distances. The maximum movable mass and the longest conveyance distance are 2.13 g and 3.71 mm respectively.

Chapter 4: Optimization design of the prototype array

In the previous chapter, the performances of the prototype actuators array have been characterized. During the experimental tests, it has been observed that there is behavior inhomogeneity for all elementary actuators which can disturb the array functioning. In order to reduce this inhomogeneity and to improve the array performances, an optimization study is proposed in this chapter in order to get an optimal array design.

This chapter is divided into three parts. In the first part, an overview of the existing optimization techniques is presented. From this overview, the genetic algorithm technique has been selected for this optimization study. In second part, the implementation of the genetic algorithm is presented. Single-objective and then multi-objective optimizations have then been realized and the results are compared. In the final part, the design of an optimized array is proposed.

IV.1. Optimization techniques

IV.1.1. Context of the optimization study

The proposed digital actuators array is based on several elementary digital actuators organized in matrix architecture. The objective of this array is to realize complex tasks (conveyance of objects) obtained by combining elementary actions from the elementary actuators. The homogeneity holding forces of the actuators array is an important parameter to ensure that all elementary actuators have the same influence on the global task. On the other hand, the magnetic interactions between the elementary actuators caused by the assembly can disturb the array behaviour. The self-return zone is also an important parameter. It represents the robustness of the actuator (ability of maintaining the stable positions) to external disturbance. In order to obtain a better behavior (homogeneity holding forces, less magnetic interactions and better robustness of elementary actuators) compared to the existing prototype array, three performance indicators have been defined. These indicators are the maximum variation of holding forces (*VF*), the average interaction force (*IF*) and the average length of self-return zone (*SRZ*). The first parameter (*VF*) is calculated with equation IV-1.

$$\begin{aligned} \max F_{holding} &= \{f^1_{holding}, f^2_{holding}, \ldots, f^{25}_{holding}\} \\ \min F_{holding} &= \{f^1_{holding}, f^2_{holding}, \ldots, f^{25}_{holding}\} \\ VF &= \max F_{holding} - \min F_{holding} \end{aligned} \qquad \text{(IV-1)}$$

Where $f^i_{holding}$ represents the holding force exerted on the i^{th} elementary actuator. The *VF* parameter characterizes directly the homogeneity of the array. A minimization of the *VF* parameter will reduce non-homogeneity of the array. The second parameter (*IF*) is calculated with the equation IV-2.

$$IF = \text{average}\{f^1_{interaction}, f^2_{interaction}, \ldots, f^{25}_{interaction}\} \qquad \text{(IV-2)}$$

Where $f^i_{interaction}$ represents the magnetic interaction force exerted on the i^{th} elementary actuator. The *IF* parameter characterizes the magnetic interaction forces between the elementary actuators. A minimization of the *IF* parameter will decrease the magnetic interferences among the MPMs of the elementary actuators. The third parameter (*SRZ*) characterizes the robustness functionality of the elementary actuators. It evaluates the bistability of each elementary actuator. The equation used to calculate this parameter has

already given by Equation II-6 in chapter II. A maximization of the *SRZ* parameter will enhance the MPMs ability to return to stable position without energy supply and then minimize the possibility of unpredictable behaviors.

In order to obtain a homogeneous and robust digital actuators array, these three performance indicators should be simultaneously optimized. Multi-Objectives (MO) optimization methods are then needed for this optimization study. In the next paragraph, several existing MO optimization techniques are presented.

IV.1.2. Multi-objectives optimization techniques

MO optimization is a mathematical method whereby several objectives are simultaneously taken into account to obtain an optimal solution [GERA 2009]. Generally, a MO optimization problem can be defined as [ASIM 2002]:

$$\begin{aligned} &\min f(\mathrm{x}) = \{f_1(\mathrm{x}), f_2(\mathrm{x}), ..., f_M(\mathrm{x})\} \\ &\text{subject to } g_j(\mathrm{x}) \le 0 \quad j = 1, J \\ &\text{and} \qquad h_k(\mathrm{x}) = 0 \quad k = 1, K \end{aligned} \tag{IV-3}$$

Where f is the vector of objective functions, x is the vector of design variables, g_j is the j^{th} inequality constraint, h_k is the k^{th} equality constraint, and M, J, and K are the total number of objective functions, inequality constraints, and equality constraints, respectively.

There is no unique solution to this problem if any of the objectives f (x) conflict with each other. As a result, the concept of non-inferiority also called Pareto optimality in [Cens 1977] must be used to characterize the objectives. Non-inferior solution is one solution in which an improvement in one objective requires a degradation of another. A feasible space Ω in the design variable space has been proposed in order to define the conception. Definition of Ω has been given in equation IV-4 [CENS 1977].

$$\Omega = \{\mathrm{x} \in R^N\} \tag{IV-4}$$

x is an element of the N-dimensional (N is the design variables total number) real numbers x∈ Ω that satisfies all the constraints in equation IV-3. Objective function space Λ is then defined in equation IV-5 [CENS 1977] :

$$\Lambda = \{y \in R^M : y = f(\mathrm{x}), \mathrm{x} \in \Omega\} \tag{IV-5}$$

An example of Ω and Λ with two design variables (x_1 and x_2) and two objective functions ($f_1(x)$ and $f_2(x)$) are shown in Figure IV-1 to illustrate the relationship between Ω and Λ. A design variables vector in Ω is related to an objective vector in Λ.

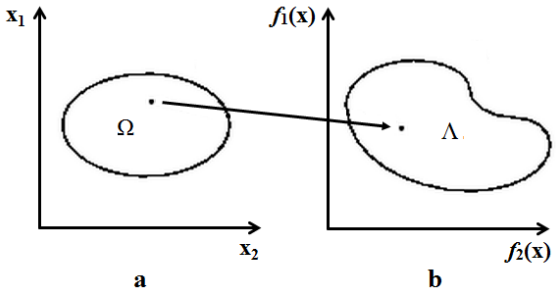


Fig IV-1: Mapping from design variable space into objective function space:

a. Design variables feasible space b. Objective function space

Based on these definitions, a non-inferior solution has been defined [CENS 1977]. Vector $x^* \in \Omega$ is a non-inferior solution if for some neighborhood of x^* there does not exist a Δx such that $(x^*+\Delta x) \in \Omega$ and subject to equation IV-6.

$$\begin{aligned} f_m\left(x^* + \Delta x\right) &\le f_m\left(x^*\right) \quad m = 1, M \\ f_p\left(x^* + \Delta x\right) &< f_p\left(x^*\right) \quad \text{for at least one } p \end{aligned} \tag{IV-6}$$

Non-inferior solutions set in the objective function space can be illustrated in Figure IV-2. In this illustration, a two-dimensional objective function space has been used as the example. In Figure IV-2, the non-inferior solutions set exists on the curve between point *C* and *D*. The points *A* and *B* are two typical non-inferior points because an improvement in one objective requires a degradation of the other objective. For example, the $f_1(x)$ decreases with the increase of $f_2(x)$ ($f_1(A) > f_1(B)$ & $f_2(A) > f_2(B)$). As a result, there is no point in Ω which can attain the most improvement of all the objectives. MO optimization is a method which focuses on the generation and selection of non-inferior solution points. The set which includes all the non-inferior solutions is called non-inferior solution set and can also be called the Pareto optimal front. A general goal in multi-objective optimization is constructing the Pareto optimal front [CENS 1977]. The decision-maker then can choose the desired solution from the Pareto optimal front.

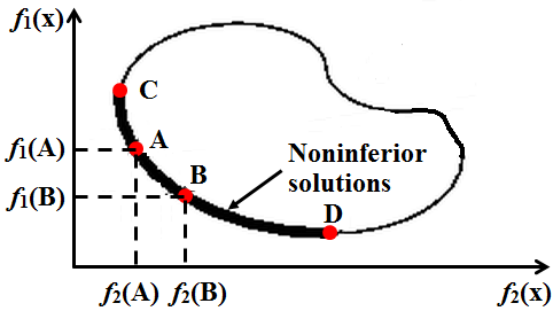


Fig IV-2: Set of non-inferior solutions

Generally, there are two approaches to solve MO optimization problems. The first approach is based on the combination of individual objective functions into a single composite function. This combination is realized using different methods such as the "Weighting Objective Method", the "Multi-level Optimization Method", the "Trade-Off Method" and the "Global Criterion Method".

IV.1.2.1. Weighting Objective Method

The Weighting Objective Method aims to convert a MO problem into a SO problem by using a weighted sum of the original multiple objectives (Equation IV-7) [ASIM 2002]:

$$\begin{aligned} & \min \sum_{i=1}^{M} w_i f_i(\mathrm{x}) \\ \text{subject to } & g_j(\mathrm{x}) \le 0 \quad j = 1, J \\ \text{and } & h_k(\mathrm{x}) = 0 \quad k = 1, K \\ & 0 < w_i \le 1 \\ & \sum_{i=1}^{N} w_i = 1 \end{aligned} \tag{IV-7}$$

Where w_i is the weighting coefficient that should have been chosen due to the priority and importance of the objective f_i. The Pareto optimal solutions set can be obtained by varying the weighting coefficients.

The main advantage of this method is its simplicity. For a convex form of objective function space (e.g. Figure IV-2), it guarantees to find solutions on the entire Pareto optimal front. However, for the non-convex objective function space, the weighting objective method will not supply a complete Pareto optimal front [CARA 2008]. A study on the convexity of the objective functions should then be realized before optimization. Moreover, the choice of the

weighting coefficients depends on the experience of the decision-maker. Thus, different choices of w_i will result in different output results.

IV.1.2.2. Multi-level Optimization Method

The second MO optimization method is the Multi-level Optimization Method which requires a classification of the objectives in a decreasing order importance, e.g. let f_1 be the most important objective and f_M the least important objective.

Two steps have to be realized to complete the optimization procedure. At the first step, a SO optimization is done which considers only the most important objective $f_1(x)$ and the original constraints. The optimization result is defined as f_1^*. At the second step, the optimum solution f_i^* of the i^{th} objective function $f_i(x)$ subjected to the constraint in Equation IV-8 [ASIM 2002] has to be fund and this has to be repeated for $i = 2$ to M. The MO problem is then converted into a SO problem.

$$\begin{aligned} &\min f_i = f_i^* \\ &\text{subject to } x \in \{x \left| f_{i-1}(x) \le \left(1 \pm \frac{\varepsilon_{i-1}}{100}\right) f_{i-1}{}^* \right.\} \end{aligned} \tag{IV-8}$$

Where, ε_i is the percentage variation allowed in the objective function value f_i^*. This constraint ranks the importance of the last calculated objective. The percentage could also be equal to zero and different choices of ε_i by the designer will result in different output results. By changing the values of ε_i, a set of Pareto optimal solutions can be obtained, Pareto optimal front is then produced using this algorithm.

The advantage of this algorithm is its easy understanding and implementation. It is also applicable to non-convex objective function space problems. However, it is difficult for decision-maker to choose the ε_i for the objective functions.

IV.1.2.3. Trade-Off Method

The Trade-Off Method is also known as ε – constraint or reduced feasible method. This method involves searching in a progressively reduced objective functions space [ASIM 2002]. This method also focuses on converting the MO problem into a new SO problem. In this SO problem, one objective is minimized. The other $M - 1$ objectives are converted into constraints that limits the values of the remaining objectives and the original constraints (Equation IV-9).

$$\begin{aligned} &\min f_r(\mathrm{x}) \\ &\text{subject to } f_i(\mathrm{x}) \le \varepsilon_i \qquad i = 1, M; i \ne r \end{aligned} \tag{IV-9}$$

Where, $\mathcal{E}_i$ is the limiting value of f_i which is decided by the decision-maker. By varying the $\mathcal{E}_i$ values, a complete set of Pareto optimal solutions can be obtained.

This optimization method can also be used for MO problem with non-convex objectives function space. With different $\mathcal{E}_i$ values, different Pareto optimal solutions can be found. However, there are several limitations for this method. The decision-maker has to choose appropriate upper bounds ($\mathcal{E}_i$) for the constraints. Moreover, the method is not particularly efficient if the number of objective is greater than two [CARA 2008].

IV.1.2.4. Genetic algorithm

The second approach to solve a MO optimization problem considers the objective functions simultaneously. In literature, Genetic Algorithm (GA) method is found to be an attractive tool for solving MO optimization problems as it can search for many non-inferior solutions at the same time.

GA is a global optimization method based on the principles of natural selection and evolutionary theory [QIAN 2010]. In GA terminology, each design variable is called a gene and an individual is defined by a design variables vector x. GA operates with a collection of individuals which is called a population. The population is randomly initialized. The calculation iterations in GA are called generations. In each generation, the individuals are evaluated by the objective functions which have been grouped and called fitness functions. Objective (fitness) functions are the mathematic equations which calculate the objectives (fitness) values. GA provides a fitness value to each individual in the same generation based on the evaluation of the fitness functions. After the evaluation, the initial individuals are operated by three operators i.e. Crossover, Mutation and Selection based on their fitness values. These three operators are used to generate a new population. With the Crossover operator, two individuals (with better fitness values) call parents are selected in the initial population. These two parent individuals are then combined together with an exchange of genes to form two new children individuals so that these new individuals are expected to inherit the improvement of fitness values. With the operations of applying the crossover operator iteratively, the most efficient individual genes then can appear more frequently in the population. Finally, this frequently appearance of efficient individuals will lead to the MO

optimization convergence to an overall efficient solution [KONA 2006]. The mutation enlarges the diversity of the genes in the population. The mutation operator randomly introduces random changes in gene values of individuals. By changing randomly the genes in the individuals of the parent generation, new individuals are obtained. With the operations of applying the mutation operator iteratively, new genes are expected to be reintroduced back into the population to get a higher genetic diversity. This operator allows escaping from local optima [KONA 2006]. After the operation of the two operators, a selection of the new individuals generated from the previous two operators is done to form a new population. In most cases, this selection procedure is based on the fitness values of these new individuals which determine the individual survival chance for the next generation. The individuals which own better and suitable fitness values have more chance to be selected and kept into the next generation by the selection procedures. There are different selection procedures in GA depending on how the fitness values are used, i.e. proportional selection, ranking, and tournament selection [KONA 2006]. A general procedure of the GA optimization is illustrated in Figure IV-3.

The GA procedure is summarized in the following steps:

- Step 1: Initialization and evaluation
  - Set G =1. G represents the generation number.
  - Randomly generation of N individuals to form the initial population, P^1 with respect to the constraints of each design variables.
  - Evaluation of the fitness functions of individuals in P^1.
- Step 2: Selection, crossover, mutation
  - Crossover: Generate a children population Q^G. Choose solutions from P^G based on the fitness values. Using a crossover operator, generate individuals and add them to Q^G.
  - Mutation: Mutate each individual $x \in Q^G$ with a predefined mutation rate.
  - Selection: Evaluate the new population and assign a fitness value to each solution $x \in Q^G$ based its objective function value. Select N solutions from Q^G based on their fitness and assigned them P^G+1.
- Step 3: Termination
  - If the output condition is satisfied, terminate the search and return the current population, else, set G=G+1 go to Step 2.

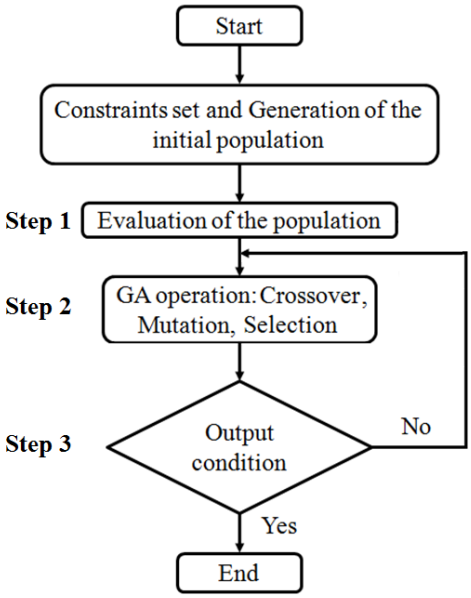


Fig IV-3: GA optimization procedure

The GA optimization method is more complex and difficult to implement compared to the other methods. However, the GA ability which considers a number of different design variables simultaneously makes it possible to find a diverse set of Pareto optimal solutions even for several special situations such as complex problems with non-convex, discontinuous objective function space [KONA 2006]. As a result, a study on the objective function space of the MO optimization problem is not necessary. Moreover, this method does not require the decision-maker to prioritize, scale, or weight objectives. The influence of inappropriate choice on these parameters can then be minimized.

IV.1.3. Comparison of the MO methods

In the previous section, two main approaches to solve the MO optimization problems with different methods have been presented. They are all commonly used in practical situations. However, each method has its own advantages and disadvantages.

For the first approach, the methods are focusing on converting a MO optimization problem into a SO optimization problem. As a result, they have the advantage to be easily understandable and implementable. However, all these algorithms require additional inputs from the decision-maker e.g. w_i, $\mathcal{E}_i$. The selection of the values for these additional parameters depends on the designer's experience. In practice, it can be difficult to precisely and accurately select these parameters. Moreover, these algorithms have to be run many times to find several solutions in the Pareto optimal set [JAIM 2009]. When many objectives and

design variables are taken into account, the problems become large and complex. For several methods e.g. Weighting Method, a study of the objective functions space have to be done to verify its convexity and continuity.

For the second approach, the MO optimization problem is fully considered. The GA optimization method is based on this approach and is more complex to be understood and implemented compared to the first approach methods. It does not require the decision-maker to prioritize, scale, or weight objectives. However, it requires the decision-maker to fix the other parameters such as crossover percentage, mutation, percentage and etc. In addition, it takes into account simultaneously many objectives and variables and is able to find a set of Pareto optimal solutions in a single run. Moreover, a study of the objective function space is also unnecessary.

In our optimization study of the digital actuators array, 14 design variables parameters (presented in the next section) and 3 objectives (early presented in this chapter) are considered. In order to avoid getting local optimal solutions by setting the parameters such as weight arbitrarily and to simplify the optimization procedure (GA can take into account massive of objectives, variables simultaneously and able to find a set of Pareto optimal solutions in a single run), MO optimization method based on GA has been chosen to optimize the design of the actuators array. In the following section, the MO optimization method based on GA is presented.

IV.2. Genetic optimization realized in MATLAB

For the implementation of the array optimization with GA, MATLAB software has been used. In MATLAB software, GA optimization function has been realized using the Global Optimization Toolbox (GOT). The MATLAB static model (presented in Chapter II) which computes the magnetic forces and the *SRZ* value has been used to evaluate the fitness functions. The optimization of the array performances has then been carried out.

IV.2.1. Performance indicators

The main objective of the presented digital actuators array is to realize a planar conveyance task via the contributions of each elementary actuator. Three conditions have been defined to ensure the realization of conveyance task using the array. An independent control of the elementary actuators is needed to ensure the realization of dedicated tasks such as rotations.

This independent behavior represents the first condition. The second condition is the need of a homogeneous behavior of the array. The impact of each elementary actuator on the complex actions has indeed to be identical regardless to the position of the considered elementary actuators in the array. The third condition characterizes the digital behavior of the elementary actuators and specially the robustness of each actuator to external disturbances. Considering these three conditions, three performance indicators have been defined to characterize the optimal design.

The first performance indicator is the average length of the self-return zone (*SRZ*) of the elementary actuators. As presented in Chapter II, the *SRZ* characterizes the digital behavior of the elementary actuators. *SRZ* corresponds to the maximum distance from the stable position where the MPM could return to the nearest stable position without input current. An increase of *SRZ* will enhance the ability of MPM to returns to its stable positions in presence of high disturbances.

The second performance indicator is the average magnetic Interference Force (*IF*) among the elementary actuators. When the elementary actuators are combined together in an array, the MPMs magnetically interfere with each other. The decrease of *IF* will enable less magnetic interferences among the elementary actuators then ensures a more independent behavior of the elementary actuators.

The third performance indicator is the maximum Variation of magnetic holding Force among all the elementary actuators in the array (*VF*). A minimization of the magnetic holding variation force variation ensures indeed a more homogeneous behavior of the array.

The three defined performance indicators are *SRZ*, *IF* and *VF*. To optimize the array, a maximization of *SRZ* and *VF* and a minimization of *IF* have to be carried out.

IV.2.2. Design parameters

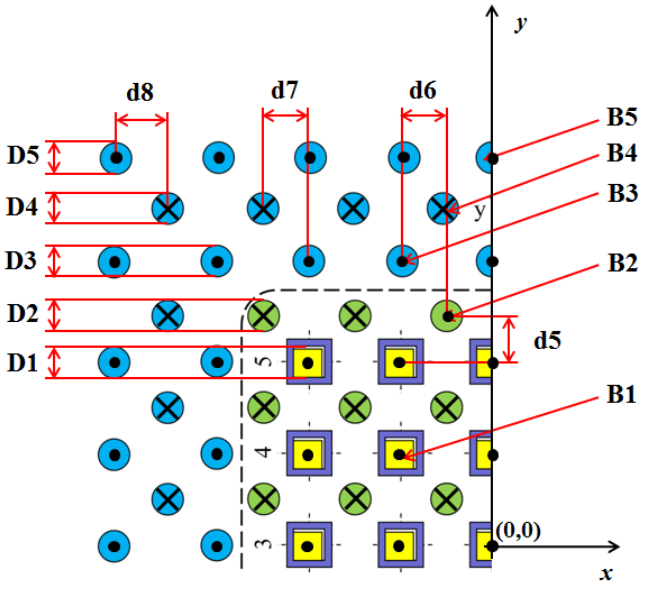


Fig IV-4: 14 design parameters

The design of the array is defined according to 14 design parameters (Figure IV-4). These parameters characterize the magnetic properties (Bx), the PMs dimensions (Dx) and the distances between the components of the array (dx). The design parameters are listed below:

- PM magnetizations:
  - B1 for MPM magnetization,
  - B2 for FPM magnetization,
  - B3 for FPM1 magnetization,
  - B4 for FPM2 magnetization,
  - B5 for FPM3 magnetization.
- PM dimensions:
  - D1 for MPM dimensions in length,
  - D2 for FPM dimensions in diameter,
  - D3 for AFPM1 dimensions in diameter,
  - D4 for AFPM2 dimensions in diameter,
  - D5 for AFPM3 dimensions in diameter.
- Distances between PMs:
  - d5 for the distance between MPMs and FPMs,
  - d6 for the distance between FPMs and AFPM1s,
  - d7 for the distance between AFPM1s and AFPM2s,
  - d8 for the distance between AFPM2s and AFPM3s.

The constraints range for the design parameters are [0.5 T ; 1.5 T], [1 mm ; 3 mm] and [2 mm ; 5 mm] for the PMs magnetization, the PMs dimensions and the distances between PMs, respectively. These value ranges are chosen because for the NdFeB magnet (used in presented work), it is currently not possible to achieve a magnetization higher than 1.5 T. Regarding to

the dimensions and distances, the presented values ([2 mm ; 5 mm]) are chosen aiming to reduce the size of the array.

IV.2.3. Single-objective optimization

In the optimization study, three SO optimizations of the array have been firstly implemented considering the three performance indicators independently. These SO optimization studies enable to obtain the maximum performance indicator values that can be obtained independently. These values will also be used to compare and to characterize the performances of the optimal array design obtained in a second time by a MO optimization.

IV.2.3.1. Optimization setup

To implement the SO optimization, the function GA in the Global Optimization Tool (GOT) toolbox of MATLAB software has been used.

An initial programming parameter setting of GA has been realized to characterize the population size, the maximum iteration generation number and the output conditions (presented in GA procedure section). For the SO optimization, the population size is set to 50 by default in MATLAB GOT. An increase of this value increases the diversity of the initial input individuals and then increases the possibility to find most optimal solutions. However, for an optimization study with a huge number of design variables and complex fitness function, a big population size will greatly increase the calculation time at each generation. As a consequence, in our case (with 14 design variables and complex magnetic calculation fitness function), the population size is set at 40 to decrease the calculation time. The calculation time for a single individual is about 10 minutes with an Intel i3 CPU (3.3 GHz) and 6 Go RAM PC then about 6.5 hours for a single generation (40 individuals).

The maximum generation number is set to "100 × number of Variables (14 design variables)" by default in MATLAB GOT. As it has been previously presented, the generation size represents the iteration number calculated in GA. If many generations are evaluated, the possibility to find the most optimal solutions is increased. However, it will also significantly increase the calculation time. As a result, the maximum number of generation has been fixed to 100 to reduce the computer calculation time. For the considered problem and with these choices (population size and number of generations), the calculation time for the optimization study is about 28 days.

For the termination of the SO optimization, three output conditions can be defined. The first one is the maximum generation number presented in the previous paragraph. When the number of generations is equal to 100, the optimization study stops. The second output condition is the time limit which specifies the maximum time in seconds during which the optimization study runs before stopping. This condition has not been used for the presented optimization study, the time limit has then fixed at infinite. The third condition is the fitness function tolerance. The GA stops if the average relative change in the best fitness function value over the generations is less or equal than the fitness function tolerance. The fitness function characterizes the convergence of the optimal solutions. When the tolerance is small, GA considers that the best solution value converges to a certain value, it then stops. For the present optimization study, the fitness function tolerance has then been fixed at 1×10^{-6} by MATLAB default.

IV.2.3.2. Single-objective optimization results

In this section, three SO optimizations considering the three performance indicators separately are presented. These three SO optimizations are then terminated due to the third output condition: average change in the fitness value less than fitness function tolerance. The maximum calculation time is about 72 hours for the three optimization calculations.

The three optimal array geometries are presented in Figure IV-5.a, b and c which correspond to the optimization of *SRZ*, *IF* and *VF*, respectively. In this figure, the PMs dimensions and the distances are represented at scale. The PMs magnetization values are represented using color depth. The dark red and dark blue colors correspond to the maximum positive (+1.5 T) and negative (-1.5 T) magnetization values respectively. The white color represents a magnetization of 0 T.

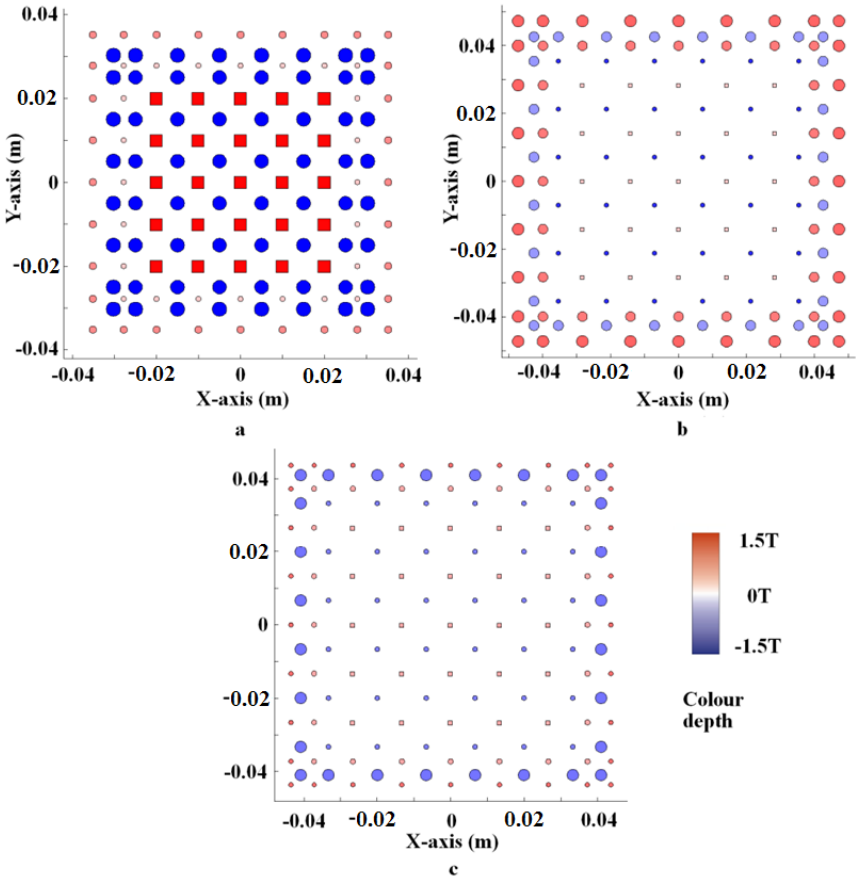


Fig IV-5: SO optimizations on different objectives: a. *SRZ*, b. *IF*, c. *VF*

The Figure IV-5-a represents the optimized array geometry obtained while considering a maximization of the *SRZ* performance indicator. Obviously, in this configuration, the MPM and FPM magnetizations and dimensions are maximal and the distance between them is minimal. This configuration ensures a maximal magnetic holding force exerted by the FPMs on the MPMs then the maximum value of *SRZ*.

The Figure IV-5-b presents the geometry obtained when the *IF* performance indicator is minimized. In this configuration, the MPM dimensions and magnetizations are minimal and the distance between the MPM and the FPM, then between the MPMs, are maximal. This configuration then minimizes the magnetic interaction force between MPMs.

The array geometry obtained with a minimization of the *VF* performance indicator is presented in Figure IV-5-c. In this configuration, the MPMs, the first and third rows of AFPMs dimensions and magnetizations are minimal. The dimensions of the second rows of AFPMs is maximal. With this configuration, the actuators located at the boundary of the array are well magnetically balanced. The *VF* between elementary actuators is then minimized.

In this study, the three performance indicators have been independently optimized. For each SO optimization, the indicator taken into account is only optimized and the other ones are not considered in the optimization process. The SO optimization results are presented in Table IV-1. The performance indicators of the existing prototype array - *SRZ* (27.1 µm), *IF* (1.7 mN) and *VF* (0.142 mN) are optimized to 61.23 µm, 0.003 mN and 0.01 mN respectively corresponding to the different considered optimization objectives.

Other Indicators	Optimization performance indicators		
	SRZ (µm)	*IF* (mN)	*VF* (mN)
SRZ Fig. IV-5-a	61.2	7.6	32.9
IF Fig. IV-5-b	0	0.003	0.07
VF Fig. IV-5-c	0	0.07	0.01
Prototype array	27.1	1.7	0.14

Table IV-1: SO optimization results

The solutions obtained from this SO optimization result in unacceptable solutions because a global optimuum is not found. SO optimization can not indeed satisfy all performance indicators simultaneously. One performance indicator value gets optimized with the sacrifice of the others e.g. when *SRZ* (61.23 µm) is optimized, *IF* (7.61 mN) and *VF* (32.91 mN) are deteriorated compared to the existing prototype array. However the performance indicators values of the solutions obtained (presented in Table IV-1) can be considered as the best results which can be obtained for each performance indicators. To obtain configurations that ensure a global optimal design (optimization of the three performance indicators at the same time), MO optimization is needed and presented in the next section.

IV.2.4. Multi-objective optimization

MO optimization of the array has been implemented on MATLAB with considering the three performance indicators simultaneously. In this section, the MO optimization setup and the results are presented.

IV.2.4.1. Optimization setup

Similarly to the SO optimization, an initialization setting of GA in the Global optimization tool box of MATLAB is also needed for the MO optimization. This setting includes the characterization of the population size, the maximum generation number and the output conditions. To be consistent with the SO optimization, the population size and the maximum generation number have been set to 40 and 100 respectively. For the MO optimization, there are also three output conditions to terminate the optimization which are same with the SO optimization. The first two conditions are strictly the same with the SO optimization which are the maximum generation size limit and the maximum time limit. However, the third one – fitness function tolerance is defined different from the fitness function value in the SO optimization in MO optimization.

The fitness function value in MO optimization represents the average change in the spread of the Pareto front over the generations illustrated in Figure IV-6 (a two objectives (f_1(x) and f_2(x)) Pareto front has been used for illustration). The spread of the Pareto front corresponds to the Euclidean distance (d_1, d_2, d_3... d_f) between two consecutive solution sets (generated in two consecutive generations by GA) [DEB 2002]. If the average change in spread value is small than the defined tolerance value between two consecutive generations, GA considers that the optimization solution set converges to the Pareto optimal front. The algorithm is then terminated. This value has been set 1×10^{-6} by default.

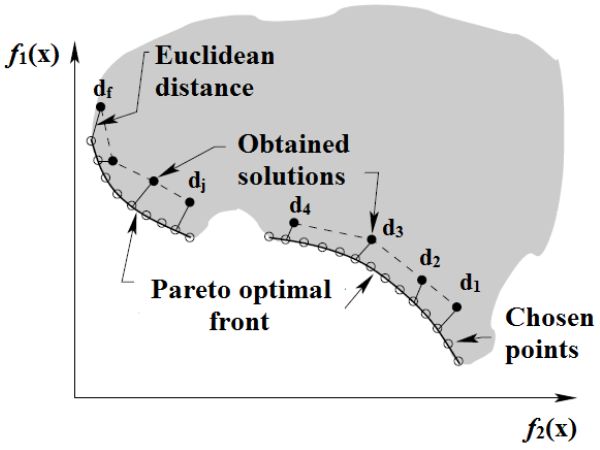


Fig IV-6: Illustration of Pareto front spread using two objective functions, DEB et al. [DEB 2002]

IV.2.4.2. Multi-objective optimization results

In the MO optimization study, the three performance indicators (*SRZ*, *IF* and *VF*) have been considered simultaneously. The MO optimization program has been executed 3 times to verify

if the same optimal result is achieved. It has been found that all 3 calculation attempts have been terminated at the 100th generation due to the first output condition: maximum generation number exceeded. The optimization results from the several attempts are always not the same (due to the randomly search of the GA) but are similar with little changes. The calculation duration is about 28 days.

In MATLAB MO optimization, there is a parameter – Pareto fraction which is ratio value (between 0 and 1) and helps to limit the elite individual numbers on the Pareto front as GA progresses. This limitation of elite individual members will help the MO optimization convergence to a final optimal Pareto front quickly. By default, the Pareto fraction is set 0.35, i.e. the optimal individual number existing on the final Pareto front should be 14 (Pareto fraction value * population size) for our problem. However, a bigger Pareto fraction value enables to generate a final Pareto front with more individuals. In order to enlarge the choice, the Pareto fraction value has been modified to 0.7 in this study. As a result, a final optimal Pareto front set has been defined with 28 individuals selected from the last population by the GA algorithm of MATLAB. These solutions are given via a 3D Pareto front set presented in Figure IV-7.

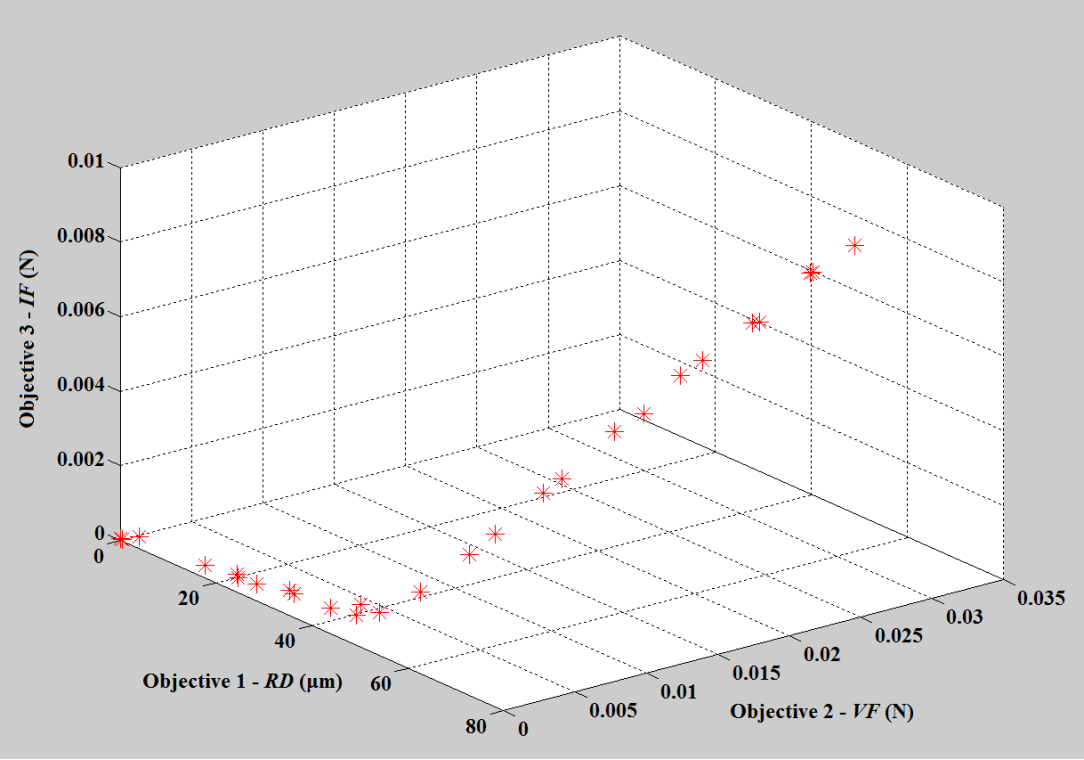


Fig IV-7: 3D Pareto front set

From the Pareto front, 8 optimal solutions out of the 28 solutions have been selected. These eight optimal solutions have been chosen because they ensure a global optimization of the performance of the array with a maximization of the *SRZ* and a minimization of the *IF* and *VF*. The performances of these solutions are presented in Table IV-3.

Solutions	Performance indicators		
	SRZ (µm)	*IF* (mN)	*VF* (mN)
1	43.34	0.64	**0.21**
2	47.61	0.66	0.54
3	58.17	3.90	0.51
4	52.95	1.06	0.39
5	48.53	0.66	0.54
6	35.36	**0.56**	0.34
7	57.40	1.72	1.78
8	**59.14**	2.54	4.60

Table IV-2: Eight selected configurations from the MO Pareto front set

Only one solution has to be chosen from the 8 solutions presented in Table IV-2 to form the new optimal array. An analysis on the performance of the 8 optimal solutions has then been done to help the choice of this solution.

Firstly, the 3rd, 6th and 8th solutions are excluded from the choice for the best compromising solution because these solutions include the worst values of the three performance indicators (*IF*, *SRZ* and *VF*). The performance of the 2nd and the 5th solutions are similar with each other. The *VF* and the *IF* performance indicators of the two solutions are the same. However, the 5th solution enjoys a higher *SRZ* value than the 2nd solution. The 5th solution is then kept and the 2nd solution is excluded. Thirdly, the 7th solution is excluded because two performance indicators (*IF* and *VF*) values are much higher than the other solutions (1st, 4th and 5th).

A comparison between the remaining solutions is illustrated in Figure-8. In this figure, the three axes represent the values of the three performance indicators (*VF*, *IF* and *SRZ*). From this figure, it is visible that solution 1 ensures the best compromise among the three performance indicator. This solution sacrifices a little the *SRZ* value but there is a significant improve for both *IF* and *VF*. In this solution, the minimum value of *VF* (0.21 mN) and the second minimum value of *IF* (0.64 mN) in Table IV-2 have been found. The *SRZ* value (43.34

µm) is not the smallest found value but compared to the prototype array (27.1 µm), this performance indicator has been improved. The solution 1 has then been chosen as the final design of the array. The 14 design parameters of this selected optimal solution are given in Table IV-3. The geometry of this optimal solution is also presented in Figure IV-9. It is observed that the obtained array is quite homogeneous in both PM dimension and magnetization.

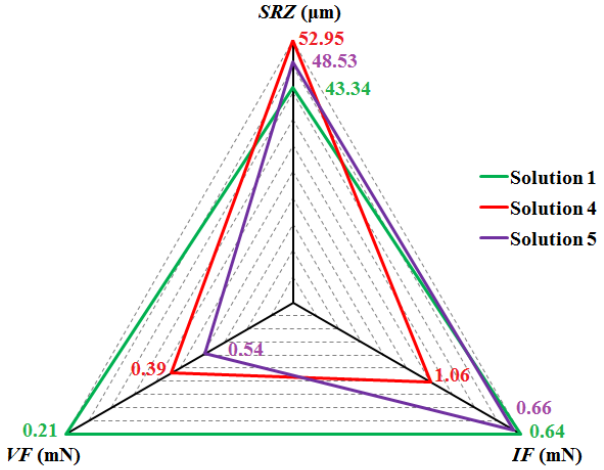


Figure IV-8: Comparison of the remaining solutions (1st, 4st and 5th)

PM magnetizations				
B1	B2	B3	B4	B5
1.36 T	1.29 T	0.81 T	0.87 T	0.95 T
PM dimensions				
D1	D2	D3	D4	D5
1.52 mm	2.93 mm	1.91 mm	2.24 mm	2.28 mm
Distances between PMs				
d5	d6	d7	d8	
2.36 mm	3.79 mm	3.6 mm	3.6 mm	

Table IV-3: Design parameters values corresponding to the selected MO optimal solution

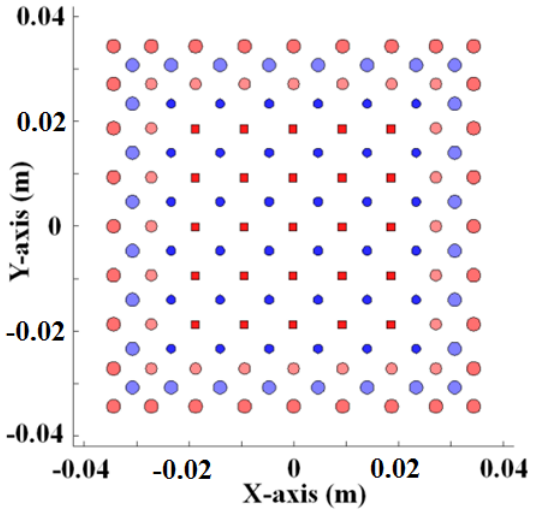


Fig IV-9: Geometry of the selected MO optimal solution

For this optimal design, the average magnetic holding force exerted on the MPM is 0.91 mN. The average holding force has of the existing actuators array is 0.57 mN, this parameter has then be increased. This increase is explained by the increase of the *SRZ* value. However, to ensure that this solution is experimentally usable, the minimum driving current needed to switch the MPM between the discrete positions has been computed. This minimum current value is 1.01 A and 1.25 A for the x and y-axis respectively. Comparing to the minimum current for switching the MPMs in the existing array which is 0.63 A and 0.78 A for the x and y-axis respectively, the minimum current value for the optimal design increases a little. However, this minimum current for the optimal design can still be afforded in the laboratory. This solution is then usable.

For a given application, if one performance indicator is more important than the two other ones; different global optimized solutions can be selected using the Pareto front set. For example, if the performance indicator *IF* is considered as more important than *VF* and *SRZ*, the 6th solution in Table IV-2 should be selected. If the performance indicator *VF* is more important than the *IF* and *SRZ*, the 1st solution in Table IV-2 should be selected. The obtained Pareto front then enables a selection of suitable global optimal solutions with respect to different required importance on one of the performance indicators and without completely neglecting the other ones.

IV.2.5. Comparison of the two methods

A comparison of the performance indicators values between the existing actuators array and the optimized solutions obtained with the SO and MO optimization methods are carried out in

Table IV-4. For this comparison, the three SO optimized solutions obtained independently are taken as reference because the SO optimization provides the considered maximum reachable performance indicators values. For each configuration, the relative value (in percent) corresponding to the best value obtained with SO optimization has been computed. For the *SRZ*, *IF* and *VF* values, 61.20 µm, 0.003 mN and 0.01 mN are considered as 100%.

	Performance indicators		
	SRZ	*IF*	*VF*
Prototype array	44.28% (27.10 µm)	0.17% (1.73 mN)	7.14% (0.14 mN)
MO optimal	70.82% (43.34 µm)	0.47% (0.64 mN)	4.76% (0.21 mN)
SO (*SRZ*)	100.00% (61.20 µm)	0.00% (32.91 mN)	0.13% (7.61 mN)
SO (*IF*)	0.00% (0 µm)	100.00% (0.003 mN)	10.00% (0.1 mN)
SO (*VF*)	0.00% (0 µm)	4.29% (0.07 mN)	100.00% (0.01 mN)

Table IV-4: Comparison of the optimization results

For the MO optimized design, the SRZ performance indicator value has been improved by 26.56% compared to the existing prototype array. This increase of the *SRZ* value improves the MPM self-return ability to the stable positions then the digital behavior of the elementary actuators of the array. The *IF* performance indicator has been increased by 0.30% compared to the existing prototype array *IF*. For the existing prototype array, the *IF* value (1.73 mN) represents 303.51% to the holding force value value (0.57 mN). In the optimal array, the *IF* value (0.64 mN) represents 70.33% of the holding force value (0.91 mN). This decrease on *IF* value characterizes then a reduction of the magnetic interactions between the MPMs of the array. The independence of the elementary actuators is then improved for the MO optimal array compared to the existing actuators array. For the MO optimized design, the *VF* value has been decreased by 2.38% compared to the prototype array. This degradation of the *VF* performance indicator is however linked to the increase of the magnetic holding force value compared to the existing array. For the existing prototype, the holding force value is 0.57 mN and *VF* represents 0.14 mN. For the optimized version, the holding force is 0.91 mN and *VF* represents 0.21 mN. The relative value between the magnetic force variation and the average holding force represents then 24.56% and 23.07% for the existing actuators array and the MO optimized design respectively. The *VF* performance indicator has then been decreased by 1.49%

in relative value compared to the existing actuator array that ensures a very small increase of the magnetic array homogeneity between the MO optimized design and the existing array. The three performance indicators have then been improved compared to the prototype array value.

In addition to the optimization of the three performance indicators, the size of the MO optimal array has been reduced compared to the existing prototype actuators array. The geometries of the MO optimized array and of the existing array are represented in Figure IV-11-a and b, respectively. With the same number of elementary actuators (5 × 5) and the same stroke (0.2 mm), the sizes of the optimized and of the existing arrays are 49 (7.00 × 7.00) cm^2 and 63 (7.94 × 7.94) cm^2 respectively. The surface reduction represents then 21.9% between the two geometries. The optimization study presented in this chapter leads to a new design of the actuators array with the same functionalities and with a best digital behavior (*SRZ*), a greater independence between the elementary actuators (*IF*), a more homogeneous behavior (*VF*) with a smaller size.

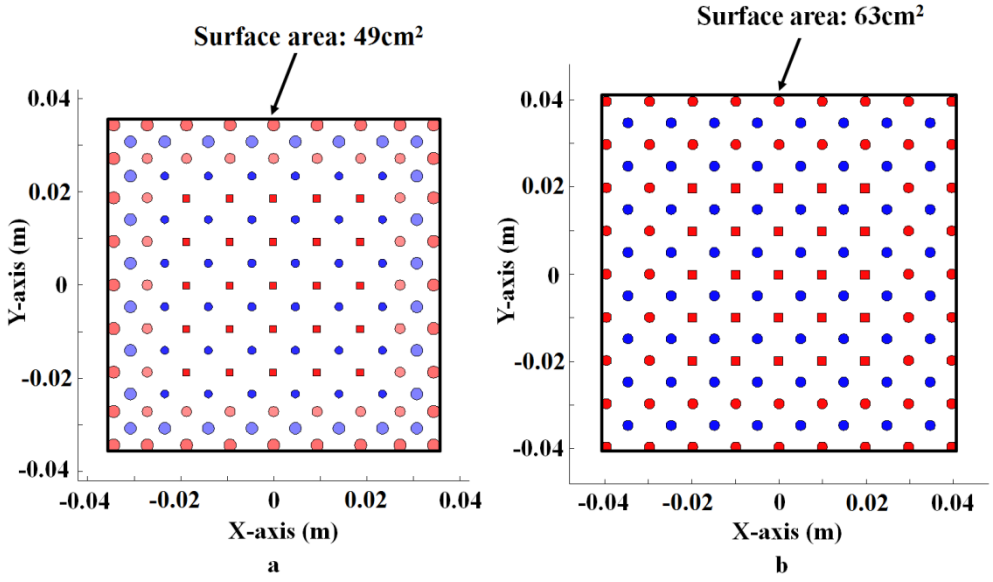


Fig IV-11: a. MO optimal design, b. Prototype array

IV.3. Conclusion

In this chapter, a MO optimization study has been carried out. Several MO optimization methods have been firstly presented and the genetic algorithm optimization method has been selected. The static model enables to compute the magnetic forces exerted on each MPM of the array (presented in Chapter II) has been used for the evaluation of the different array configurations. The implementation of the genetic algorithm has been realized on MATLAB using the Global Optimization Tool box (GOT).

A SO optimization study of the array has secondly been carried out. Three performance indicators have been optimized and three optimal configurations have been obtained while considering the performance indicators independently. These three configurations correspond to the most optimized configuration that can be obtained and have been considered as references to characterize the performances of the final design.

A MO optimization has then been realized while considering the three performance indicators simultaneously and several optimal solutions have been obtained via a 3D Pareto front set. Using the Pareto front, eight configurations have been initially selected and finally a single optimized design which ensures a global compromise between the three performance indicators has been defined. Based on the Pareto front set, some other optimized solutions have also been proposed in order to optimize a most important objective without totally neglecting the other ones.

Finally, a comparison between the performances of the configurations obtained with the SO and the MO optimization studies and the existing prototype array has been carried out. Compared to the existing design, the *SRZ* (44.28%) and *IF* (0.17%) performance indicators have be optimized in absolute value by 26.56% and 0.30% respectively. On the other hand, the *VF* performance indicator has been deteriorated in absolute value (2.38%). However, the magnetic holding force of the optimal array has also been increased compared to the existing array. Thus, a relative *VF* decrease value of 1.49% has been found for the optimal array when compared to the existing prototype array. In addition to the improvement of the performance indicators, the size of the optimized actuators array has been reduced by 21.9% compared to the existing array for the same number of elementary actuators and the same stroke.

Chapter 5: Conclusion and perspectives

This chapter provides a review and a conclusion of the work realized during the thesis and then gives some short-term and long-term perspectives for future research based on the study presented in this thesis.

V.1. Conclusion

In the first chapter, a state of art of the digital actuation has been presented. The basic concept and the properties of the digital actuation principle have been described and a review of digital actuators developed in literature has been carried out. In this review, the different architectures of digital actuators and the physical principles used for their actuation have been presented. On the basis of this state of art, a classification of digital actuators based on the number of stable positions (0, 1, 2 and more) has been proposed. The applications of digital actuators have also been presented and classified into two categories: the single and multiple actuations. The single actuation application category regroups applications where only one digital actuator is used (such as optical, electrical or fluidic switches …). The multiple actuations category regroups applications where several digital actuators are used together to realize complex tasks (such as displacement tables, tactile display devices, modular robots, mechanical memories and etc…). Based on this state of art and on the experience of the Roberval laboratory, the electromagnetic principle has been selected for the actuation of the considered digital actuators array. This physical principle is indeed well adapted for digital actuators especially to obtain a non-energy consuming holding force using the interaction between permanent magnets.

The digital actuators array principle and an application as a planar conveyance device have been firstly described in the second chapter. The architecture of the elementary actuators of the array based on four stable positions with two orthogonal and independent displacement axes is the main originality of this actuators array. Secondly, a static analytical model of the array has been described. This model has been developed on MATLAB and validated by comparing it with the semi-analytical computing software RADIA. The developed model computes the magnetic forces exerted on all the MPMs and has been used to characterize the prototype as the influence of the manufacturing errors on the array performances.

In the third chapter, the prototype of the digital actuators array has been experimentally characterized. The manufacturing errors of the prototype have been measured and their

influences on the array performances have been determined. Due to the limited number of V-A converters available, the planar conveyance application has been characterized using a configuration composed of 8 elementary actuators. Displacements along two directions (x- and y-axes) of the carried plate have been realized. A contactless measurement method, based on an image processing program, has been developed in order to measure the plate displacement. The influences of several parameters (driving and holding current values, driving current form, carried mass value, conveyance on long distances) on the planar conveyance behavior have been characterized.

An optimization based on Genetic Algorithm of the array design has been presented in the fourth chapter. This optimization is based on the static model of the array described in the second chapter and has been implemented on MATLAB. Single-objective and multi-objective optimization studies have been done separately considering three performance indicators. Based on these studies, several optimal designs have been determined and one of them has been selected. With this optimal design, the *SRZ* (44.28%) and *IF* (0.17%) performance indicators have be optimized in absolute value by 26.56% and 0.30% respectively compared to the existing design. The *VF* performance indicator has been optimized by 1.49% in relative value comparing to the existing prototype array. Moreover, the size of the optimized actuators array has been reduced by 21.9% compared to the existing array.

V.2. Perspectives

In this section, several perspectives of the proposed study are presented. These perspectives include both studies of the existing prototype array and new developments or improvements of the array principle.

V.2.1. Perspectives of the existing actuators array

V.2.1.1. Dynamic modelling of the planar conveyance device

A static model of the actuators array able to characterize its static performances has been developed and has been used during its design. The studied application of the array as planar conveyance device has not yet been modelled. A dynamic model of this application which integrates the contribution of each elementary digital actuator and computes the plate displacement should be developed. Using this dynamic model, the influence of the friction non-homogeneity and manufacturing errors on the obtained displacement should be determined. Moreover based on this dynamic model, planar conveyance tasks can then be designed in virtual software environment before implementing in experiments. Optimized trajectories for complex planar conveyance can be designed in order to save the conveyance time and energy consumption.

V.2.1.2. Optimization of the friction conditions between the plate and MPMs

During the experiments, it has been observed that the friction conditions between the plate and MPMs play an important role on the plate displacement. For the proposed application (planar conveyance device), all the MPMs are firstly simultaneously switched to move the plate. During this step, a low sliding between the plate and the MPMs is needed to ensure that the MPMs displacement generates the plate displacement. Secondly, the MPMs are alternatively switched to return in their initial position. A high sliding is then needed at this step to avoid that the plate is moved in the backward direction. To improve the performances of the conveyance application, a study on the friction conditions between the plate and the MPMs should be realized. In this study, additional object fixed on the top side of the MPM and in contact with the plate will be added (Figure V-1). The material and the shape of this object will be studied in order to improve the performances of the conveyance application.

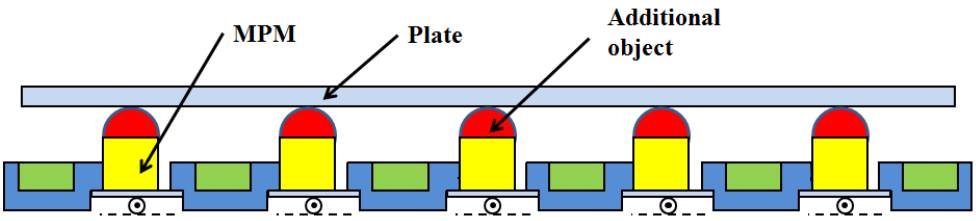


Fig V-1: Improvement of the contact situation

V.2.2. New developments

V.2.2.1. Digital actuator with three displacement directions

The existing array is able to realize displacements in two directions (x- and y-axes). An original perspective of the concept is to add a third displacement direction (along z-axis) as illustrated in Figure V-2.

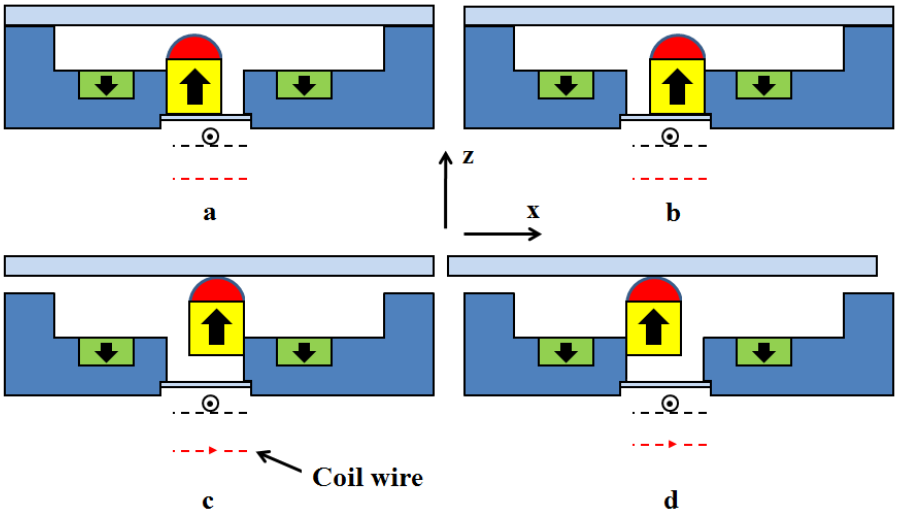


Fig V-2: z-axis actuation

In this figure, only one elementary actuator is represented but the principle can also be adapted for an array. To switch the MPM along z-axis, a coil has to be added below the MPM. Using this type of elementary actuators, the friction non-homogeneity observed during experimentation will be overcome. In this case, the additional displacement axis will be used to ensure or not the contact between the MPMs and the plate. With this solution, materials which ensure a high friction between the MPM and the plate will be chosen. During the switching steps, all the MPMs are in contact with the plate. The sliding effect between the

MPMs and the plate will then be reduced that ensures a high and repeatable plate displacement. However, when the MPMs are switched back to their initial positions, there is no contact between the plate and the MPMs (see Figure V-2 a-b). All the MPMs can then be switched back in one time; there is then no need to switch them back on after another. The time needed to realize a given plate displacement value is then reduced and the control procedure is simplified compared to the existing prototype design.

V.2.2.2. Actuators array with different strokes

In the prototype design, the stroke is identical for the 25 elementary digital actuators. A multi-strokes array can be developed in order to increase the array functionalities. An array composed of two types of actuators with two different stroke values has been taken as an example illustrated in Figure V-3.

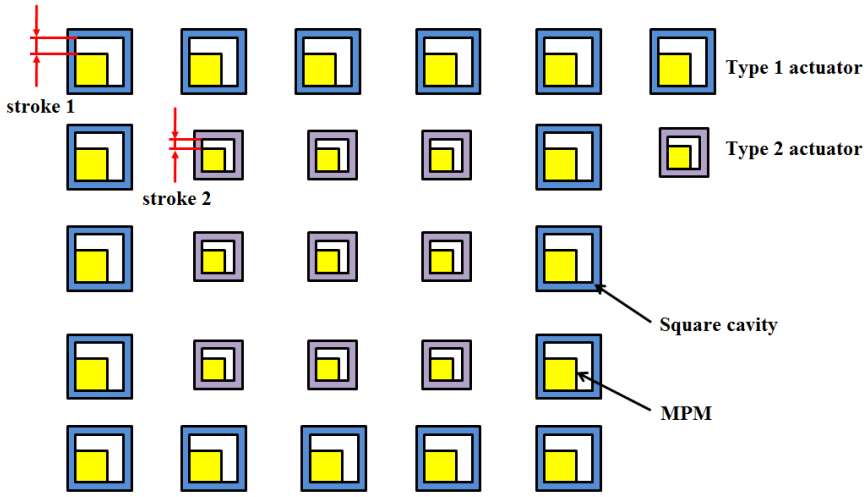


Fig V-3: Actuators array with 2 types of strokes of actuators

For a planar conveyance device with this functionality, the elementary actuators with a large stoke will be firstly used to obtain the largest part of the desired plate displacement with large displacement plate steps. The elementary actuators with a small stroke will then be used to reach the desired value with short displacement plate steps. With this conveyance strategy, the planar conveyance device will be able to displace parts on long distance in a short time, with large displacement steps, while keeping a high displacement resolution with short displacement steps.

V.2.2.3. Micro-fabricated digital actuators array

The mechanical support of the existing array prototype has been manufacturing by conventional machining. In Chapter III, it has been observed that this conventional machining brought significant manufacturing errors that can highly disturb the magnetic equilibrium of the array.

In order to reduce these disruptions, micro-fabrication techniques should be used to manufacture a new version of the array. The use of micro-fabrication techniques will bring three major advantages. The first one is reducing the fabrication errors. It has been previously presented that fabrication errors have important influence to the performance of the array. With the micro-fabrication techniques, the fabrication errors can be reduced to several micro-meters. In our study, such level of fabrication errors will have a small influence on the performances of the array. The second one is the downsizing. With the micro-fabrication techniques, the dimensions of the array can be greatly reduced. Fabrication of an array composed of a huge number of elementary actuators can then be achieved. The third advantage is that micro-fabrication techniques are indeed well suitable to achieve full identical patterns on a surface with a mask because the objects are etched at the same time. A homogeneous behaviour of all the elementary actuators will then be achieved. The use of micro-fabrication techniques is then a very important improvement of the digital actuators array.

Annex: List of publications

This work has been published and presented in the following international conferences.

Conference Communications:

Pengfei HUYAN, Jing XU, Laurent PETIT, Christine PRELLE, "Modeling and optimization of digital electromagnetic actuators array," 2014 IEEE/ASME International Conference on Advanced Intelligent Mechatronics, Besancon, France. July 8-11, 2014.

Laurent PETIT, Pengfei HUYAN, Christine PRELLE, Emmanuel DORE, Frédéric LAMARQUE, "Characterization of a four discrete positions electromagnetic actuator," ESDA 2012 11th Biennial Conference on Engineering Systems Design and Analysis, Nantes, France. July 2-4, 2012.

Pengfei HUYAN, Laurent PETIT, Christine PRELLE, Emmanuel DORE, Frédéric LAMARQUE, "Experimental characterization of a digital electromagnetic actuators array," Proceeding of ACTUATOR 2012, 13th International Conference on New Actuators, Bremen, Germany. June 16-19, 2012.

Laurent PETIT, Pengfei HUYAN, Christine PRELLE, Frédéric LAMARQUE, Emmanuel DORE, "Modeling of a digital eletromagnetic actuators array," 8th France-Japan and 6th Europe-Asia Congress on Mechatronics, Yokohama, Japan. November 22-24, 2010.

Bibliography

Bibliography

[ABAD 2009] J. Abadie, N. Chaillet, C. Lexellent, “Modeling of a new SMA micro-actuator for active endoscopy applications”, Mechatronics, vol. 6, pp. 437-442, 2009.

[ASIM 2002] K. Asim, “Multi-objective Optimization Techniques,” http://www-aaa.eng.ohio-state.edu/-salimul/pubs/multi-bj.pdf, 2002.

[BART 2012] J. Barth, C. Megnin, M. Kohl, “A Bistable Shape Memory Alloy Microvalve With Magnetostatic Latches”, Journal of Microelectromechanical Systems, vol. 21, n°1, pp. 76-84, 2012.

[BISH 2002] R.H. Bishop, “The Mechatronics Handbook”, ISA-The Instrumentation, Systems, and Automation Society, 2002.

[CARA 2008] M. Caramia, P. Dell’Olmo, “Multi-objective management in Freight logictics”, Springer London, 2008.

[CART 2009] R. Carta, G. Tortora, J. Thone, B. Lenaerts, P. Valdastri, A. Menciassi, P. Dario, and R. Puers, “Wireless powering for a self-propelled and steerable endoscopic capsule for stomach inspection,” Sensors Biosensors and Bioelectronics, vol. 25, pp. 845-851, 2009.

[CAZO 2008] P. Cazottes, A. Fernandes, J. Pouget, M. Hafez, “Actuation of bistable buckled beams with Macro-Fiber Composites”, IEEE/RSJ International Conference on Intelligent Robots and Systems (IROS 2008), vol. 6, pp. 564-569, 2008.

[CENS 1977] Y. Censor, "Pareto Optimality in Multi-objective Problems," Appl. Math. Optimization, vol. 4, pp 41-59, 1977.

[CHAL 2013] V. Chalvet, Y. Haddab, P. Lutz, “A Microfabricated Planar Digital Microrobot for Precise Positioning Based on Bistable Modules”, IEEE Transactions on Robotics, vol. 29, n°3, pp. 641-649, 2013.

[CHAP 2004] Y.A. Chapuis, Y. Fukuta, Y. Mita, H. Fujita, “Autonomous Decentralized Systems Based on Distributed Controlled MEMS Actuator for Micro Conveyance Application”, Seisan Kenkyu, vol. 56, n°1, pp. 109-115, 2004.

[CHAR 2008] B. Charlot, W. Sun, K, Yamashita, H. Fujita, H. Toshiyoshi, “Bistable nanowire for micromechanical memory”, Journal of Micromechanics and Microengineering, vol. 18, n°4, 2008.

[CHEN 2008] Q. Chen, Y. Haddab, P. Lutz, “Digtial Microrobotics Based on Bistable Modules: Design of Compliant Bistable Structures”, IEEE/ASME MESA'08, pp. 36-41, 2008.

[CHEN 2011] Q. Chen, Y. Haddab, P. Lutz, “Microfabricated Bistable Module For Digital Microrobotics”, Journal of Micro Nano Mechatronics, vol. 6, pp. 1-12, 2011.

[CHOU 2012] P. Chouinard, J.-S. Plante, “Bistable Antagonistic Dielectric Elastomer Actuators for Binary Robotics and Mechatronics”, IEEE/ASME Transactions on Mechatronics, vol. 17, n°5, pp. 857-865, 2012.

[COCH 2005] K.R. Cochran, L. Fan, D.L. Devoe, “High-power optical microswitch based on direct fiber actuation”, Sensors and Actuators, vol. 8, pp. 512-519, 2005.

[DEB 2002] D. Kalyanmoy, "Multi-Objective Optimization using Evolutionary Algorithms," John Wiley & Sons, Ltd, Chichester, England, 518 pages, 2002.

[DRIE 2010] M. Drien, F. Ceyssens, J. Decoster, R. puers, “Nickel-plated thermal switch with electrostatic latch,” Sensors and Actuators, vol. 6, pp. 148-153, 2010.

[ELLA 1997] P. Elleaume, O. Chubar, J. Chavanne, "Computing 3D Magnetic Field from Insertion Devices", proc. of the PAC97 Conference May 1997, p.3509-3511.

[FURL 2001] P. Furlani, “Permanent magnet and electromechanical device - materials, analysis, and applications”, Academic Press, San Diego, p.518, 2001.

[GERS 2012] Y. Gerson, S. Krylov, B. Ilic, D. Schreiber, “Design considerations of a large-displacement multistable micro actuator with serially connected bistable elements”, Finite Elements in Analysis and Design, vol. 12, pp. 58-69, 2012.

[GIAN 2007] G. Giannopoulos, J. Monreal, and J. Vantomme, “Snap-through buckling behavior of piezoelectric bimorph beams: I. Analytical and numerical modeling” Smart Materials and Structures, vol. 16, pp. 1148-1157, 2007.

[GIDD 2011] P.F. Giddings, H.A. Kim, A.I.T. Salo, C.R. Bowen, “Modelling of piezoelectrically actuated bistable composites”, Materials Letters, vol. 3, pp. 1261-1263, 2011.

[HERD 2004] M. Herding, G. Jobst, G. Urban, P. Woias, “A polymer-based optical 1 × 2 fiber switch”, 9th International Conference on New Actuators (ACTUATORS 2004), Bremen, Germany, 2004.

[HUES 2010] T. Huesgen, G. Lenkm, T. Lemke, P. Woias, “Bistable Silicon microvalve with thermoelectrically driven thermopneumatic actuator for liquid flow control,” IEEE 23rd International Conference on Micro Electro Mechanical Systems (MEMS), vol. 4, pp. 1159-1162, 2010.

[JIA 2009] C. Jia, J. Zhou, W. Dong, W. Chen, “Design and fabrication of silicon-based 8 × 8 MEMs optical switch array,” Microelectronics Journal, vol. 4, pp. 83-86, 2009.

[KHAN 2014] M.U. Khan, “Contribution to the design and fabrication of compact mechatronic systems: Application to an integrated micro-positioning system”, PhD thesis, Laboratoire Roberval – Université de Technologie de Compiègne, 2014.

[KONA 2006] A. Konak, D.W. Coit, A.E. Smith, “Multi-Objective Optimization Using Genetic Algorithms: A Tutorial,” Reliability Engineering and System Safety, vol. 9, pp. 992-1007, 2006.

[LIAO 2010] B.T. Liao, B.T. Chia, S.C. Shih, K.C. Fan, Y.J. Yang, “A 2 x 2 Split Cross-Bar Optical Switch Using a Hybrid Actuation Configuration”, Journal of lightwave technology, vol. 28, n°20, 2010.

[LUHA 2008] R. Luharuka, P. Hesketh, “A bistable electromagnetically actuated rotary gate microvalve”, Journal of micromechanics and microengineering, vol. 18, n°3, 2008.

[MAO 2010] S. Mao, H. Wang, Y. Wu, J. Tang, G. Ding, “A latching bistable microswitch using dual-beam electrothermal actuation”, 5th IEEE International Conference on Nano/Micro Engineered and Molecular Systems (NEMS), vol. 4, pp. 732-735, 2010.

[MATS 2013] T. Matsunaga, K. Totsu, M. Esashi, Y. Haga, “Tactile display using shape memory alloy micro-coil actuator and magnetic latch mechanism”, Displays, vol. 6, pp. 89-94, 2013.

[MIAO 2011] X. Miao, X. Dai, P. Wang, G. Ding, X. Zhao, “Design, fabrication and characterization of a bistable electromagnetic microrelay with large displacement”, Microelectronics Journal, vol. 7, pp. 992-998, 2011.

[MICH 2008] A. Michael, C.Y. Kwok, K. Yu, M.R. Mackenzie, “A Novel Bistable Two-Way Actuated Out-of-Plane Electrothermal Microbridge”, Journal of Microelectromechanical systems, vol. 17, n°1, pp. 58-69, 2008.

[MIRO 2007] E. Mirowski, J. Moreland, S. Russek, M. Donahue, K. Hsieh, "Manipulation of magnetic particles by patterned arrays of magnetic spin-valve traps", Journal of magnetism and magnetic materials, vol. 4, pp. 401-404, 2007.

[OBER 2006] J. Oberhammer, M. Tang, A.Q. Liu, G. Stemme, "Mechanically tri-stable, true single-pole-double-throw (SPDT) switches", Journal of Micromechanics and Microengineering, vol. 9, pp. 1-8, 2006.

[OGDE 2012] S. Ogden, J. Jonsson, G. Thornell, K. Hjort, "A latchable high-pressure thermohydraulic valve actuator", Sensors and Actuators, vol. 188, pp. 292-297, 2012.

[PANE 2009] I.Z. Pane, T. Asano, "Analysis and fabrication of ampere-force actuated bistable curved beam," Japanese Journal of Applied Physics, vol. 48, pp. 06FK08:1-06FK08:4, 2009.

[PARK 2008] S. Park, D. Hah, "Pre-shaped buckled-beam actuators: Theory and experiments", Sensors and Actuators, vol. 7, pp. 186-192, 2008.

[PETI 2009] L. Petit, "Contribution aux techniques d'actionnement numérique Cas d'un système électromagnétique 2D ", PhD thesis, Laboratoire Roberval – Université de Technologie de Compiègne, 2009.

[PETI 2010] L. Petit, P. Huyan, C. Prelle, F. Lamarque, E. Doré, "Modeling of a digital electromagnetic actuators array," 8th France-Japan and 6th Europe-Asia Congress on Mecatronics (MECATRONICS), vol. 6, Tokyo, Japan, 2010.

[PETI 2012] L. Petit, P. Huyan, C. Prelle, E. Doré, F. Lamarque, "Characterization of a four discrete positions electromagnetic actuator", Proceeding of the ASME 2012 11th Biennial Conference on Engineering Systems Design and Analysis (ESDA), vol. 6, Nantes, France, 2010.

[PHAM 2011] H.T. Pham, D.A. Wang, "A quadristable compliant mechanism with a bistable structure embedded in a surrounding beam structure", Sensors and Actuators, vol. 11, pp. 438-448, 2011.

[PORT 2008] P. Portela, P. Camanho, P. Weaver, I. Bond, "Analysis of morphing, multi stable structures actuated by piezoelectric patches", Computers and structures, vol. 10, pp. 347-356, 2008.

[QIAN 2010] Y. Qian, M. Xu, Z. Zeng, X. Yan, "Optimal Multiple-impulse Time-fixed Rendezvous Using Genetic Algorithm", 2nd International Conference on information engineering and computer science, vol. 4, pp. 1-4, 2010.

[RADI 1997] "Radia Main features", http://www.esrf.eu/Accelerators/Groups/InsertionDevices/Software/Radia/Documentation

[ROOD 2008] B. Roodenburg, B.H. Evenblij, "Design of a fast linear drive for (hybrid) circuit breakers - Development and validation of a multi domain simulation environment", Mechatronics, vol. 13, pp. 159-171, 2008.

[TSUC 2006] Y. Tsuchiya, K. Takai, N. Momo, T. Nagami, H. Mizuta, S. Oda, "Nanoelectromechanical nonvolatile memory device incorporating nanocrystalline Si dots", Journal of applied physics, vol. 6, 2006.

[VITU 2009] R. Vitushinsky, S. Schmitz, A. Ludwig, "Bistable Thin-Film Shape Memory Actuators for Applications in Tactile Displays", Journal of Microelectromechanical Systems, vol. 18, n°1, pp. 186-194, 2009.

[WANG 2009] D.A. Wang, H.T. Pham, Y.H. Hsieh, "Dynamical switching of an electromagnetically driven compliant bistable mechanism", Sensors and Actuators, vol. 9, pp. 143-151, 2009.

[WANG 2011] J. Wang, F. Gao, Y. Zhang, "Study on Binary Driven Pneumatic Unit for Hyper-Redundant Robots", 5th International Conference on Automation, Robotics and Applications (ICARA), vol. 5, pp. 329-333, 2011.

[WING 2006] A. Wingert, M.D. Lichter, S. Duhowsky, "On the Design of Large Degree-of-Freedom Digital Mechatronic Devices Based on Bistable Dielectric Elastomer Actuators", IEEE/ASME Transactions on Mechatronics, vol. 11, n°4, pp. 448-456, 2006.

[WONK 2010] S.W. Kim, J.S. Koh, M. Cho, K.J. Cho, "Towards a Bio-mimetic Flytrap Robot Based on a Snap-Through Mechanism", 3rd IEEE RAS and EMBS International Conference on Biomedical Robotics and Biomechatronics (BioRob), vol. 6, pp. 534-539, 2010.

[WU 2010] Y. Wu, G. Ding, C. Zhang, J. Wang, S. Mao, H. Wang, "Design and implementation of a bistable microcantilever actuator for magnetostatic latching relay", Microelectronics Journal, vol. 6, pp. 325-220, 2010.

[YANG 2009] Y.J. Yang, B.T. Liao, "A Novel 4 x 4 Optical Switch Using an Anisotropically Etched Micromirror Array and a Bistable Mini-Actuator Array", IEEE Photonics Technology Letters, vol. 21, n° 2, 2009.

[YANG 2011] B. Yang, B. Wang, “Structure design and fabrication of a bistable microvalve”, Second International Conference on Mechanic Automation and Control Engineering (MACE), vol. 4, pp. 1635-1638, 2011.

[ZAID 2011] S. Zaidi, “Contactless Energy Transfer and Control Strategy for Bistable Micro-Actuator”, PhD thesis, Laboratoire Roberval – Université de Technologie de Compiègne, 2011.

[ZHAN 2007] Y.H. Zhang, G. Ding, S. Fu, B. Cai, “A fast switching bistable electromagnetic microactuator fabricated by UV-LIGA technology”, Mechatronics, vol. 7, pp. 165-171, 2007.

[ZHAO 2013] J. Zhao, R. Gao, Y. Yang, Y. Huang, P. Hu, “A Bidirectional Acceleration Switch Incorporating Magnetic-Fields-Based Tristable Mechanism”, IEEE/ASME Transactions on Mechatronics, vol. 8, n°1, pp. 113-120, 2013.

[ZHOU 2004] G. Zhou, F.E.H. Tay, F.S. Chau, Y. Zhao, VJ Logeeswaran, “Micromechanical torsional digital-to-analog converter for open-loop angular positioning applications”, Journal of micromechanics and microengineering, vol. 9, pp. 737-745, 2004.